Aus dem Institut für Radiologie
der Medizinischen Fakultät Charité – Universitätsmedizin Berlin

DISSERTATION

Quantification of porosity, separated fluid-solid shear wave fields and coupling density with inversion recovery magnetic resonance elastography in porous phantoms and in vivo brain

Quantifizierung von Porosität, getrennten Scherwellenfelder der festen und flüssigen Phasen sowie Kopplungsdichte mittels Inversion-Recovery-Magnetresonanzelastographie in porösen Phantomen und In-vivo-Gehirnen

zur Erlangung des akademischen Grades
Doctor of Philosophy (PhD)

vorgelegt der Medizinischen Fakultät
Charité – Universitätsmedizin Berlin

von

Ledia Lilaj

Datum der Promotion: 25/11/2022

Contents

List of Figures

List of abbreviations

IR-MRE	Inversion recovery - magnetic resonance elastography
IR-MRI	Inversion recovery - magnetic resonance imaging
WM	White matter
MRE	Magnetic resonance elastography
MRI	Magnetic resonance imaging
CSF	Cerebrospinal fluid
MRPE	Magnetic resonance poroelastography
MR	Magnetic resonance
MEG	Motion encoding gradient
TI	Inversion recovery time
TE	Echo time
TR	Repetition time
MP-RAGE	Magnetization Prepared - RApid Gradient Echo
f	Porosity
SNR	Signal to noise ratio
GM	Grey matter
MT	Magnetic transfer

Abstract

Background Magnetic resonance elastography (MRE) is an emerging noninvasive technique based on magnetic resonance imaging (MRI) and shear waves that depicts biomechanical properties of biological tissues.

In MRE, quantitative parameter maps are usually reconstructed under the assumption of monophasic viscoelastic media. Conversely, the poroelastic model, consisting of a solid porous matrix permeated by a fluid, can better describe the behavior of multiphasic soft tissues, e.g., the brain. However, the assumption of two media and their interactions increases the complexity of the underlying motion equations, impeding their solution without independent information on fluid and solid wavefields and prior porosity quantification.

Therefore, the aim of this thesis was threefold: 1) to develop an MRI method for determining porosity; 2) to develop an MRE method for separately encoding shear wave fields of fluid and solid fractions in biphasic tissues; and 3) to estimate coupling density ρ_{12} and thus experimentally validate the poroelastic model equations.

Methods Inversion recovery MRI (IR-MRI) and IR-MRE are introduced for voxel-wise quantification of porosity, shear strain of solid and fluid compartments, and ρ_{12}.

Porosity was estimated in fluid phantoms of different relaxation times, fluid-solid tofu phantoms, and in *in vivo*, in the brains of 21 healthy volunteers. Reference values of phantom porosity were obtained by microscopy and draining the fluid from the matrix. Solid and fluid shear-strain amplitudes and ρ_{12} were quantified in three tofu phantoms and seven healthy volunteers.

Results Phantom porosity measured by IR-MRI agreed well with reference values (R=0.99, $P<.01$). Average brain tissue porosity was 0.14±0.02 in grey matter and 0.05±0.01 in white matter ($P<.001$). Fluid shear strain was phase-locked with solid shear strain but had lower amplitudes in both phantoms and brains ($P<.05$). ρ_{12} was negative in all materials and

biological tissues investigated.

Conclusions IR-MRI for the first time allowed noninvasive mapping of *in vivo* brain porosity and yielded consistent results in tissue-mimicking phantoms. IR-MRI combined with IR-MRE allowed us to separately encode shear strain fields of solid and fluid motion in phantoms and human brain. This led to the quantification of coupling density ρ_{12}, which was negative, as predicted. IR-MRE opens horizons for the development and application of novel imaging markers based on the poroelastic behavior of soft biological tissues. Moreover, quantification of subvoxel multicompartmental interactions provides insight into multiscale mechanical properties, which are potentially relevant for various diagnostic applications.

Zusammenfassung

Hintergrund Die Magnetresonanz-Elastographie (MRE) ist eine neuartige Technik, welche die Magnetresonanztomographie (MRT) mit Scherwellen kombiniert, um so die nichtinvasive Darstellung der biomechanischen Gewebeeigenschaften zu ermöglichen.
In der MRE werden quantitative Parameterkarten von Weichgewebe unter der Annahme monophasischer, viskoelastischer Materialeigenschaften rekonstruiert. Das in dieser Arbeit verwendete poroelastische Modell hingegen berücksichtigt bei Weichgewebe wie dem Gehirn die Mehrphasigkeit des Gewebe bestehend aus einer festen porösen Matrix und flüssigen Kompartimenten. Deren unabhängige mechanische Eigenschaften und ihre Wechselwirkungen erhöhen die Komplexität der zugrundeliegenden Bewegungsgleichungen in der Poroelastographie, wodurch die Lösung ohne zusätzliche Informationen über die Wellenfelder und vorherige Quantifizierung der Gewebeporosität erschwert wird.
Diese Arbeit hatte daher drei Ziele: 1) eine MRT-Methode zur Messung der Gewebeporosität zu entwickeln, 2) eine MRE-Methode zur getrennten Kodierung der Scherwellenfelder von flüssigen und festen Anteilen in biphasischen Geweben zu entwickeln, und 3) die Kopplungsdichte ρ_{12} zu bestimmen um so die biphasischen Modellgleichungen experimentell zu validieren.

Methoden Diese Arbeit stellt die Inversion-Recovery-MRT (IR-MRI) sowie die neuartige Inversion-Recovery-MRE (IR-MRE) vor, womit sich die Porosität, die Scherwellenauslenkung der festen und porösen flüssigen Phasen sowie die Kopplungsdichte ρ_{12} in Weichgeweben quantifizieren lassen.
Porosität wurde in Flüssig-Phantomen unterschiedlicher Relaxationszeiten, Flüssig- Festkörper-Phantomen auf Tofubasis sowie *in vivo* im Gehirn bei 21 gesunden Probanden ermittelt. Referenzwerte der Porosität wurden in Phantomen durch Mikroskopie sowie Flüssigkeitsdrainage bestimmt. Feste und flüssige Scherauslenkungsamplituden und ρ_{12} wurden in drei Tofuphan-

tomen und bei sieben gesunden Probanden quantifiziert.

Ergebnisse Die mittels IR-MRI gemessene Porosität der Phantome stimmte gut mit den Referenzwerten überein (R=0.99, $P<.01$). Die durchschnittliche Porosität der grauen und weißen Substanz betrug 0.14±0.02 und 0.05±0.01 ($P<.001$). Die Scherwellenamplituden der flüssigen Anteile und der festen Matrix waren phasengekoppelt, jedoch geringer in den flüssigen Anteilen ($P<.05$). ρ_{12} war in allen untersuchten Materialien und Geweben negativ.

Schlussfolgerung Mittels der IR-MRI konnten erstmals die Porosität von Hirngewebe *in vivo* nichtinvasiv abgebildet und die Konsistenz der Werte in gewebeähnlichen, porösen Phantomen nachgewiesen werden. Die Kombination von IR-MRI mit IR-MRE ermöglichte die getrennte Kodierung von Scherwellenfeldern fester und flüssiger Phasen und damit die Quantifizierung der Kopplungsdichte ρ_{12}, welche, wie theoretisch vorhergesagt, negative Werte aufwies.
Die IR-MRE eröffnet vielfältige Möglichkeiten zur Entwicklung und Anwendung neuartiger Bildgebungsmarker auf der Grundlage poroelastischer Kenngrößen von Weichgeweben und ermöglicht somit potenziell eine Vielzahl diagnostischer Anwendungen.

Chapter 1

Introduction

Magnetic resonance elastography (MRE) is a noninvasive imaging technique that uses extrinsically induced shear waves as kind of a contrast medium to measure the viscoelastic response of biological soft tissues [2]. At the current state of the art, MRE is the only modality that can measure mechanical properties of the whole brain *in vivo* and noninvasively, while other methods are limited by the rigid skull [3, 4, 5]. Ultrasound elastography has only been performed in the neonatal brain through the fontanelles [6] and in adult brains for tumor assessment after skull opening [7]. Recently, time-harmonic ultrasound elastography has been introduced for noninvasively determining brain stiffness, however, without spatial resolution [8, 9, 10]. By contrast, MRE can generate spatially resolved maps of viscoelastic parameters that characterize the mechanical properties of brain tissue.

The mechanical model that has been adopted for MRE assumes that brain tissue is a monophasic viscoelastic medium [11]. *In vivo* viscoelastic parameters measured using MRE were mapped to create a reference atlas of the distribution of viscoelasticities in the human brain [12] and were correlated with age and sex [13, 14, 15, 16]. Moreover, cerebral viscoelasticity was investigated in normal pressure hydrocephalus [17, 18], multiple sclerosis [19, 20], Alzheimer's disease [21, 22], Parkinson's disease [23, 24], and dementia [25, 26].

However, several biological tissues, such as the brain [27, 28], cartilage [29], or edematous tissue [30], are better described by a biphasic poroelastic mechanical model which assumes a porous matrix permeated by an incompressible fluid [31]. In this model, the solid compartment may include cells and an extracellular matrix, while the fluid compartment may consist of interstitial fluid, cerebrospinal fluid (CSF), and blood.

The use of the poroelastic model instead of the viscoelastic model clearly leads to increased

complexity. The poroelastic model requires the characterization of two media instead of one, distributed throughout the tissue in different volume ratios. Porosity is the main structural parameter that describes a poroelastic medium and is defined as the ratio of the fluid volume over total volume. Furthermore, the solid-fluid interactions as the coupling of motion fields lead to a larger number of modeling parameters.

The poroelastic model was first introduced for ultrasound-based elastography [32, 33, 34] and was then expanded to MR-based poroelastography [35, 36]. Postprocessing of magnetic resonance poroelastography (MRPE) data was introduced based on a finite-elements approach with a number of physical properties defined a priori, such as porosity or hydraulic conductivity [35, 37]. Porosity, for example, has never been mapped noninvasively in the *in vivo* human brain. In previous poroelastography studies, a global porosity of 0.20 was assumed for the entire brain [38]. Furthermore, no studies have experimentally measured the fluid and solid displacement fields in biphasic media or addressed coupling density ρ_{12}. ρ_{12} is related to the transfer of kinetic energy between the two compartments and, due to the fluid's inability to statically support shear waves, it has been predicted to be negative [39]

The aim of this Ph.D. thesis was threefold: i) development of specialized acquisition protocols and postprocessing strategies in order to quantify porosity based on each compartment's T_1 relaxation time, ii) separate measurement of the displacement field of the fluid and the solid compartment, and iii) estimation of coupling density ρ_{12} in *in vivo* human brain.

The feasibility of the novel method was demonstrated in phantom experiments. First, theoretically predicted porosity was tested on an emulated phantom. Then tissue-mimicking phantoms made of tofu, whose microstructure is characterized by a matrix with fluid-filled pores, were produced at different porosities. The estimated porosity was compared with porosities determined by alternative methods. Shear strain fields were separated, and ρ_{12} maps were generated and compared with the results expected from theory. Finally, brain tissue was modeled as a poroelastic medium permeated by an extracellular fluid [40] with T_1 relaxation properties similar to those of CSF [41]. The strain fields of the solid matrix and the fluid compartment and ρ_{12} maps were estimated for each scanned brain slice.

Chapter 2

Theory

2.1 The mechanical medium model

2.1.1 The viscoelastic monophasic medium model

The mechanical properties of a monophasic medium can be described in terms of elasticity and viscosity. These two characteristics of the tissue determine the mechanical response of the medium to a time-varying force. A purely elastic medium will deform but restore its initial shape after the external force has been removed. It can be modeled as a massless spring. The stress-strain relation of the spring model in the one-dimensional case is

$$\sigma_{\mathrm{e}} = E\varepsilon \tag{2.1}$$

where σ_e is the stress into the direction denoted by vector e, E the Young's modulus and ε the resulting strain [2]. Strain is the variation in length ΔL relative to the original length L_0 of the spring

$$\varepsilon = \frac{\Delta \mathrm{L}}{L_0}. \tag{2.2}$$

In contrast, a purely viscous medium retains deformation after removal of the external force. This is due to conversion of mechanical work in thermal energy during the deformation. The simplest viscous model is a dashpot filled with viscous fluid and with a piston that can move in the fluid. The dashpot model stress-strain relation is

$$\sigma_v = \eta\dot{\varepsilon} \tag{2.3}$$

where σ_v is the stress in the medium denoted by v, η is the viscosity of the fluid and $\dot{\varepsilon}$ is the rate of change of the strain [2]. In a three dimensional context, we can define stress and

strain in a Cartesian coordinate system where they can be represented by 3×3 matrixes

$$\varepsilon = \begin{bmatrix} \varepsilon_{11} & \varepsilon_{12} & \varepsilon_{13} \\ \varepsilon_{21} & \varepsilon_{22} & \varepsilon_{23} \\ \varepsilon_{31} & \varepsilon_{32} & \varepsilon_{33} \end{bmatrix} \tag{2.4}$$

$$\sigma = \begin{bmatrix} \sigma_{11} & \sigma_{12} & \sigma_{13} \\ \sigma_{21} & \sigma_{22} & \sigma_{23} \\ \sigma_{31} & \sigma_{32} & \sigma_{33} \end{bmatrix}. \tag{2.5}$$

Hooke's law describes the relationship between the nine stress coefficients σ_{ij} nd the nine strain coefficients ε_{kl} of a continuous linear elastic material by the elasticity tensor $\boldsymbol{C}$:

$$\sigma_{ij} = \sum_{k,l=1}^{3} C_{ijkl}\varepsilon_{kl} \tag{2.6}$$

where $i,j = 1,2,3$ [2]. The stiffness tensor $\boldsymbol{C}$ is a medium's property and depends on physical state variables such as microstructure, temperature, or pressure. Due to inherent symmetries of σ and ε [42], and the symmetry of the material [43], assuming that the considered medium is isotropic, $\boldsymbol{C}$ can be simplified in terms of the bulk modulus K and shear modulus μ (or denoted by G) [2]. The first parameter quantifies the medium resistance to a change in volume and the second to shear deformation.

$$\begin{pmatrix} \sigma_{11} \\ \sigma_{22} \\ \sigma_{33} \\ \sigma_{12} \\ \sigma_{23} \\ \sigma_{13} \end{pmatrix} = \begin{pmatrix} \left(K+\frac{4}{3}\mu\right) & \left(K-\frac{2}{3}\mu\right) & \left(K-\frac{2}{3}\mu\right) & 0 & 0 & 0 \\ \left(K-\frac{2}{3}\mu\right) & \left(K+\frac{4}{3}\mu\right) & \left(K+\frac{4}{3}\mu\right) & 0 & 0 & 0 \\ \left(K-\frac{2}{3}\mu\right) & \left(K-\frac{2}{3}\mu\right) & \left(K+\frac{4}{3}\mu\right) & 0 & 0 & 0 \\ 0 & 0 & 0 & \mu & 0 & 0 \\ 0 & 0 & 0 & 0 & \mu & 0 \\ 0 & 0 & 0 & 0 & 0 & \mu \end{pmatrix} \cdot \begin{pmatrix} \varepsilon_{11} \\ \varepsilon_{22} \\ \varepsilon_{33} \\ 2\varepsilon_{12} \\ 2\varepsilon_{23} \\ 2\varepsilon_{13} \end{pmatrix}. \tag{2.7}$$

Due to the very low compressibility of most biological media, the compression modulus K is extremely large in the order of GPa, while the shear modulus μ is in the order of kPa. In soft biological tissues, the shear modulus conveys valuable structural information while, assuming a monophasic material, the compression modulus is essentially determined by the high incompressibility of water. However, as shown later, the situation changes when we account for freely moving fluid immersed within a solid tissue matrix.

The viscoelastic model is a combination of the spring and dashpot models. As in electrical circuits, the elastic and viscoelastic models can be combined to assemble systems with

complex behaviors. A parallel arrangement of a spring and a dashpot model represents the Kelvin-Voigt model, and the serial alignment is referred to as the Maxwell model. The solution of these systems is similar to their electrical analogy, leading to differential equations that would have to be solved for ε and $\dot{\varepsilon}$ at the same time. A representation in the Laplace domain is preferred since, in the frequency representation, differentiation becomes multiplication and therefore it simplifies these systems' solutions into algebraic expressions. The Kelvin-Voigt model constitutive equation, being a composition of the two components in parallel, is

$$\sigma = \sigma_{spring} + \sigma_{dashpot} = E\varepsilon + \eta\dot{\varepsilon}. \tag{2.8}$$

After Laplace transform, it becomes

$$\bar{\sigma} = E\bar{\varepsilon} + \eta \mathrm{s}\bar{\varepsilon} \tag{2.9}$$

where s is the Laplace domain variable and the displacement at t=0 is assumed null [2]. Therefore, $\overline{G^*}(s) = E$ for the spring model and $\overline{G^*}(s) = \eta s$ for the dashpot model. The Laplace domain variable s can be substituted by $\mathrm{s} = \mathrm{i}\omega$, and the resulting quantity $\overline{G^*}(s)$ is the measure of viscoelastic properties of the tissue when an oscillating strain is applied with angular frequency $\overline{\omega}$. Two parametrizations are commonly used to represent the complex shear modulus:

$$G^* = G' + iG'' \tag{2.10}$$

$$G^* = |G^*| \cdot e^{i\varphi} \tag{2.11}$$

where G' and G'' denote the real and imaginary part, and G^* and φ the magnitude and phase of the complex modulus [2]. The phase varies between 0 and $\pi/2$, describing a purely elastic medium ($\varphi = 0$) to a purely viscous medium ($\varphi = \pi/2$). The tangent of the phase angle φ is called loss angle [2] or fluidity [44], defined as

$$\tan(\varphi) = \frac{G'}{G''}. \tag{2.12}$$

2.1.2 The poroelastic medium model

A poroelastic medium is, in the simplest case, a biphasic medium composed of a porous elastic solid matrix permeated by an incompressible fluid [31]. Contiguous pore space is assumed, allowing the fluid compartment to freely move through the solid matrix. A fundamental parameter that describes the structure of a poroelastic medium is called porosity, and it is defined as the volume fraction occupied by the fluid compartment:

$$f = \frac{V^f}{V} \tag{2.13}$$

where V is a medium volume element, and V^f is the enclosed fluid volume. All the pores are assumed filled with fluid, therefore the volume ratio of the solid matrix is defined as $1 - f$. The mechanical response of the matrix is described by shear modulus μ^s and bulk modulus K^s. Since we assume that shear waves cannot propagate in the fluid compartment, we will only introduce the fluid bulk modulus K^f. Furthermore, since viscosity is neglected in this model, all the parameters are real-valued. Given these assumptions, we can formulate the relationship between static deformation and resulting stresses using the following generalization of Hooke's law

$$\begin{pmatrix} (1-f)\sigma^s_{11} \\ (1-f)\sigma^s_{22} \\ (1-f)\sigma^s_{33} \\ (1-f)\sigma^s_{12} \\ (1-f)\sigma^s_{23} \\ (1-f)\sigma^s_{13} \\ f\sigma^f \end{pmatrix} = (1-f) \begin{pmatrix} \left(K^s + \frac{4}{3}\mu^s\right) & \left(K^s - \frac{2}{3}\mu^s\right) & \left(K^s - \frac{2}{3}\mu^s\right) & 0 & 0 & 0 & fH \\ \left(K^s - \frac{2}{3}\mu^s\right) & \left(K^s + \frac{4}{3}\mu^s\right) & \left(K^s - \frac{2}{3}\mu^s\right) & 0 & 0 & 0 & fH \\ \left(K^s - \frac{2}{3}\mu^s\right) & \left(K^s - \frac{2}{3}\mu^s\right) & \left(K^s + \frac{4}{3}\mu^s\right) & 0 & 0 & 0 & fH \\ 0 & 0 & 0 & \mu^s & 0 & 0 & 0 \\ 0 & 0 & 0 & 0 & \mu^s & 0 & 0 \\ 0 & 0 & 0 & 0 & 0 & \mu^s & 0 \\ fH & fH & fH & 0 & 0 & 0 & \frac{f}{1-f}K^f \end{pmatrix} \cdot \begin{pmatrix} \epsilon^s_{11} \\ \epsilon^s_{22} \\ \epsilon^s_{33} \\ 2\epsilon^s_{12} \\ 2\epsilon^s_{23} \\ 2\epsilon^s_{13} \\ \epsilon^f \end{pmatrix} \tag{2.14}$$

where the coupling modulus H quantifies the stress induced in one compartment by deformation of the other [2].

This approach does not account for added stresses induced by hydrostatic pressure gradients since, as in the monophasic medium model, we are only focused in shear deformation and assume the corresponding model parameters to be pressure-independent. In the marginal cases $f \to 0$ and $f \to 1$, Eq. 2.14 reduces to the classical monophasic Hooke's law for a solid (Eq. 2.7) or fluid, respectively.

Equation of motion

The equations of motion are derived by equating the second time derivative of the displacement field, $\ddot{\mathbf{u}}$ (i.e., local acceleration of the medium) with the gradient of the stress tensor:

$$\rho\ddot{\mathbf{u}} = \nabla \cdot \boldsymbol{\sigma}. \tag{2.15}$$

ρ denotes mass density. Applying the divergence operator to Eq. (2.14) and separating the resulting equations for fluid and solid motion yields for the right-hand side

$$(1-f)\nabla \cdot \boldsymbol{\sigma}^s = (1-f)\left[\left(K^s + \frac{1}{3}\mu^s\right)\nabla\left(\nabla \cdot \mathbf{u}^s\right) + fH\nabla\epsilon^f + \mu^s\Delta\mathbf{u}^s\right] \tag{2.16}$$

$$f\nabla\sigma^f = f(1-f)H\nabla\left(\nabla \cdot \mathbf{u}^s\right) + fK^f\nabla\left(\nabla \cdot \mathbf{u}^f\right). \tag{2.17}$$

The elastic properties are assumed to vary slowly in space, therefore their gradients were neglected.

Eqs. 2.16 and 2.17 determine the motion of the full vector field, which is composed of both shear and volumetric deformation. However, from Eq. 2.14, the shear strain appears decoupled from volumetric stress, and vice versa. As the focus of elastography is on shear deformation, the curl operator is applied to the displacement field to suppress volumetric deformation (compression waves).

$$\rho\nabla \times \ddot{\mathbf{u}} = \nabla \times \nabla \cdot \boldsymbol{\sigma}. \tag{2.18}$$

For the acceleration terms present on the left-hand side of Eq. 2.18, we utilize the densities introduced in Biot's original theory [45]:

$$\rho_{11}\ddot{\mathbf{u}}^s + \rho_{12}\ddot{\mathbf{u}}^f = (1-f)\nabla \cdot \boldsymbol{\sigma}^s \tag{2.19}$$

$$\rho_{12}\ddot{\mathbf{u}}^s + \rho_{22}\ddot{\mathbf{u}}^f = f\nabla\sigma^f \tag{2.20}$$

with $\rho_{11} = (1-f)\rho^s - \rho_{12}$, $\rho_{22} = f\rho^f - \rho_{12}$, and coupling density $\rho_{12} < 0$. ρ^f and ρ^s are the fluid and the solid compartment densities. The coupling density quantifies acceleration of one phase caused by deformation of the other phase, resulting, counterintuitively, in a negative quantity. This parameter is not related to the properties of a single medium alone but represents the interaction between two compartments. This concept that recalls the idea of fictitious forces [46]. In the frame of poroelastic media, an essential characteristic of the fluid compartment is its inability to resist shear deformation due to its shear modulus being zero. However, due to adhesion and friction at the solid-fluid interface and deformation of

the pore space's architecture, the fluid can be forced to follow the deformation of the solid. The fluid, like a passenger whose weight slows down an accelerating car, acts as a "parasitic mass" to matrix motion, thus, having a decelerating effect on the solid displacement. It is important to note that in this process, no energy is dissipated but kinetic energy is exchanged between the phases without heat generation.

Applying the curl operator to Eqs.2.19 and 2.20 yields the equations for the shear fields only, with $\mathbf{c} = \nabla \times \mathbf{u}$

$$(1-f)\rho^s \ddot{\mathbf{c}}^s + \rho_{12}\left(\ddot{\mathbf{c}}^f - \ddot{\mathbf{c}}^s\right) = (1-f)\nabla \times \nabla \cdot \boldsymbol{\sigma}^s \tag{2.21}$$

$$f\rho^f \ddot{\mathbf{c}}^f + \rho_{12}\left(\ddot{\mathbf{c}}^s - \ddot{\mathbf{c}}^f\right) = f\nabla \times \nabla \sigma^f = \mathbf{0} \tag{2.22}$$

In Equation 2.22, we exploited that $\nabla \times \nabla \xi = \text{curl grad } \xi = 0$ for any scalar field ξ. This equation allows us to establish a relationship between the two shear displacement fields:

$$\ddot{\mathbf{c}}^f = -\frac{\rho_{12}}{f\rho^f - \rho_{12}}\ddot{\mathbf{c}}^s \tag{2.23}$$

Since $\rho_{12} < 0$ and f, $\rho_f > 0$, the two displacement fields have the same sign. In the case of oscillating displacements, $\tilde{\mathbf{c}} = \mathbf{c} \cdot e^{i(\omega t + \phi_0)}$, the displacement fields of the solid and liquid compartment can be expected to have approximately the same phase $\phi_0 + \omega t$.

2.2 Signal generation

2.2.1 Encoding propagating waves with MRE

MRE is a phase contrast-based imaging method for the measurement of strain displacement fields in an object. This technique involves essentially three steps:

1. generation of waves that propagates through the medium,
2. acquisition of MR images that depict the propagation of the induced shear waves,
3. processing of the acquired images in order to generate quantitative maps of biomechanical parameters, e.g., magnitude and phase of the complex shear modulus [47].

In this study, the focus is only on *time-harmonic* MRE, in which tissue displacement is induced by time-harmonic waves. Other methods based on non-harmonic motion exist, but are less common [48, 49]. The technique that allows the acquisition of propagating shear waves into the phase of MR images invented by Muthupillai et al. [11] is based on the use of motion encoding gradients (MEGs) to sense wave fields by storing displacement information in the phase of the complex MR signal. This allows the decoupling of the motion sensitivity from image resolution (∼hundreds of micrometers versus ∼2 mm) [2]. Imposed a gradient field $\mathrm{G_r(t)}$ is imposed, the motion of nuclear spins results in the phase shift ϕ, defined as

$$\phi = \gamma \int_0^{\tau} G_r(t) \cdot r(t) dt \tag{2.24}$$

where γ is the gyromagnetic ratio, τ is the time duration of a gradient field,t is the time, $r(t)$ is the position of the nuclear spins as a function of time [11]. If the nuclear spins and $\mathrm{G_r(t)}$ oscillates with the same harmonic motion frequency and τ is set such as

$$\int_0^{\tau} G_r(t) dt = 0 \tag{2.25}$$

the spins motion is encoded into the phase of the magnetic resonance complex signal, with phase shift

$$\phi(\vec{r}, \theta) = \frac{\gamma n T \left(\vec{G} \cdot \overrightarrow{\xi_0} \right)}{2} \cos(\vec{k} \cdot \vec{r} + \theta) \tag{2.26}$$

where r is the position vector, θ is the phase offset between the applied motion and the gradient, n is the gradient cycles, T is the MEG period, G is the gradient amplitude, ξ_0 is the displacement amplitude and k is the wave vector [11]. It is essential in an MRE sequence the

presence of MEGs synchronized with the external mechanical vibration. Usually, the wave is sampled with 4 to 8 phase images for drive frequency. The aforementioned synchronization enables the application of MEGs at the exact time points of a vibration period. More detailed information about MRE imaging sequences is available in [2, 11].

2.2.2 Model of biphasic signal generation with inversion recovery

In a monophasic medium, the longitudinal relaxation time can be estimated using an inversion recovery (IR) sequence. This imaging technique essentially a sequence where a 180° pulse precedes the signal generation of an interval of time, called inversion recovery time (TI). During the TI interval, the tissue undergoes T_1 relaxation, as shown in Fig. 2.1.

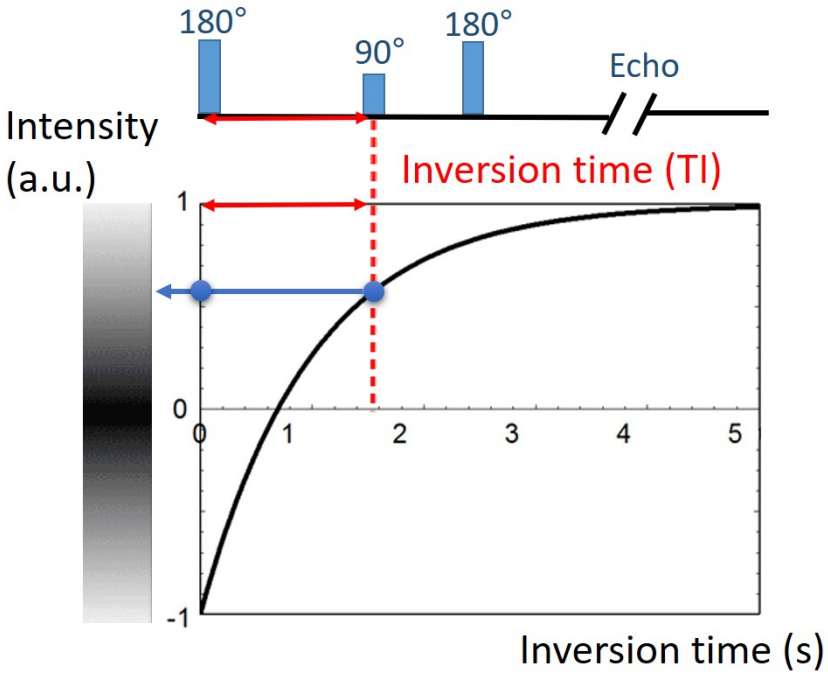

Figure 2.1: Inversion recovery scheme for monophasic media.

This process is introduced to create different contrast between tissues characterized by different T_1 times. In order to estimate the T_1 of each media, several images of the tissue with different TI can be acquired and the signal intensity of each voxel is fitted with a monoexponential equation

$$I(TI) = I_\infty \cdot \left(1 - 2 \cdot e^{-\frac{TI}{T_1}}\right) + C \tag{2.27}$$

where *I(TI)* is the intensity of the voxel of the image with inversion time *TI*. I_∞ is the voxel intensity without inversion. C is the noise offset and it is typically two orders of magnitude smaller than I. Since we ensured that $TR > 5T_1$ in all measurements, we assumed that each scan was conducted with fully relaxed longitudinal magnetization and therefore we neglected TR-dependent terms in Eq. 2.27. In the poroelastic medium, the fluid and solid

compartment simultaneously contribute to the signal generated in a voxel volume. Their contribution varies based on their specific characteristics that could ideally be measured via monophasic fitting in case of voxel small enough to avoid any partial volume effect, and by the volume ratio of each tissue in a voxel, or porosity. Many biological tissues can be modeled as biphasic poroelastic media. In this thesis, we modeled the brain tissue as a poroelastic material where the solid compartment comprises macromolecules and cells, while the fluid compartment comprises moving fluids as CSF or interstitial fluid, which we assume as similar relaxation properties than CSF. The IR-MRI biphasic medium signal is a superposition of the two compartments' contribution, each weighted by its volume fraction, which is f for the fluid and $(1-f)$ for the solid (Fig. 2.2).

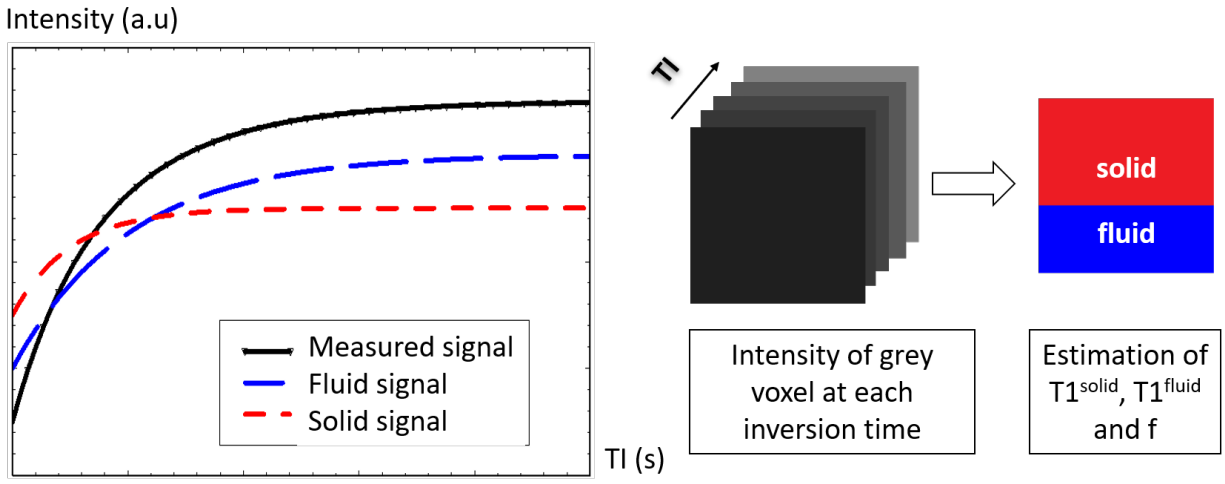

Figure 2.2: Inversion recovery scheme for biphasic media.

To account for biphasic T_1 signal relaxation, the longitudinal relaxation is expressed as a function of TI:

$$I^m(TI) = I^f \cdot f\left(1 - 2e^{-\frac{TI}{T_1^f}}\right) + I^s \cdot (1-f)\left(1 - 2e^{-\frac{TI}{T_1^s}}\right) + C \tag{2.28}$$

The subscript m on the equation left-hand side indicates that this quantity is the measured signal intensity, in contrast with I^s and I^f, the signal intensities of the solid and fluid compartment, which can only be determined indirectly. Furthermore, I^s and I^f account for the signal intensity dependence on $T2/T2^*$ and TE, which are not relevant for this work. To estimate porosity, Equation 2.28 is fitted to a series of IR-MRI scans acquired with different inversion times. However, six unknown parameters (I^f, I^s, T_1^f, T_1^s, f, C) lead to

an unstable fitting process. Therefore, the fluid properties, I^f and T_1^f,will be assessed in an independent estimation, assuming negligibility of their variability across the biphasic object, thus reducing the unknown parameters to the set (I^s, T_1^s, f, C). It is possible to simplify the equation further using the information given by a specific inversion recovery obtained without inversion recovery pulse, which formally is identical to $TI \to \infty$ (TI dependence is dropped in the following formulas)

$$I^{m,\infty} = I^f \cdot f + I^s \cdot (1 - f) + C \tag{2.29}$$

Since offset C in Eq 2.29 is usually two orders of magnitude lower than I^f and $I^{m,\infty}$, it will be neglected henceforth, thus improving fitting stability at the expense of precision. Solving Eq 2.29 for I^s and substituting into Eq. 2.28 yields the following simplified equation:

$$I^m(TI) = -2 \cdot f \cdot I^f e^{-\frac{TI}{T_1^f}} - 2\left(I^{m,\infty} - f \cdot I^f\right) \cdot e^{-\frac{TI}{T_1^s}} + C. \tag{2.30}$$

With I^s eliminated as an unknown parameter, the group of fitting parameters is reduced to f, C, and $T1_s$. The IR-MRE signal equation of a biphasic medium is the extension of Eq 2.28 and includes the motion-induced signal phase:

$$M^m \cdot e^{i\varphi^m} = I^f \cdot f \left(1 - 2e^{-\frac{TI}{T_1^f}}\right) \cdot e^{i\varphi^f} + I^s(1 - f)\left(1 - 2e^{-\frac{TI}{T_1^s}}\right) \cdot e^{i\varphi^s}. \tag{2.31}$$

M^m and φ^m represent the magnitude and phase of the measured MRE signal. If MRE is performed twice with two different inversion times (TI_1 and TI_2), the system of the two resulting versions of Equation 2.31 can be used to decompose the measured compound displacement field, φ^m, into the compartmental fields φ^s and φ^f. The simplest case is the one where we choose $TI_1 \to \infty$ (i.e., no inversion is performed) and $TI_2 = \ln(2)T_1^f$, i.e., the inversion time that nulls the signal of the fluid compartment. The system of the Equation 2.31 two versions for two inversion times can be solved for φ^s and φ^f

$$e^{i\varphi^s} = \frac{M^{m,2} \cdot e^{i\varphi^{m,2}}}{I^s \cdot (1 - f)\left(1 - 2e^{-\frac{TI^{m,2}}{T_1^s}}\right)} \tag{2.32}$$

$$e^{i\varphi^f} = \frac{M^{m,1} \cdot e^{i\varphi^{m,1}} - \frac{M^{m,2} \cdot e^{i\varphi^{m,2}}}{\left(1 - 2e^{-\frac{TI^{m,2}}{T_1^s}}\right)}}{I^f \cdot f} \tag{2.33}$$

where indices 1 and 2 indicate the measurements with TI_1 and TI_2.

Chapter 3

Materials and Methods

3.1 IR-MRI phantoms

3.1.1 Fluid-fluid phantom

A simple phantom made of two fluids of different T1-relaxation times was used to emulate a biphasic phantom. The phantom is composed of two 100 ml flat rectangular containers filled with physiological solutions. In one of the two containers, the solution was doped with 10^{-4} mol/l gadolinium (Dotarem, Guerbet, Roissy, France) in order to change the T1 of the fluid (Figure 3.1).

Figure 3.1: Fluid-fluid phantom. Figure adapted from [1].

3.1.2 Solid-fluid biphasic phantoms made of tofu

Twelve tofu samples were produced with different porosities starting with 220 ml soy milk (Soja Drink Nature, DM, Germany) heated up to 90°C in a beaker and coagulated by adding 25 ml of acetic acid (4 vol% in water). The coagulated curd was then transferred in a cylindrical plexiglass container of 5.6 cm diameter and 12 cm height. The curd was separated by the remaining fluid pushing a press composed of a metal mesh and a cellulose filter circle (Whatman™Grade 595 Qualitative Filter Circles, GE Healthcare, Little Chalfont, UK), taking care of not incorporating any air bubbles in the phantom. The degree of compression of the tofu-fluid mixture was manually adjusted along the cylinder axis, allowing the production of phantoms with different heights corresponding to different porosities, as shown in Figure 3.2. The coagulated curds compose the solid compartment of the poroelastic model, while the remaining fluid that permeates the solid matrix represents the fluid component of the model. The remaining fluid inside the phantom is assumed to have the same characteristics as the fluid on the sample's top.

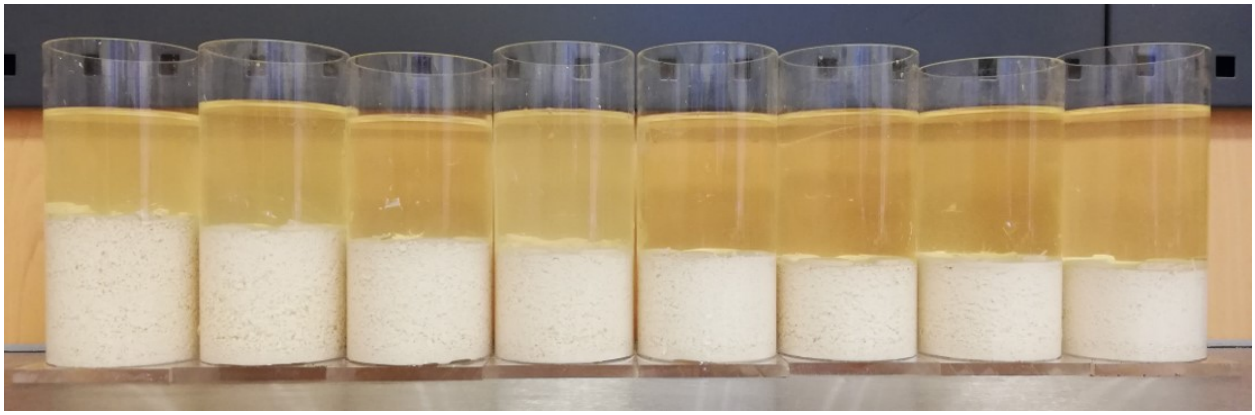

Figure 3.2: Eight tofu phantoms. Porosity decreases from left to right. Figure adapted from [1].

3.2 IR-MRE phantoms

3.2.1 Tofu phantoms

Three larger tofu samples were produced in a similar way as explained above. Therefore, a plexiglass cylinder with a diameter of 9.5 cm and 12 cm in height (3.3). The dimension of the head coil in which the samples were scanned limited the size of the container. Given this

constraint, to reduce the volume of the extracted fluid in relation to the volume of the tofu phantom, a third of the soy milk was evaporated prior to coagulation.

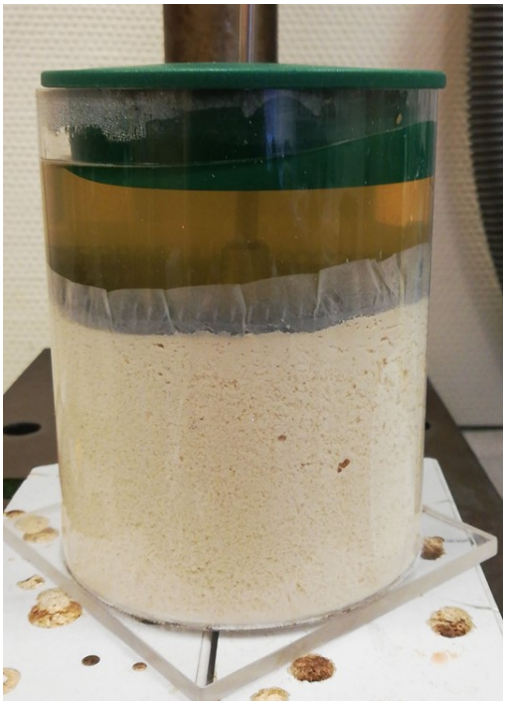

Figure 3.3: Larger phantom for IR-MRE. The press and the filter are still inside the vessel while the sample is cooling at room temperature.

3.3 Volunteers

21 healthy volunteers (6 females and 15 males) were examined by IR-MRI. The average age was 35 – 10 years, and the age range was 23 - 58 years. 7 healthy volunteers (4 females and 3 males) were investigated by IR-MRE. The average age was 33 – 6 years, and the age range was 25 - 41 years. The institutional review board approved the study. All participants gave written informed consent.

Chapter 4

Methods

4.1 IR-MRI/IR-MRE sequence

The diagram in Figure 4.1 shows the acquisition of ten slices with IR-MRE.

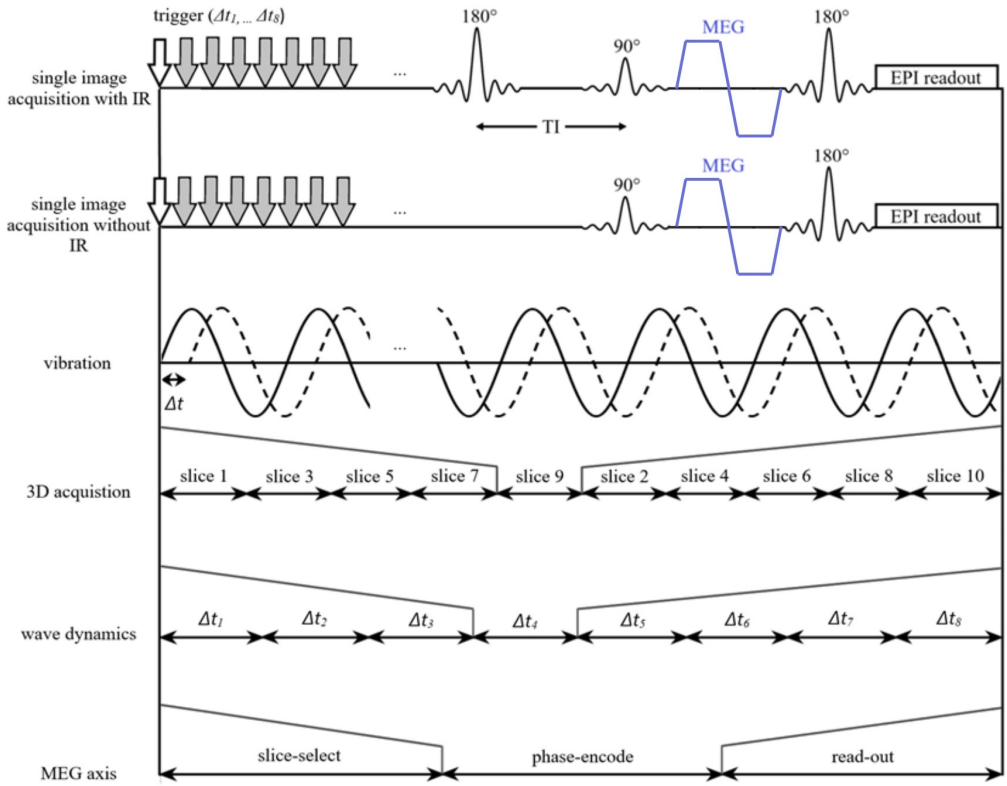

Figure 4.1: Simplified sequence diagram.

IR-MRI was performed based on the sequence shown in figure 6 but without the motion

encoding gradient (MEG, shown in blue) and without external vibration. The time between the slice-selective 180° inversion pulse and the slice-selective 90° excitation pulse denoted the inversion recovery time (TI). A slice-selective 180° refocusing pulse preceded the echo-planar imaging (EPI) readout. The MEG was 0^{th} moment nulled. The acquisition scheme was repeated identically for each imaging slice. In each IR-MRE sequence used in this study, to sample the full oscillation cycle, the relative oscillation phase between the continuous vibration and the MEG was incremented in eight equally spaced steps, and the MEG directions are three. As a reference, an MRE experiment can be performed using the same IR-MRE sequence, however, without IR. To produce images acquired at precisely the same time steps as in IR-MRE, the TI was substituted with a delay time but without inversion pulse.

4.2 Data acquisition

4.2.1 IR-MRI in phantoms

Phantom experiments were performed on a 1.5 Tesla MR scanner (Siemens Sonata, Erlangen, Germany) using a single-channel head coil. The fluid-fluid phantom was investigated by single-slice acquisitions of 32 × 88 matrix size and 1.85 × 1.85 × 1.90 mm^3 voxel volume. A first reference scan without inversion recovery was acquired, followed by acquisitions with inversion times from 120 to 520 ms with 50 ms increments, from 620 to 1020 ms with 100 ms increments, from 1220 to 3020 ms with 200 ms increments, and from 3400 to 5000 ms with 400 ms increments. Echo time (TE) and repetition time (TR) were 36 ms and 5150 ms, respectively. Pauses were inserted between measurements to ensure that the effective TR was higher than five times the T_1 of the undoped solution. Solid-fluid phantoms were investigated in 16 slices of 112 × 32 matrix size and 2 × 2 × 2 mm^3 voxel size with a 2 mm interslice gap. A first noninverted reference scan was acquired, followed by acquisitions with inversion times from 120 to 620 ms with 50 ms increments, from 720 to 1020 ms with 100 ms increments, from 1220 to 2020 ms with 200 ms increments, and from 2420 to 3620 ms with 400 ms increments. TE and TR were 35 ms and 60 sec, respectively, the latter being intentionally long to ensure full longitudinal relaxation between scans.

4.2.2 Measurement of porosity via draining

To obtain a second, independent measure of porosity, the eight tofu samples were drained after MRI. The whey permeate on top of the phantom was removed with care being taken to not remove any of the liquid from within the tofu. The volume of the tofu was quantified by measuring the height of the sample. Then the tofu was transferred to a ceramic filter funnel lined with a paper filter, and the liquid was allowed to drain out of the tofu. The drained liquid mass was measured every 5 minutes over one hour; the fluid extracted after one hour, together with the amount of fluid absorbed by the paper filter, was assumed to be a good estimator of the total free fluid that had been initially trapped in the tofu. The mass of water drained from a tofu sample after draining time t, denoted $m(t)$, was modeled as an exponential function

$$m(t; a, b, c) = a \cdot \left(1 - e^{-b \cdot t}\right) + c \tag{4.1}$$

The parameter a represents the fluid that asymptotically drains from the tofu, b the drainage rate, and c the amount of excess fluid that drains within the first few seconds of the process. Numerical values for a, b and c were estimated by fitting Eq. 4.1 to the sampled data. For all other phantoms, only the drained liquid after 10 minutes was measured. Assuming that b and c, are constant for all phantoms and $t10 = 10$ min and $m10$ is fluid weight drained after 10 minutes, the corresponding value of a can be estimated for any sample that has been drained for 10 minutes as

$$\tilde{a} = \frac{m_{10} - C}{1 - e^{-B \cdot t_{10}}}. \tag{4.2}$$

The asymptotic mass that represents the mass of the fluid compartment in each sample is calculated as

$$m_\infty = \tilde{a} + C. \tag{4.3}$$

Assuming that the whey permeate density is the same as the density of water, this method allows the quantification of the overall volume of the drained liquid phase of the tofu from a single data point acquired after 10 minutes of the draining process. The ratio of the fluid volume and the tofu volume is the resulting porosity.

4.2.3 Measurement of porosity via microscopy

Tofu cubes of approximately 1 cm^3 were excised from different locations in the remaining four tofu phantoms, fixed in paraformaldehyde, dehydrated for 48h in 20% sucrose solution,

and frozen in liquid nitrogen. 50 μm thick slices were prepared according to Kawamoto's film method [50] using a cryostat (Leica CM 1850 UV, Nussloch, Germany). Ten slices for each sample were analyzed using light transmission microscopy (Zeiss Axio Observer for Biology, Jena, Germany).

4.2.4 IR-MRI in *in vivo* human brain

IR-MRI experiments were performed on a 3 Tesla MR scanner (Siemens Trio, Erlangen, Germany) using a 12-channel head coil. For each volunteer, 5 slices were acquired of 100 $\times$ 100 matrix size and 2 $\times$ 2 $\times$ 2 mm^3 voxel volume. A first reference scan without inversion recovery was acquired, followed by acquisitions with inversion times from 120 to 510 ms with 130 ms increments, from 900 to 19000 ms with 200 ms increments, from 2200 to 3400 ms with 200 ms increments and from 3800 to 5000 ms with 400 ms increments. TE and TR were 45 ms and 40550 ms, respectively. An additional Magnetization Prepared - RApid Gradient Echo (MP-RAGE) sequence was acquired for anatomical reference.

4.2.5 IR-MRI/IR-MRE in tofu phantoms

IR-MRI/IR-MRE experiments were performed on a 3 Tesla MR scanner (Siemens Prisma^{Fit}, Erlangen, Germany) using a 32-channel head coil. The IR-MRI and IR-MRE acquisitions are done in the same session, one after the other. Two pressurized air drivers were placed side by side under the tofu sample. IR-MRI was performed first: 5 slices were of 108 $\times$ 100 matrix size and 2 $\times$ 2 $\times$ 2 mm^3 voxel volume. A first reference scan without inversion recovery was acquired, followed by acquisitions with inversion times 100 ms, from 200 to 1200 ms with 200 ms increments, 1600 ms, 2000 ms, from 2500 to 6000 ms with 500 ms increments. TE and TR) were 65 ms and 17380 ms, respectively. Two synchronized IR-MRE were performed, once with no inversion recovery and secondly with TI equal to the nulling TI of the fluid compartment. The two air drivers attached to the inside of the head coil, as shown in Fig. 4.2, were operated in opposed-phase mode at a mechanical frequency of 20 Hz. The motion-encoding gradient was 39.53 Hz with 20 mT/m.

4.2.6 IR-MRI/IR-MRE in *in vivo* human brain

The in *in vivo* IR-MRI/IR-MRE experiments were performed similarly to the phantom experiment. In this setting, the air bottles are positioned under the volunteer's head, which was fixated with cushions to avoid any movement. In IR-MRE the TI = 2900 ms, which corresponded to the nulling TI of the CSF signal. The TR was set to 20000 ms due to the longer relaxation time of CSF. A T_1-weighted MP-RAGE sequence supplemented the *in vivo* scanning session for segmentation. The total scan time per volunteer was approx. 30 minutes.

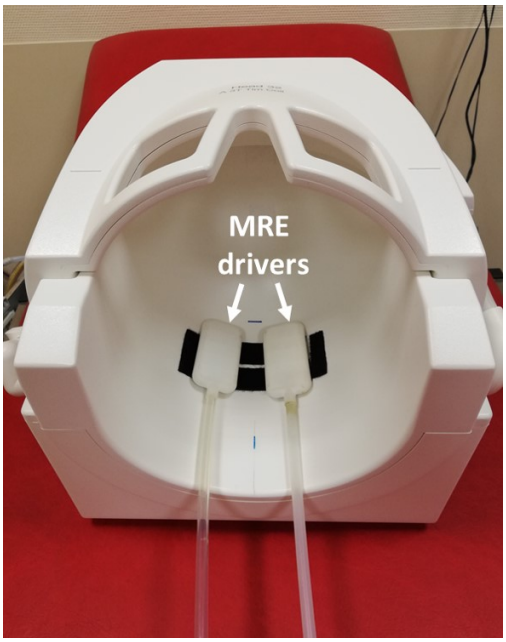

Figure 4.2: Actuators set up.

4.3 Data processing

The fluid-fluid phantom data were processed in two stages. The first step was estimating T_1 relaxation time, signal amplitude I, and noise offset C by fitting the mono-exponential Equation 2.28 to the single-compartment IR-MRI signals within each of the two compartments. Afterward, the signal of multiple ROIs, each composed of voxels from both compartments at different ratios, was averaged into supervoxels, emulating the biphasic signal from voxels with different porosities as simplified in Figure 4.3. Since usually in poroelastic media the fluid compartment has a longer T_1 than the solid compartment, we refer to the saline solution, which has longer T_1, as the fluid compartment and the Gd-doped solution, which has

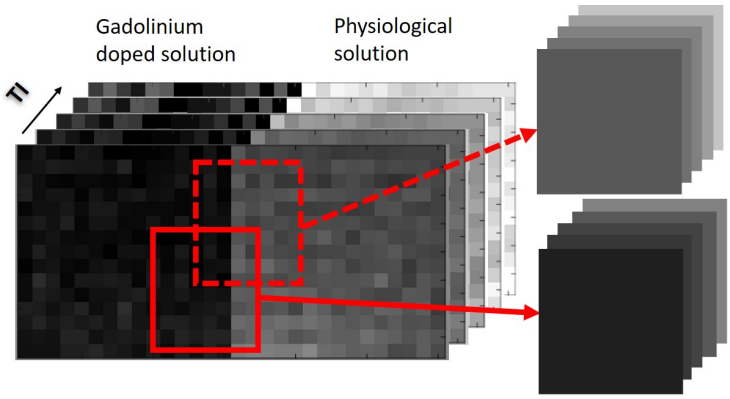

Figure 4.3: Emulation of supervoxels. Figure adapted from [1].

a shorter T_1, as the solid compartment. Consequently, for each ROI, the fraction of voxels from the long-T_1 compartment was taken as ground truth porosity. As previously clarified in the Theory chapter, T_1 and I values of the fluid compartment needed to be quantified separately and used as input variables for our biphasic model to improve fitting stability. The fitting of either the full Equation 2.28 or reduced Equation 2.30 to the biexponential relaxation signal led to the estimation of IR-MRI porosity of the biphasic supervoxel and T_1 times of the gadolinium doped solution.

Similarly, solid-fluid tofu phantoms data were analyzed in two steps. First, the IR-MRI signal decay of the excess fluid on top of the phantom was fitted to the monophasic model (Eq. 2.27) to extract T_1^f and I^f. Second, these parameters were used as constants for the biexponential fits (Eq.2.30) of the biphasic tofu IR-MRI signal on a voxel basis, leading to the estimation of porosity and T_1^s maps.

In addition to the alternative measure of porosity obtained draining the tofu samples, a further estimation of porosity was derived from the acquired microscopy slides images. From these micrographs, average porosity was computed by first segmenting the tissue image and then calculating the ratio of the pore area over the total area.

The same strategy applied for tofu IR-MRI data was used in *in vivo* IR-MRI data post-processing, where CSF properties were assumed as the fluid compartment characteristics. Hence, the CSF IR-MRI signal in the ventricles was first analyzed by monoexponential fitting (Equation 2.27) for determination of T_1^f and I^f and then, using these values as constants, the fitting the biexponential signal relaxation of the IR-MRI (Eq. 2.30) was applied to the brain images voxel-by-voxel.

In the IR-MRI/IR-MRE experiments, the IR-MRI images were processed similarly as in the

previous IR-MRI experiment to estimate f and T_1^s maps aligned with the IR-MRE scans. Equations 2.32 and 2.33 were solved to obtain the displacement field of the fluid and solid compartments. The displacement field of the fluid compartment, being present in lower volumes than the solid, has a lower SNR than the solid displacement field. Therefore, a Butterworth low-pass filter was applied with a cutoff of 50 m^{-1} and order 1. The fluid and solid displacement fields curl was determined using central differences for interior data points and single-sided differences at the endpoints, and ρ_{12} was estimated by solving Equation 2.23, assuming ρ_f=1000 kg/m^3, equal to the density of water.

4.4 Statistical analysis

All statistical tests were performed in Matlab (Mathwork Inc., Natick, USA, version 2018). In IR-MRI phantom experiments, Student's t-tests assuming significance of $P = 0.005$ were performed to compare IR-MRI porosity with the alternative measurement of porosity. In the IR-MRI *in vivo* experiments, grey matter (GM), white matter (WM), and CSF probability maps were generated based on MP-RAGE scans using Statistical Parametric Mapping (SPM) 12 software (The Wellcome Centre for Human Neuroimaging, London, UK) [51]. A voxel was designated to a compartment if its probability value of being composed of that medium exceeded 80%. The coregistration of IR-MRI and MP-RAGE scans allowed the segmentation of the resulting porosity and T_1 maps in WM, GM, and CSF. Group mean values and standard deviations (SD) of CSF T_1 and monophasic T_1, compartmental T_1, and porosity of GM and WM were computed. A paired Student's t-test analysis was performed for average porosity and normalized solid T_1 values of WM and GM in each volunteer. All T_1 and porosity values with a coefficient of determination $R^2 < 0.9$ were discarded. In the IR-MRE phantom and *in vivo* studies, the magnitude and oscillation phase of the curl components after Fourier transform were analyzed separately. To test if the magnitude of the curl component of the solid compartment is higher than the amplitude of the fluid component, a right-tail t-test was performed. To verify the assumption that solid and fluid compartments are phase-locked, the oscillation phase from one compartment was plotted versus the oscillation phase of the other one on a per-voxel basis, and linear regression was estimated for each sample and each volunteer. Due to the instabilities caused by the subtraction at the denominator of the rearranged Equation 2.23, $\rho_{12} = \frac{f\rho^f \ddot{c}^f}{\ddot{c}f - \ddot{c}^s}$, voxels with

$|\ddot{\mathbf{c}}^s| < 5 \cdot 10^{-4}$ were removed from the statistical analysis. Median and interquartile intervals were determined for each tofu sample and in the *in vivo* brain for WM and GM separately.

Chapter 5

Results

5.1 IR-MRI in phantoms

Figure 5.1 displays IR-MRI results obtained in the fluid-fluid phantom based on the full model (Eq. 2.28) and the reduced model (Eq. 2.30). Error bars indicate that the standard error of estimated parameters is smaller for the reduced Eq. 2.30 (mean standard error of f: $\pm$ 0.007, of T_1^s: $\pm$ 22 ms) than for the full Eq. 2.28 (mean standard error of f: $\pm$ 0.03, of T_1^s: $\pm$ 63 ms). Eq. 2.30 tends to underestimate T_1^s and to overestimate porosity at higher ground truth porosities. At ground truth porosities higher than 0.8, we evaluated an overestimation of f of 4 % and of T_1^s of %. Nevertheless, porosities reconstructed using the reduced Equation 2.30 were in excellent agreement with ground truth values ($R = 1$, $P = 0$, porosity mean residual error: $\pm$ 0.02).

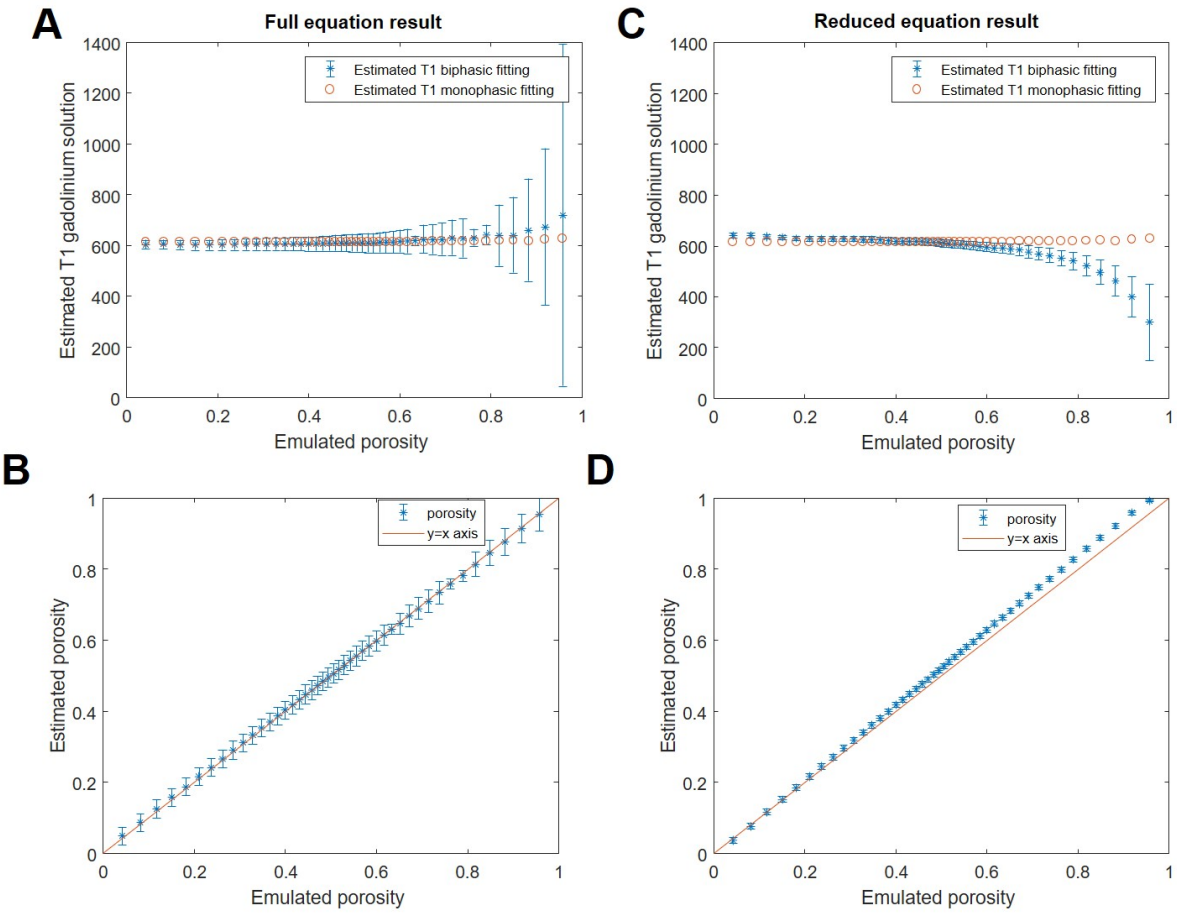

Figure 5.1: IR-MRI porosity results compared to the emulated values. Figure from [1].

The microscopy slides confirmed that the solid-fluid phantoms had porous structures (Fig. 5.2). Microscopy porosities in the different sampled regions resulted in 0.11 ± 0.03, 0.13 ± 0.05, and 0.19 ± 0.04,, thus indicating an inhomogeneous porous structure on the length scales of these micrographs.

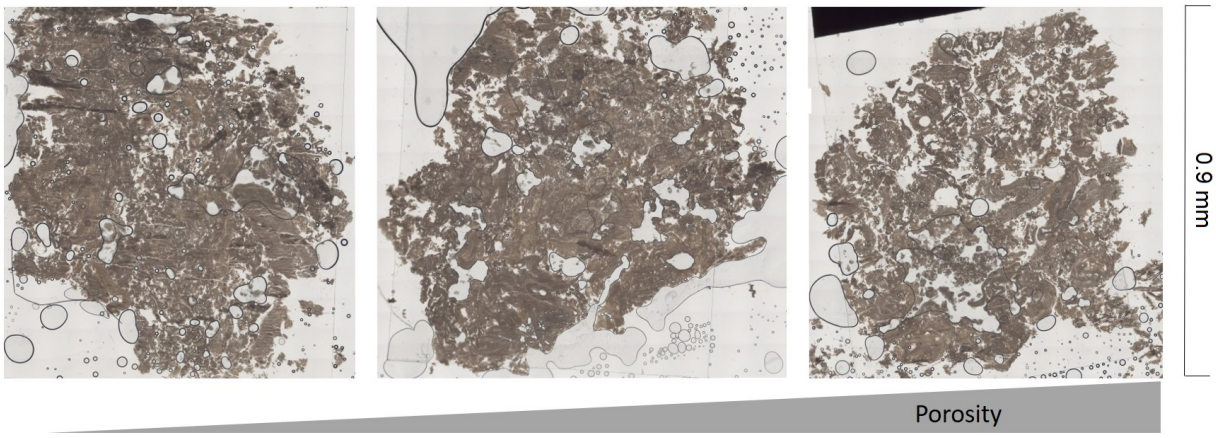

Figure 5.2: Examples of microscopy slides. Figure adapted from [1].

The microscopy data show a significant correlation with IR-MRI porosity ($R = 0.99$, $P < 0.01$) (Fig. 5.3).

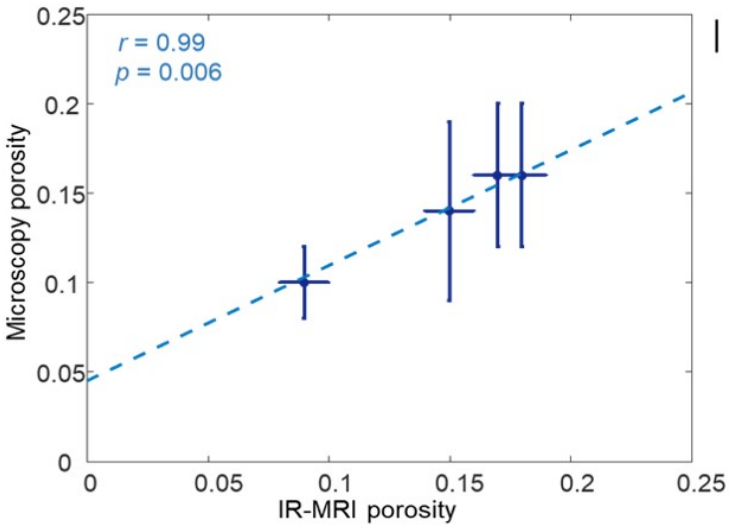

Figure 5.3: Spatially averaged IR-MRI porosity of four samples compared to porosity measured by microscopy. Figure from [1].

Figure 5.4 shows porosity maps of the central slice of each tofu sample reconstructed from IR-MRI using Eq. 2.30. Mean porosities varied from 0.12 to 0.27. Porosity derived by draining tofu samples went from 0.08 to 0.30, indicating good agreement of IR-MRI with reference porosity values.

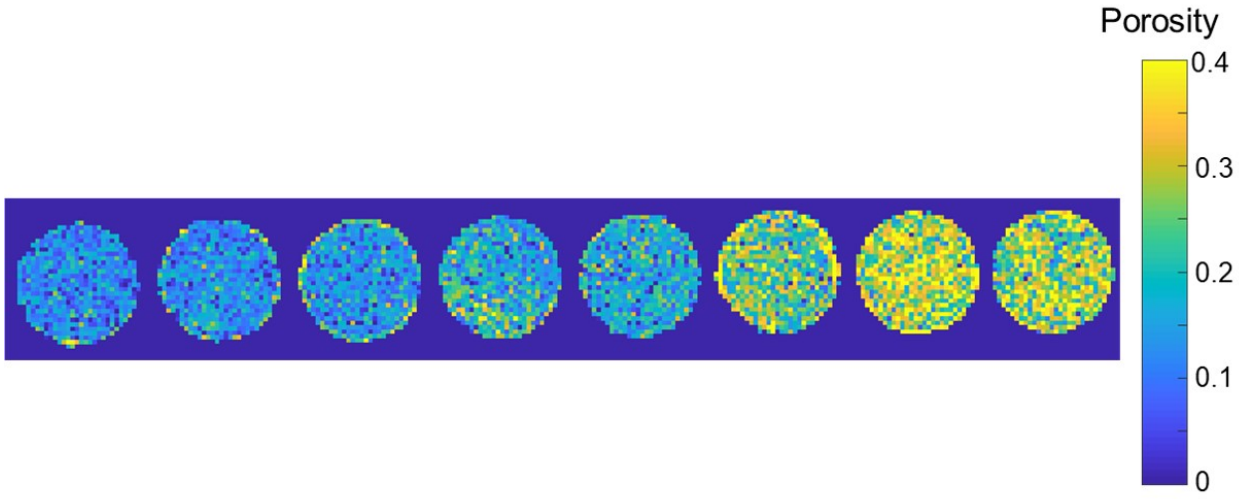

Figure 5.4: Porosity maps of the central slice of each tofu phantom in Fig. 3.2. Figure adapted from [1].

Figure 5.5 presents spatially averaged IR-MRI porosity values versus draining porosity [1]. The error bars of IR-MRI porosity results represent the standard deviation of porosity across slices, while the draining porosity error bars represent the measurement error. Porosity estimated with IR-MRI is correlated with draining porosity ($R = 0.99$, $P < 10^{-5}$). Due to water adhesion, some of the free water is retained in the tofu sample and, therefore, draining porosity is prone to underestimation, especially at low porosities [1].

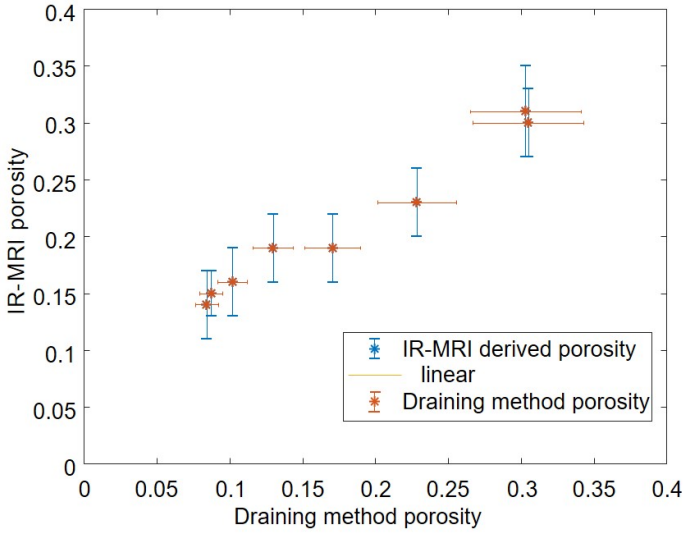

Figure 5.5: IR-MRI porosity compared to draining porosity. Figure adapted from [1].

5.2 *In vivo* brain study IR-MRI

Figure 5.6 shows an example of IR-MRI porosity map and solid-tissue T_1 map of *in vivo* brain. Average CSF T_1 across all volunteers resulted in 4257 ± 157 ms, while T_1^s and f were 1172 ± 36 ms and 0.14 ± 0.02 in GM and 800 ± 15 ms and 0.05 ± 0.01 in WM, respectively (Figure 5.7).

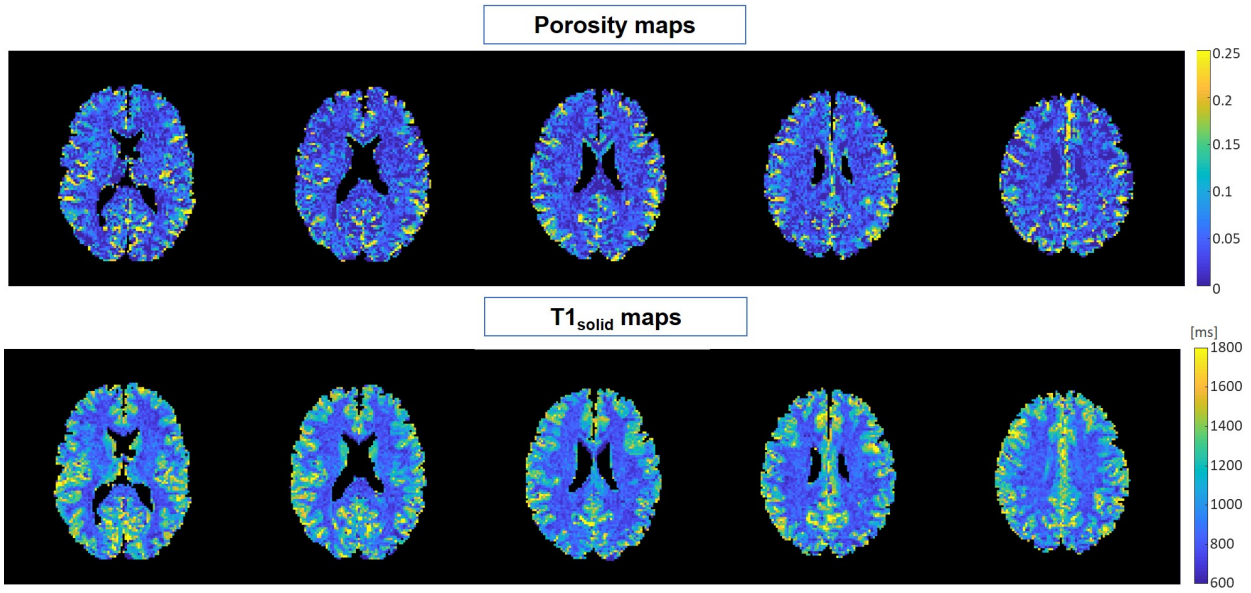

Figure 5.6: Porosity and T_1 maps of the solid compartment of a healthy volunteer brain. Figure adapted from [1].

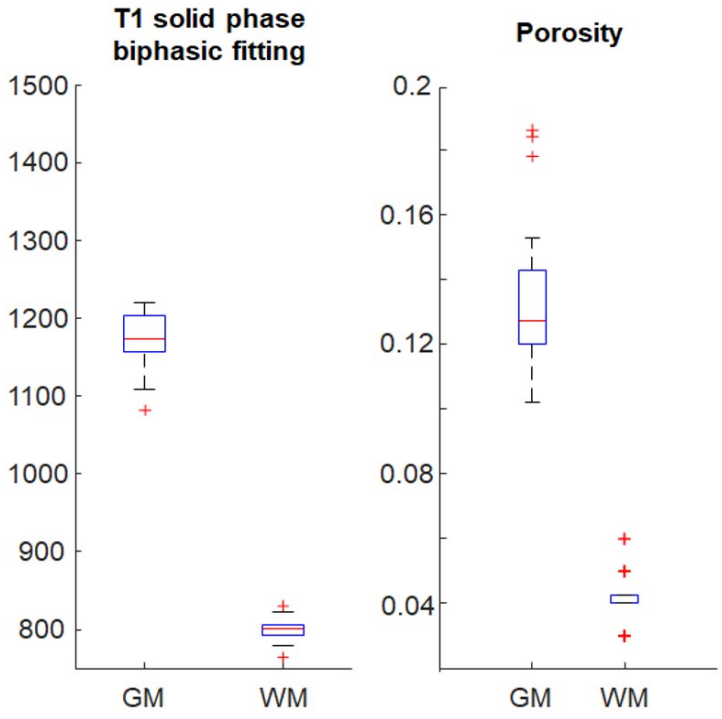

Figure 5.7: Variation of the average porosity and T_1 of the solid compartment in *in vivo* brain. Figure from [1].

These values were statistically significantly different between GM and WM (all $P < 10^{-16}$). However, the different shapes of the porosity and T_1^s distributions show that these

two parameters represent independent information, as shown in Figure 5.8. These charts illustrate that T_1^s values are distributed with two distinct peaks corresponding to GM and WM, whereas porosity shows a more continuous single-peaked wider distribution [1].

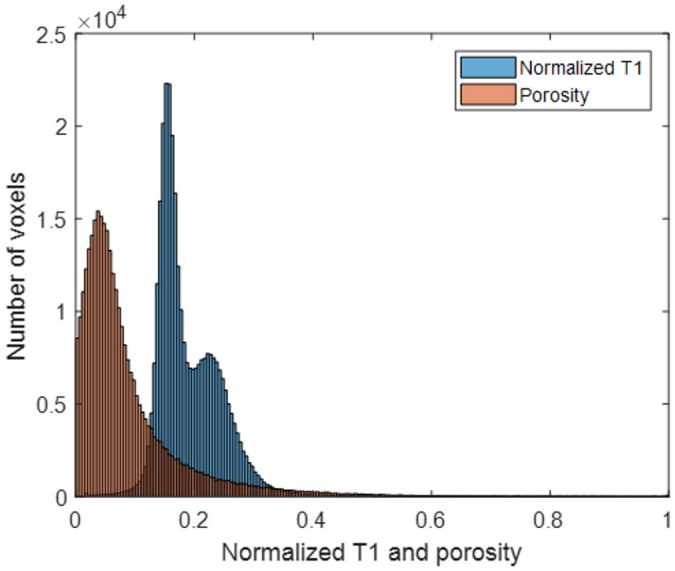

Figure 5.8: Normalized porosity and T_1 distribution. Figure from [1].

5.3 IR-MRI/IR-MRE in tofu phantoms

The average shear wave amplitude in the fluid compartment resulted lower than in the solid ($P < 0.05$), while voxel-by-voxel linear fitting of the phases of c^f and c^s showed an average slope of 0.93 ± 0.07, offset of 0.10 ± 0.01, and $R^2 = 0.90 \pm 0.07$. For example, you can see the comparison of the shear wave amplitudes maps and the fitting of the corresponding phases of one sample in Figures 5.9 and 5.10.

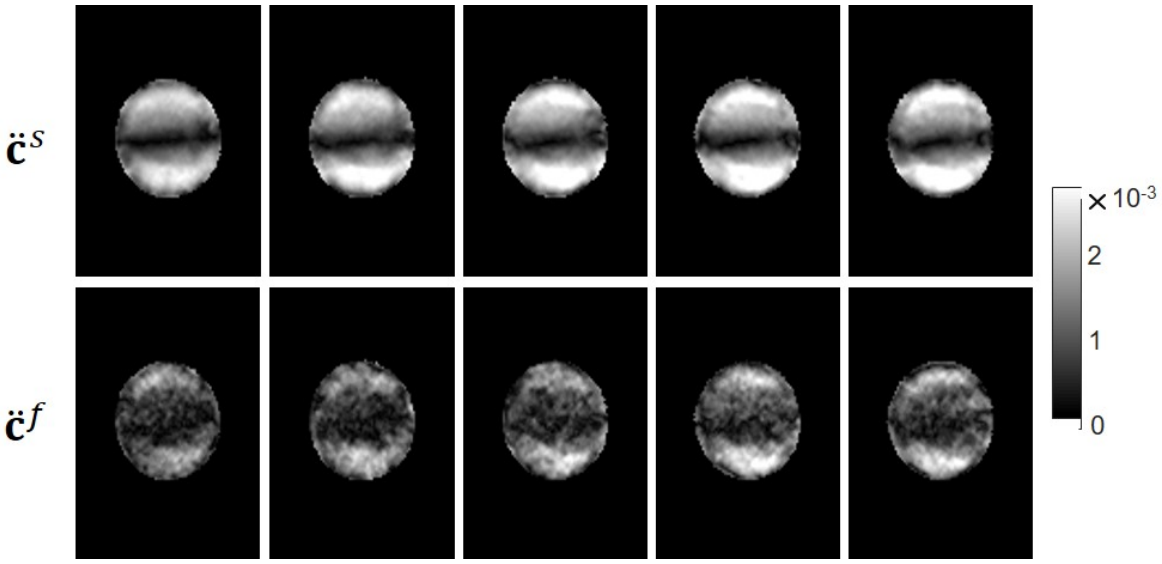

Figure 5.9: Magnitude images of the through-plane component of the curl of the solid (first row) and fluid compartment (second row) of one tofu sample. Figure adapted from [1].

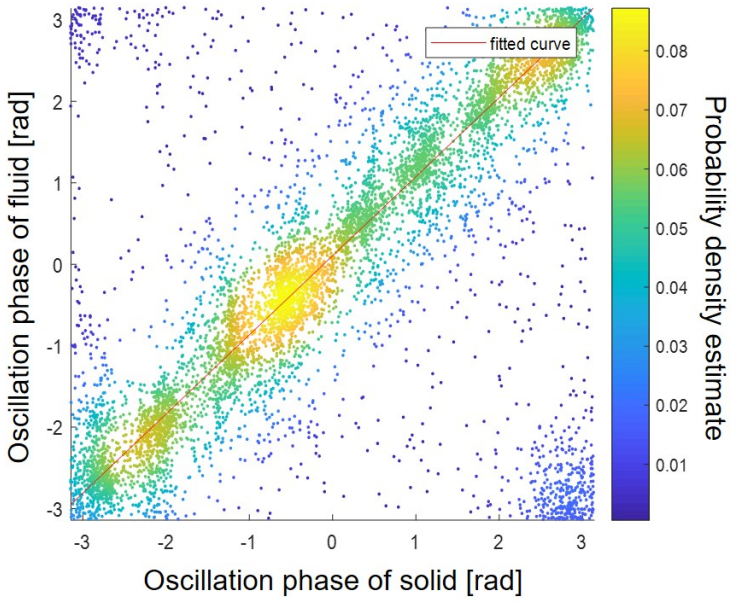

Figure 5.10: Voxel-by-voxel plot of solid and fluid curl phase. Figure adapted from [1].

Maps of ρ_{12} were determined for each slice. The ρ_{12} maps and porosity map of the sample represented in the previous two images are shown in Figure 5.11. The distribution of ρ_{12} was strongly asymmetrical (Figure 5.12), therefore median and interquartile range were determined with -114 (-318, -24) kg/m^3, -117 (-330, -21) kg/m^3, and -190 (-511, -22) kg/m^3 for the three tofu phantoms. The distribution between ρ_{12} and f was not significantly correlated [1].

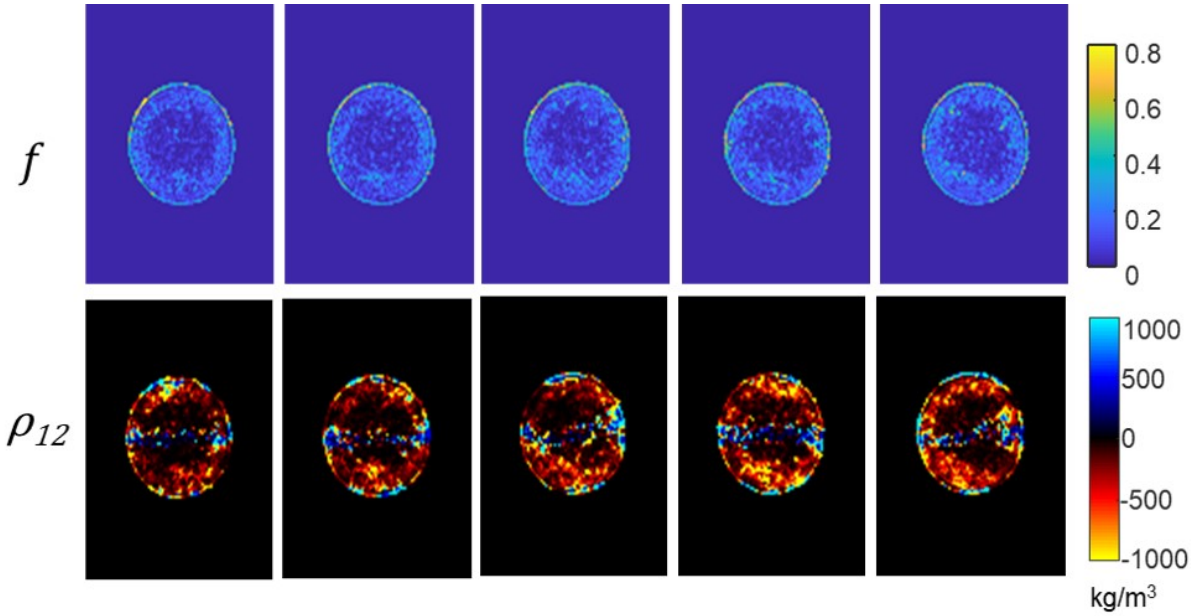

Figure 5.11: Porosity (first row) and ρ_{12} maps (second row) of a tofu sample. Figure adapted from [1].

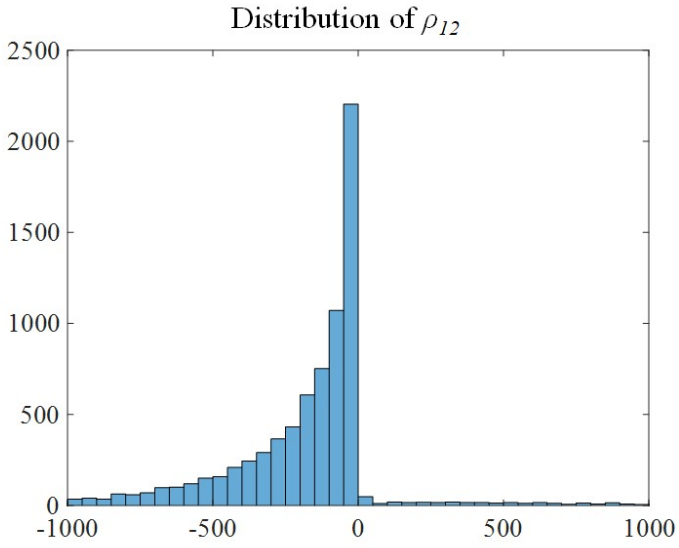

Figure 5.12: Histogram of the distribution of ρ_{12} values in the tofu phantom. Figure from [1].

5.4 IR-MRI/IR-MRE in *in vivo* human brain

Figure 5.13 shows an example of the curl of the solid and fluid compartment in the human brain. In each volunteer, the average shear wave amplitude in the solid is higher than in the fluid ($P < 0.05$). Voxel-by-voxel linear fitting of the phases of $\ddot{\mathbf{c}}^f$ and $\ddot{\mathbf{c}}^s$ resulted in an average slope of 0.98 ± 0.01, offset of 0.01 ± 0.09, and $R^2 = 0.950.02$. The phase data fitting generated from the same volunteer as in Figure 5.13 is shown in Figure 5.14. Maps of ρ_{12} were generated for each slice (Figure 22). The group average medians resulted in -22 ± 29 kg/m^3 and -38 ± 4 kg/m^3 for GM and WM, respectively. The distribution between ρ_{12} and f were not significantly correlated (Figure 23) [1].

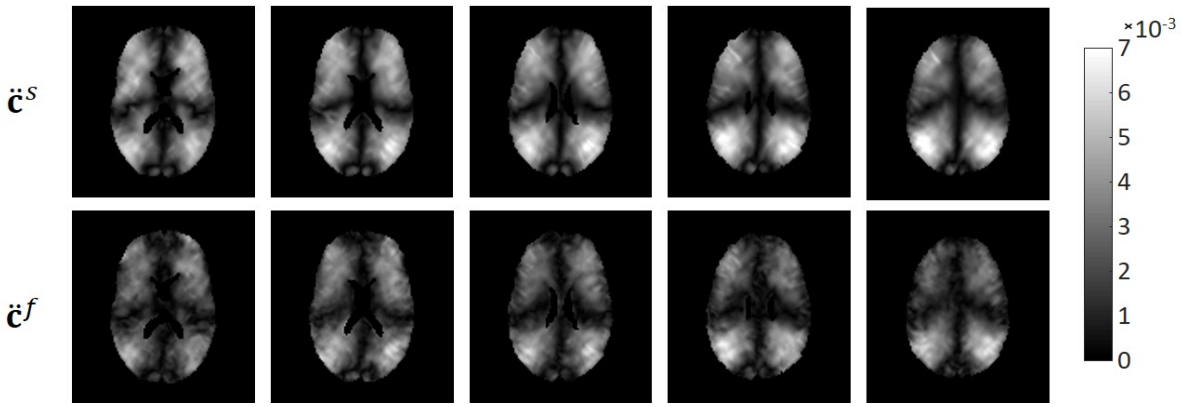

Figure 5.13: Magnitude of the curl of the solid and fluid displacement field. Figure adapted from [1].

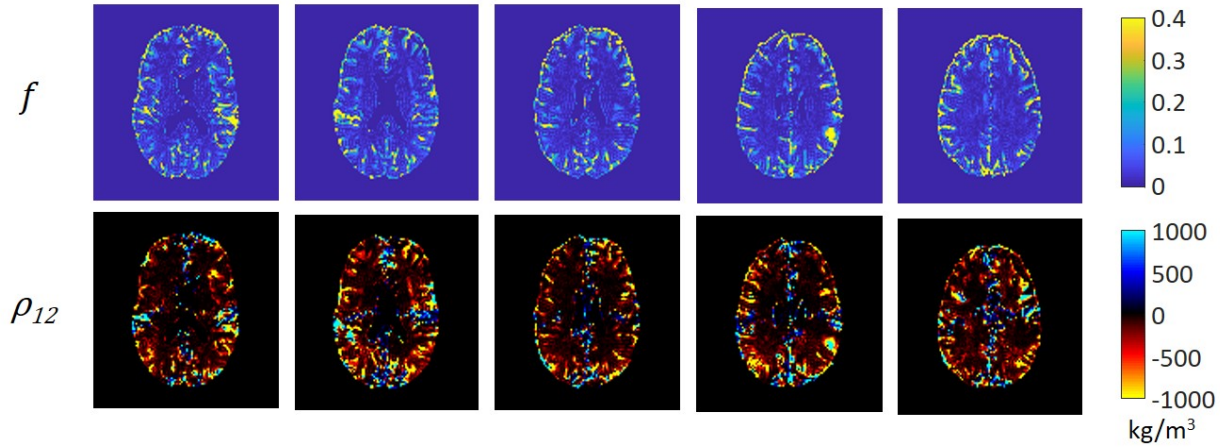

Figure 5.14: Porosity and coupling density map of the slices represented in 5.13. Figure adapted from [1].

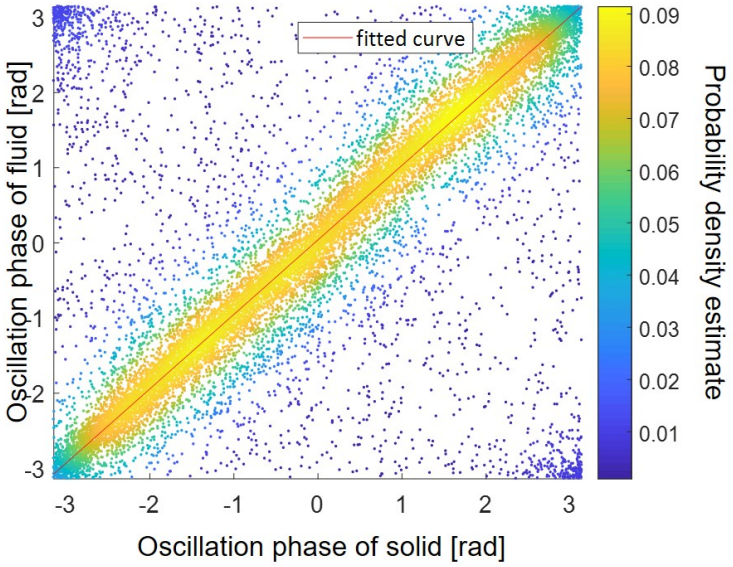

Figure 5.15: Probability density estimate of the plot of the fluid oscillation phase vs. the solid oscillation phase. Figure adapted from [1].

Chapter 6

Discussion

Estimation of porosity using the T_1 relaxation technique introduced here is a new method. Therefore, the first step was to demonstrate and validate consistency of IR-MRI in phantom studies.

The fluid-fluid phantom experiment represented a highly simplified setting since the phantom consisted of an emulated porosity composed of two averaged monophasic media signals measured at different TI. The solution of the full model led to stable results over a wide range of porosities ($f < 0.9$). However, the simplified model produced comparable values in a more constrained range of porosities ($f < 0.5$) with a smaller standard deviation (Figure 5.1). In most biological soft tissues, porosity values are below 50%, as, for example, in the brain where previous studies report a porosity on the order of 20% [38]. Since this value is clearly below 50%, we considered the simplified solution of the biphasic fitting to be the most suitable approach for the scope of this project.

Our fluid-fluid phantom results confirmed the feasibility of the sequence and fitting method for high-SNR scenarios. To address more realistic SNR values and tissue structures, further experiments involving tissue-mimicking phantoms were necessary. Tofu is a convenient and commonly used phantom for poroelastography [35, 52]. The need for phantoms with different porosities and optimal MRI characteristics motivated the development of a protocol for producing our own tofu phantoms. Usually, simple calcium salts or nigari are used to coagulate soy milk but they affect MRI relaxation times. Therefore, acetic acid was used as a coagulating agent. The standard production method yielded air bubbles in the tofu slabs, which affected magnetic field susceptibilities, leading to distortions in our EPI scans. With our method, the excess fluid was separated from the soybean curd using a metal mesh

of exactly the same size as the container. With this mesh, pressure was applied until we reached the desired volume of the tofu slab while keeping it covered with the remaining fluid to avoid the formation of air cavities(Figure 3.3).

As revealed by microscopy, the tofu samples were composed of a matrix with highly heterogeneous pores on the millimeter scale (Figure 5.2). This feature of the tissue imposes challenges in defining a ground truth porosity based on microscopy. Furthermore, the method that allows the production of microscopy slides is highly complex due to the relatively delicate structure of the tofu matrix and involves preparation steps such as snap-freezing, which potentially affects porosity quantification. Thus, the drainage method was preferred to microscopy. Specifically, drainage combined with exponential extrapolation led to more consistent porosity estimations than fluid volume measurement after a fixed time. However, overall, the retention of small amounts of fluid within the hydrophilic tofu matrix caused underestimation of the draining porosity, which affected phantoms with lower porosities more markedly.

Many studies show that, in the brain, magnetization transfer (MT) can interfere with the measurement of T_1 times [53, 54]. In order to quantify the MT effect on porosity estimates, we compared the results of standard IR-MRI in our brain protocol with a modified version, where only two slices were acquired with an excessively long idle time (60 s) between slice acquisitions to allow complete proton T1 relaxation between successive RF excitations. The two measurements were performed in the same session, taking care to ensure immobilization of the volunteer's head. Analysis of the data acquired in three volunteers revealed that differences between these two scans caused uncertainty in the porosity estimation of $(17 \pm 14)\cdot^{-3}$, $(43 \pm 15)\cdot^{-3}$, and $(44 \pm 35)\cdot 10^{-3}$ in homogeneous WM regions (Figure 6.1). These results suggest that MT leads to deviations of less than 5% in porosity quantification, which does not limit the applicability of the proposed method. Nevertheless, use of an MR sequence corrected for MT would improve the accuracy of IR-MRI-based porosity quantification.

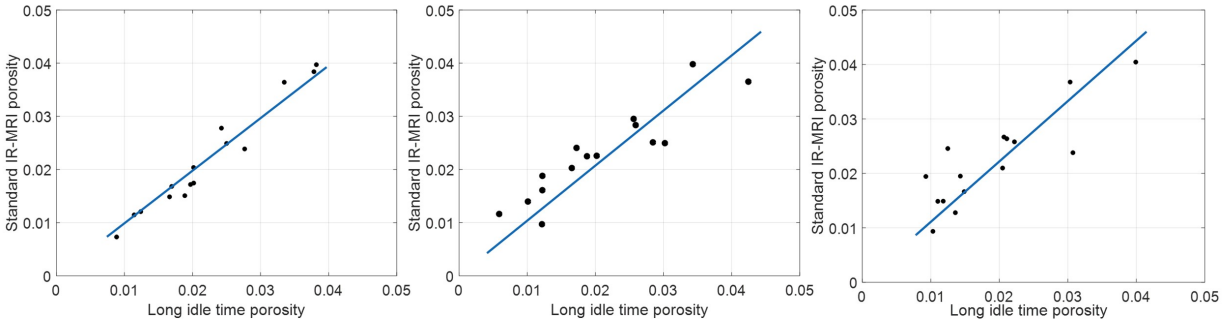

Figure 6.1: Comparison of porosity in homogeneous areas of WM obtained with standard IR-MRI and long-idle time IR-MRI. Figure from [1].

In the *in vivo* brain study, CSF was defined as the fluid compartment of the poroelastic medium that represents the brain tissue because its properties are similar to those of extracellular fluid [41]. For *in vivo* rat brain, CSF was reported to represent 15% of WM and 30% of GM [41]. Arguably, blood is another fluid that permeates the brain, but the brain vascular volume doesn't exceed 1.5% in WM and 3% in GM [55]. Consequently, blood, which has a T_1 time that is closer to that of solid brain tissue but significantly shorter than that of CSF, is assigned to the solid compartment. This introduces a systematic bias and underestimation of porosity. Additionally to blood, bound water within the ECS exhibits much shorter T_1 times than free CSF, and therefore, it is also considered part of the solid compartment. Nevertheless, this is consistent with the mechanical description of the poroelastic medium, where the fluid compartment is free to flow through the pores. As a result, the porosity of the brain measured by our IR-MRI method is lower than the volume fractions reported in the aforementioned studies and should instead be interpreted as CSF porosity. In the statistical analysis of our *in vivo* brain results, the quasi-monophasic edge cases, as $f \to 0$ and $f \to 1$, were excluded due to the fitting equation collapsing to the two extreme results, $f = 0$ and $f = 1$. Therefore, the ventricles and voxels with $f < 10^{-4}$ were excluded from analysis. Almost all voxels that collapsed to zero were found to be irregularly located in the WM. A preliminary new fitting strategy based on adaptive smoothing [56] has shown promising results in correcting these voxels taking advantage of the relative uniformity of WM tissue.

The resulting distribution of the estimated parameters shows a single-peak histogram for porosity and a two-peak histogram for T_1, corresponding to the T_1 peaks for WM and GM (Figure 5.8). Therefore, there is no monotonous mapping between the two quantities, and

thus, they can be considered independent.

Poroelastic theory predicts in-phase oscillation of the two compartments with higher amplitude in the solid compartment than in the fluid and, therefore, a resulting negative value of ρ_{12} [39]. The results of our IR-MRE, both in tofu and *in vivo* brain, agree with this theoretical prediction, except in the area of approximately zero deflection amplitudes, e.g., near standing nodes, as shown in Figures 5.13 and 5.14. In these regions, any minimal error can affect the difference between the curl of the fluid and solid compartment, which is in the denominator of the formula that defines ρ_{12}, and therefore it can have a major influence on the resulting coupling density.

As in IR-MRI, TR was set to values long enough to ensure full longitudinal relaxation of the MRI signal. In both tofu and *in vivo* experiments, perfect synchronicity between the time steps acquired with and without inversion recovery is essential. To this end, a delay of the same duration as the nulling of TI of the fluid compartment was added to each scan without an inversion recovery pulse. This extended TR, along with the added delay in the scans without inversion recovery, resulted in long acquisition times, which increase the risk of spatial mismatch due to head movement. To reduce motion, the head of the volunteer was carefully fixed with cushions inside the head coil, and additional alignments were required.

Coupling density can be defined in terms of pore geometry [57]

$$\rho_{12} = -(T-1)f\rho^{\text{fluid}} \tag{6.1}$$

where T is the tortuosity of the pore space. A curve's tortuosity can be defined as the length of the curve divided by the distance of its endpoints. The tortuosity of a straight line is 1, while for any other curve $T > 1$ (Figure 2.27).

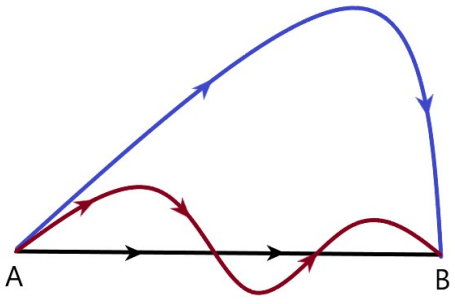

Figure 6.2: Tortuosity of the black line is 1 while it is >1 for the other two lines.

In our context, given a fixed voxel volume, tortuosity translates into a measure of the complexity of pore space geometry. Therefore, in voxels characterized by very low porosities

and thus minimal pore size, tortuosity can be relatively low, and its impact on the definition of ρ_{12} is very reduced due to $f \to 0$. In pores where f is higher, tortuosity has a higher impact on ρ_{12}, which is reflected in the higher variability of ρ_{12} at higher porosity, as illustrated in Figure 6.3, where the ρ_{12} and f of a tofu phantom are shown.

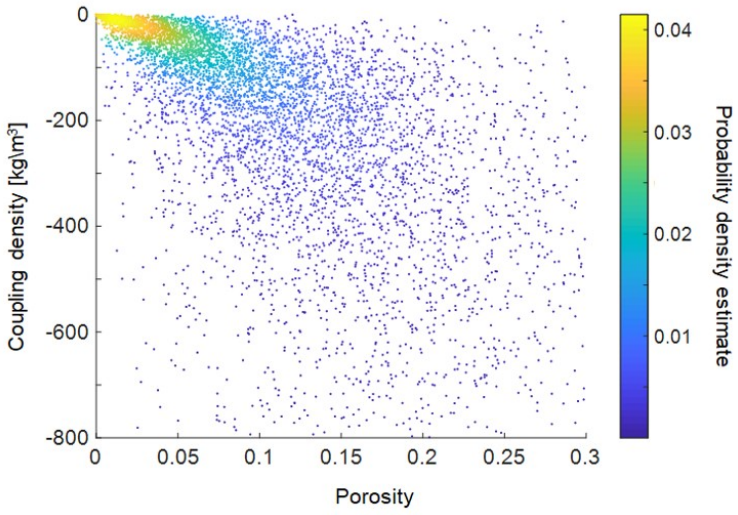

Figure 6.3: Distribution of porosity vs. coupling density of a tofu phantom.

For the first time, our study establishes the technical key methods necessary to estimate porosity and disentangle the externally induced fluid and solid displacement fields in the *in vivo* human brain modeled as a poroelastic medium. Porosity represents information below clinical resolution allowed, for the first time, estimation of coupling density, which was negative, as predicted by poroelastic theory.

IR-MRI porosity mapping provides richer details on porous tissue structures compared to average results reported by previous poroelastography studies [38]. Unlike the standard viscoelastic model used in MRE, the porous model considers that biphasic tissue displays compressive properties even though individual components are fully incompressible. Previous poro-MRE studies have focused on compression properties of porous media [58, 59]. In this work, we focused on shear waves since they can be readily separated from compression waves by using the curl operator. Vice versa, compression waves have to be separated by the divergence operator, which requires full 3D wave fields without inter-slice phase artifacts [60]. Furthermore, separation of shear waves is easier to accomplish based on the Biot model for poroelastic wave propagation, which predicts one shear wave mode instead of two com-

pression wave modes [45].

Changes in fluid content and tissue pressure in the brain are essential parameters assessing the progression of edema, hydrocephalus, or cancer. For example, hydrocephalus has been investigated within the poroelasticity theoretical framework in several studies [61, 62, 63, 64]. Porosity combined with the separation of displacement fields is a promising step towards non-invasive *in vivo* measurement of pressure, especially intracranial pressure (ICP) and should be explored further in future studies. At present, no method has demonstrated sufficient data accuracy for allowing noninvasive monitoring in clinical routine [65].

In the literature, many soft tissues such as the brain or liver are modeled as poroelastic media [27, 66]. Our study may add essential quantitative information on soft tissue structure and how its different compartments interact. For example, IR-MRE might improve the analysis of solid-fluid behavior of brain tumors [44]. Liver tissue can also be modeled as a poroelastic medium permeated by blood. Ongoing investigations of *ex vivo* and *in vivo* liver tissue modeled as a poroelastic medium underscore the relevance of IR-MRE.

Long acquisition times of IR-MRI/IR-MRE are currently addressed by further pulse sequence optimization. For example, techniques such as 3D slab IR preparation and 3D multiband readout permit a time-efficient preparation and sampling scheme. Furthermore, tissue-specific mathematical analysis based on the range of expected T_1 times is explored to optimize and reduce the number of acquired images by IR-MRI. Once available, fast IR-MRI/IR-MRE could be applied for multifrequency stimulation and acquisition and might allow clinical application of the method.

Another study has investigated an IR-MRE application for *in vivo* brain imaging using viscoelastic model-based inversion instead of the poroelastic one [67]. In this study, we have shown that nulling the CSF signal reduces blurring and biased stiffness in CSF-adjacent areas, and, therefore, allows more precise estimation of shear wave stiffness in cortical regions. Furthermore, it avoids the apparent ventricles enlargement, common in standard MRE.

This study has a few limitations.

First, our biphasic model comprises only one fluid compartment with homogeneous characteristics through the medium and a solid compartment homogeneous in each voxel. Both compartments are characterized by a sharp peak in the relaxation time spectrum. These assumptions do not consider proton exchanges across interfaces between different pools of

protons [68], magnetization transfer, continuous T_1 spectra, proton interaction-based widening of the relative T_1 peaks, and variations of the fluid properties across the medium.
Second, biexponential porosity estimation is ill-conditioned for $f \to 0$ or $f \to 1$. Nevertheless, fluid-filled spaces were segmented and excluded from porosity analysis.
Finally, any slight movement of the volunteer's head could lead to a spatial mismatch between porosity maps or inverted and noninverted MRE acquisitions, which would require further realignment steps [69]. Each volunteers' head position was fixed with thick cushions to minimize possible misalignment of successive scans.

Chapter 7

Conclusions

In this study, for the first time, porosity and the separated displacement fields of the solid and fluid compartments of biphasic tissues were measured in phantoms and *in vivo* human brain using a novel imaging technique and postprocessing pipeline.

IR-MRI combined with the biphasic T_1 relaxation model allowed us to quantify CSF porosity of brain tissue based on a simplification of highly complex fluid-solid structures. Our approach was validated in tissue-mimicking biphasic phantoms using microscopy and fluid drainage.

The combination of IR-MRI and IR-MRE allowed us to separately measure the solid and fluid strain fields. This new approach allowed us to quantify ρ_{12}, which was negative both in phantoms and in the human brain, as predicted by poroelastic theory.

Beyond poroelastography, IR-MRE can also be used to improve the characterization of mechanical properties of interfaces using viscoelastic model-based inversion. This was demonstrated in the brain, where signal from pure CSF areas was nulled, reducing blurring and biased stiffness in CSF-adjacent areas without affecting parenchymal SWS-based stiffness, again consistent with poroelastic theory.

The IR-MRE technique is currently being optimized to minimize MT and reduce long acquisition times. Furthermore, tissue-specific mathematical analysis is being developed to reduce the number of required IR-MRI TI times for further reduction of scan time. An optimized IR-MRE technique will open new horizons as a biomedical imaging marker sensitive to solid-fluid interactions and multiscale mechanical properties in biphasic media.

Other investigations have modeled soft tissues such as the brain as poroelastic media, and our study adds quantitative information, such as porosity and solid-fluid displacement fields.

Ongoing investigations of ex vivo and *in vivo* liver tissue modeled as a poroelastic material and compression wave analysis underscore the relevance of the novel IR-MRE technique.

Bibliography

[1] Ledia Lilaj, Thomas Fischer, Jing Guo, Jürgen Braun, Ingolf Sack, and Sebastian Hirsch. Separation of fluid and solid shear wave fields and quantification of coupling density by magnetic resonance poroelastography. *Magnetic Resonance in Medicine*, 85 (3):1655–1668, 2021.

[2] Sebastian Hirsch, Jurgen Braun, and Ingolf Sack. *Magnetic resonance elastography: physical background and medical applications*. John Wiley & Sons, 2017.

[3] Jeffrey Bamber, David Cosgrove, Christoph F Dietrich, Jérémie Fromageau, Jörg Bojunga, Fabrizio Calliada, V Cantisani, J-M Correas, M D'onofrio, EE Drakonaki, et al. Efsumb guidelines and recommendations on the clinical use of ultrasound elastography. part 1: Basic principles and technology. *Ultraschall in der Medizin-European Journal of Ultrasound*, 34(02):169–184, 2013.

[4] D Cosgrove, F Piscaglia, J Bamber, J Bojunga, J-M Correas, OH Gilja, AS Klauser, I Sporea, F Calliada, V Cantisani, et al. Efsumb guidelines and recommendations on the clinical use of ultrasound elastography. part 2: Clinical applications. *Ultraschall in der Medizin-European Journal of Ultrasound*, 34(03):238–253, 2013.

[5] Thomas Deffieux, Charlie Demene, Mathieu Pernot, and Mickael Tanter. Functional ultrasound neuroimaging: a review of the preclinical and clinical state of the art. *Current opinion in neurobiology*, 50:128–135, 2018.

[6] Y Su, J Ma, L Du, J Xia, Y Wu, X Jia, Y Cai, Y Li, J Zhao, and Q Liu. Application of acoustic radiation force impulse imaging (arfi) in quantitative evaluation of neonatal brain development. *Clin Exp Obstet Gynecol*, 42(6):797–800, 2015.

[7] D Chauvet, M Imbault, L Capelle, C Demene, M Mossad, C Karachi, AL Boch, JL Gen-

nisson, and M Tanter. In vivo measurement of brain tumor elasticity using intraoperative shear wave elastography. *Ultraschall Med*, 37(6):584–590, 2016.

[8] Michael Ertl, Nele Raasch, Gertrud Hammel, Katharina Harter, and Christopher Lang. Transtemporal investigation of brain parenchyma elasticity using 2-d shear wave elastography: definition of age-matched normal values. *Ultrasound in medicine & biology*, 44(1):78–84, 2018.

[9] Heiko Tzschätzsch, Bernhard Kreft, Felix Schrank, Judith Bergs, Jürgen Braun, and Ingolf Sack. In vivo time-harmonic ultrasound elastography of the human brain detects acute cerebral stiffness changes induced by intracranial pressure variations. *Scientific reports*, 8(1):1–9, 2018.

[10] Bernhard Kreft, Judith Bergs, Mehrgan Shahryari, Leon Alexander Danyel, Stefan Hetzer, Jürgen Braun, Ingolf Sack, and Heiko Tzschätzsch. Cerebral ultrasound time-harmonic elastography reveals softening of the human brain due to dehydration. *Frontiers in Physiology*, 11:1754, 2021.

[11] R Muthupillai, DJ Lomas, PJ Rossman, James F Greenleaf, Armando Manduca, and Richard Lorne Ehman. Magnetic resonance elastography by direct visualization of propagating acoustic strain waves. *Science*, 269(5232):1854–1857, 1995.

[12] Jing Guo, Sebastian Hirsch, Andreas Fehlner, Sebastian Papazoglou, Michael Scheel, Juergen Braun, and Ingolf Sack. Towards an elastographic atlas of brain anatomy. *PloS one*, 8(8):e71807, 2013.

[13] Ingolf Sack, Bernd Beierbach, Jens Wuerfel, Dieter Klatt, Uwe Hamhaber, Sebastian Papazoglou, Peter Martus, and Jürgen Braun. The impact of aging and gender on brain viscoelasticity. *Neuroimage*, 46(3):652–657, 2009.

[14] Ingolf Sack, Kaspar-Josche Streitberger, Dagmar Krefting, Friedemann Paul, and Jürgen Braun. The influence of physiological aging and atrophy on brain viscoelastic properties in humans. *PloS one*, 6(9):e23451, 2011.

[15] Arvin Arani, Matthew C Murphy, Kevin J Glaser, Armando Manduca, David S Lake, Scott A Kruse, Clifford R Jack Jr, Richard L Ehman, and John Huston 3rd. Measuring

the effects of aging and sex on regional brain stiffness with mr elastography in healthy older adults. *Neuroimage*, 111:59–64, 2015.

[16] Lucy V Hiscox, Curtis L Johnson, Matthew DJ McGarry, Michael Perrins, Aimee Littlejohn, Edwin JR van Beek, Neil Roberts, and John M Starr. High-resolution magnetic resonance elastography reveals differences in subcortical gray matter viscoelasticity between young and healthy older adults. *Neurobiology of aging*, 65:158–167, 2018.

[17] Kaspar-Josche Streitberger, Edzard Wiener, Jan Hoffmann, Florian Baptist Freimann, Dieter Klatt, Jürgen Braun, Kui Lin, Joyce McLaughlin, Christian Sprung, Randolf Klingebiel, et al. In vivo viscoelastic properties of the brain in normal pressure hydrocephalus. *NMR in Biomedicine*, 24(4):385–392, 2011.

[18] Avital Perry, Christopher S Graffeo, Nikoo Fattahi, Mona M ElSheikh, Nealey Cray, Arvin Arani, Richard L Ehman, Kevin J Glaser, Armando Manduca, Fredric B Meyer, et al. Clinical correlation of abnormal findings on magnetic resonance elastography in idiopathic normal pressure hydrocephalus. *World neurosurgery*, 99:695–700, 2017.

[19] Jens Wuerfel, Friedemann Paul, Bernd Beierbach, Uwe Hamhaber, Dieter Klatt, Sebastian Papazoglou, Frauke Zipp, Peter Martus, Jürgen Braun, and Ingolf Sack. Mr-elastography reveals degradation of tissue integrity in multiple sclerosis. *Neuroimage*, 49(3):2520–2525, 2010.

[20] Andreas Fehlner, Janina Ruth Behrens, Kaspar-Josche Streitberger, Sebastian Papazoglou, Jürgen Braun, Judith Bellmann-Strobl, Klemens Ruprecht, Friedemann Paul, Jens Würfel, and Ingolf Sack. Higher-resolution mr elastography reveals early mechanical signatures of neuroinflammation in patients with clinically isolated syndrome. *Journal of Magnetic Resonance Imaging*, 44(1):51–58, 2016.

[21] Matthew C Murphy, David T Jones, Clifford R Jack Jr, Kevin J Glaser, Matthew L Senjem, Armando Manduca, Joel P Felmlee, Rickey E Carter, Richard L Ehman, and John Huston III. Regional brain stiffness changes across the alzheimer's disease spectrum. *NeuroImage: Clinical*, 10:283–290, 2016.

[22] Lea M Gerischer, Andreas Fehlner, Theresa Köbe, Kristin Prehn, Daria Antonenko, Ulrike Grittner, Jürgen Braun, Ingolf Sack, and Agnes Flöel. Combining viscoelasticity,

diffusivity and volume of the hippocampus for the diagnosis of alzheimer's disease based on magnetic resonance imaging. *NeuroImage: Clinical*, 18:485–493, 2018.

[23] Axel Lipp, Cornelia Skowronek, Andreas Fehlner, Kaspar-Josche Streitberger, Jürgen Braun, and Ingolf Sack. Progressive supranuclear palsy and idiopathic parkinson's disease are associated with local reduction of in vivo brain viscoelasticity. *European radiology*, 28(8):3347–3354, 2018.

[24] Axel Lipp, Radmila Trbojevic, Friedemann Paul, Andreas Fehlner, Sebastian Hirsch, Michael Scheel, Cornelia Noack, Jürgen Braun, and Ingolf Sack. Cerebral magnetic resonance elastography in supranuclear palsy and idiopathic parkinson's disease. *NeuroImage: Clinical*, 3:381–387, 2013.

[25] John Huston III, Matthew C Murphy, Bradley F Boeve, Nikoo Fattahi, Arvin Arani, Kevin J Glaser, Armando Manduca, David T Jones, and Richard L Ehman. Magnetic resonance elastography of frontotemporal dementia. *Journal of Magnetic Resonance Imaging*, 43(2):474–478, 2016.

[26] Mona ElSheikh, Arvin Arani, Avital Perry, Bradley F Boeve, Fredric B Meyer, Rodolfo Savica, Richard L Ehman, and John Huston III. Mr elastography demonstrates unique regional brain stiffness patterns in dementias. *American Journal of Roentgenology*, 209 (2):403–408, 2017.

[27] Giulia Franceschini, Davide Bigoni, Peter Regitnig, and Gerhard A Holzapfel. Brain tissue deforms similarly to filled elastomers and follows consolidation theory. *Journal of the Mechanics and Physics of Solids*, 54(12):2592–2620, 2006.

[28] MDJ McGarry, CL Johnson, BP Sutton, JG Georgiadis, EEW Van Houten, AJ Pattison, JB Weaver, and KD Paulsen. Suitability of poroelastic and viscoelastic mechanical models for high and low frequency mr elastography. *Medical physics*, 42(2):947–957, 2015.

[29] CG Armstrong, WM Lai, and VC Mow. An analysis of the unconfined compression of articular cartilage. *Journal of biomechanical engineering*, 106(2):165–173, 1984.

[30] Raffaella Righetti, Brian S Garra, Louise M Mobbs, Christina M Kraemer-Chant, Jonathan Ophir, and Thomas A Krouskop. The feasibility of using poroelastographic

techniques for distinguishing between normal and lymphedematous tissues in vivo. *Physics in Medicine & Biology*, 52(21):6525, 2007.

[31] Maurice A Biot. General theory of three-dimensional consolidation. *Journal of applied physics*, 12(2):155–164, 1941.

[32] Elisa E Konofagou, Timothy P Harrigan, Jonathan Ophir, and Thomas A Krouskop. Poroelastography: Imaging the poroelastic properties of tissues. *Ultrasound in medicine & biology*, 27(10):1387–1397, 2001.

[33] Gearóid P Berry, Jeffrey C Bamber, Cecil G Armstrong, Naomi R Miller, and Paul E Barbone. Towards an acoustic model-based poroelastic imaging method: I. theoretical foundation. *Ultrasound in medicine & biology*, 32(4):547–567, 2006.

[34] Ricardo Leiderman, Paul E Barbone, Assad A Oberai, and Jeffrey C Bamber. Coupling between elastic strain and interstitial fluid flow: ramifications for poroelastic imaging. *Physics in Medicine & Biology*, 51(24):6291, 2006.

[35] Phillip R Perriñez, Francis E Kennedy, Elijah EW Van Houten, John B Weaver, and Keith D Paulsen. Magnetic resonance poroelastography: an algorithm for estimating the mechanical properties of fluid-saturated soft tissues. *IEEE transactions on medical imaging*, 29(3):746–755, 2010.

[36] Phillip R Perriñez, Adam J Pattison, Francis E Kennedy, John B Weaver, and Keith D Paulsen. Contrast detection in fluid-saturated media with magnetic resonance poroelastography. *Medical physics*, 37(7Part1):3518–3526, 2010.

[37] Phillip R Perriñez, Francis E Kennedy, Elijah EW Van Houten, John B Weaver, and Keith D Paulsen. Modeling of soft poroelastic tissue in time-harmonic mr elastography. *IEEE transactions on biomedical engineering*, 56(3):598–608, 2008.

[38] Matthew McGarry, Elijah Van Houten, Ligin Solamen, Scott Gordon-Wylie, John Weaver, and Keith Paulsen. Uniqueness of poroelastic and viscoelastic nonlinear inversion mr elastography at low frequencies. *Physics in Medicine & Biology*, 64(7): 075006, 2019.

[39] Ingolf Sack and Tobias Schaeffter. *Quantification of biophysical parameters in medical imaging*. Springer, 2018.

[40] Tatsuya Nagashima, Norihiko Tamaki, Satoshi Matsumoto, Barry Horwitz, and Yasuyuki Seguchi. Biomechanics of hydrocephalus: a new theoretical model. *Neurosurgery*, 21(6):898–904, 1987.

[41] Eva Syková and Charles Nicholson. Diffusion in brain extracellular space. *Physiological reviews*, 88(4):1277–1340, 2008.

[42] GL Belen'kiĭ, E Yu Salaev, and RA Suleĭmanov. Deformation effects in layer crystals. *Soviet Physics Uspekhi*, 31(5):434, 1988.

[43] Félix Mouhat and François-Xavier Coudert. Necessary and sufficient elastic stability conditions in various crystal systems. *Physical review B*, 90(22):224104, 2014.

[44] Kaspar-Josche Streitberger, Ledia Lilaj, Felix Schrank, Jürgen Braun, Karl-Titus Hoffmann, Martin Reiss-Zimmermann, Josef A Käs, and Ingolf Sack. How tissue fluidity influences brain tumor progression. *Proceedings of the National Academy of Sciences*, 117(1):128–134, 2020.

[45] Maurice A Biot. Theory of propagation of elastic waves in a fluid-saturated porous solid. ii. higher frequency range. *The Journal of the acoustical Society of america*, 28 (2):179–191, 1956.

[46] Victor Ilisie. *Lectures in Classical Mechanics*. Springer, 2020.

[47] Yogesh K Mariappan, Kevin J Glaser, and Richard L Ehman. Magnetic resonance elastography: a review. *Clinical anatomy*, 23(5):497–511, 2010.

[48] Thomas L Chenevert, Andrei R Skovoroda, Matthew O donnell, and Stanislav Y Emelianov. Elasticity reconstructive imaging by means of stimulated echo mri. *Magnetic resonance in medicine*, 39(3):482–490, 1998.

[49] Derek D Steele, Thomas L Chenevert, Andrei R Skovoroda, and Stanislav Y Emelianov. Three-dimensional static displacement, stimulated echo nmr elasticity imaging. *Physics in Medicine & Biology*, 45(6):1633, 2000.

[50] Tadafumi Kawamoto. Use of a new adhesive film for the preparation of multi-purpose fresh-frozen sections from hard tissues, whole-animals, insects and plants. *Archives of histology and cytology*, 66(2):123–143, 2003.

[51] John Ashburner and Karl J Friston. Unified segmentation. *Neuroimage*, 26(3):839–851, 2005.

[52] Raffaella Righetti, Jonathan Ophir, and Thomas A Krouskop. A method for generating permeability elastograms and poisson's ratio time-constant elastograms. *Ultrasound in medicine & biology*, 31(6):803–816, 2005.

[53] Steven D Wolff and Robert S Balaban. Magnetization transfer contrast (mtc) and tissue water proton relaxation in vivo. *Magnetic resonance in medicine*, 10(1):135–144, 1989.

[54] W Thomas Dixon, Hans Engels, Mauricio Castillo, and Maziar Sardashti. Incidental magnetization transfer contrast in standard multislice imaging. *Magnetic resonance imaging*, 8(4):417–422, 1990.

[55] Kurt E Schlageter, Peter Molnar, Gregory D Lapin, and Dennis R Groothuis. Microvessel organization and structure in experimental brain tumors: microvessel populations with distinctive structural and functional properties. *Microvascular research*, 58(3): 312–328, 1999.

[56] Jörg Polzehl and Karsten Tabelow. *Magnetic Resonance Brain Imaging*. Springer, 2019.

[57] Andrew N Norris. Radiation from a point source and scattering theory in a fluid-saturated porous solid. *The Journal of the Acoustical Society of America*, 77(6):2012–2023, 1985.

[58] Sebastian Hirsch, Dieter Klatt, Florian Freimann, Michael Scheel, Jürgen Braun, and Ingolf Sack. In vivo measurement of volumetric strain in the human brain induced by arterial pulsation and harmonic waves. *Magnetic resonance in medicine*, 70(3):671–683, 2013.

[59] Likun Tan, Matthew DJ McGarry, Elijah EW Van Houten, Ming Ji, Ligin Solamen, Wei Zeng, John B Weaver, and Keith D Paulsen. A numerical framework for interstitial fluid pressure imaging in poroelastic mre. *Plos one*, 12(6):e0178521, 2017.

[60] Eric Barnhill, Mila Nikolova, Cemre Ariyurek, Florian Dittmann, Jürgen Braun, and Ingolf Sack. Fast robust dejitter and interslice discontinuity removal in mri phase acquisitions: Application to magnetic resonance elastography. *IEEE transactions on medical imaging*, 38(7):1578–1587, 2019.

[61] Mariusz Kaczmarek, Ravi P Subramaniam, and Samuel R Neff. The hydromechanics of hydrocephalus: steady-state solutions for cylindrical geometry. *Bulletin of mathematical biology*, 59(2):295–323, 1997.

[62] David N Levine. The pathogenesis of normal pressure hydrocephalus: a theoretical analysis. *Bulletin of mathematical biology*, 61(5):875–916, 1999.

[63] Richard D Penn and Andreas Linninger. The physics of hydrocephalus. *Pediatric neurosurgery*, 45(3):161–174, 2009.

[64] Brett Tully and Yiannis Ventikos. Coupling poroelasticity and cfd for cerebrospinal fluid hydrodynamics. *IEEE Transactions on biomedical engineering*, 56(6):1644–1651, 2009.

[65] Xuan Zhang, Joshua E Medow, Bermans J Iskandar, Fa Wang, Mehdi Shokoueinejad, Joyce Koueik, and John G Webster. Invasive and noninvasive means of measuring intracranial pressure: a review. *Physiological measurement*, 38(8):R143, 2017.

[66] Andrea Bonfiglio, Kritsada Leungchavaphongse, Rodolfo Repetto, and Jennifer H Siggers. Mathematical modeling of the circulation in the liver lobule. *Journal of biomechanical engineering*, 132(11), 2010.

[67] Ledia Lilaj, Helge Herthum, Tom Meyer, Mehrgan Shahryari, Gergely Bertalan, Alfonso Caiazzo, Jürgen Braun, Thom Fischer, Sebastian Hirsch, and Ingolf Sack. Cerebral inversion recovery mr elastography for cortical stiffness quantification.

[68] Sean CL Deoni and Shannon H Kolind. Investigating the stability of mcdespot myelin water fraction values derived using a stochastic region contraction approach. *Magnetic resonance in medicine*, 73(1):161–169, 2015.

[69] Andreas Fehlner, Sebastian Hirsch, Martin Weygandt, Thomas Christophel, Eric Barnhill, Mykola Kadobianskyi, Jürgen Braun, Johannes Bernarding, Ralf Lützkendorf, Ingolf Sack, et al. Increasing the spatial resolution and sensitivity of magnetic resonance elastography by correcting for subject motion and susceptibility-induced image distortions. *Journal of Magnetic Resonance Imaging*, 46(1):134–141, 2017.

Statutory Declaration

“I, Ledia, Lilaj, by personally signing this document in lieu of an oath, hereby affirm that I prepared the submitted dissertation on the topic Quantification of porosity, separated fluid-solid shear wave fields and coupling density with inversion recovery magnetic resonance elastography in porous phantoms and in vivo brain/ Quantifizierung von Porosität, getrennten Scherwellenfelder der festen und flüssigen Phasen sowie Kopplungsdichte mittels Inversion-Recovery-Magnetresonanzelastographie in porösen Phantomen und In-vivo-Gehirnen, independently and without the support of third parties, and that I used no other sources and aids than those stated.
All parts which are based on the publications or presentations of other authors, either in letter or in spirit, are specified as such in accordance with the citing guidelines. The sections on methodology (in particular regarding practical work, laboratory regulations, statistical processing) and results (in particular regarding figures, charts and tables) are exclusively my responsibility.

Furthermore, I declare that I have correctly marked all of the data, the analyses, and the conclusions generated from data obtained in collaboration with other persons, and that I have correctly marked my own contribution and the contributions of other persons (cf. declaration of contribution). I have correctly marked all texts or parts of texts that were generated in collaboration with other persons.

My contributions to any publications to this dissertation correspond to those stated in the below joint declaration made together with the supervisor. All publications created within the scope of the dissertation comply with the guidelines of the ICMJE (International Committee of Medical Journal Editors; www.icmje.org) on authorship. In addition, I declare that I shall comply with the regulations of Charité – Universitätsmedizin Berlin on ensuring good scientific practice.

I declare that I have not yet submitted this dissertation in identical or similar form to another Faculty.

The significance of this statutory declaration and the consequences of a false statutory declaration under criminal law (Sections 156, 161 of the German Criminal Code) are known to me.”

Date Signature

Declaration of your own contribution to the top-journal publication for a Ph.D. or MD/Ph.D. degree

Ledia Lilaj contributed the following to the below listed publication:

Publication 1: Ledia Lilaj, Thomas Fischer, Jing Guo, Jürgen Braun, Ingolf Sack, Sebastian Hirsch. Separation of fluid and solid shear wave fields and quantification of coupling density by magnetic resonance poroelastography, Magnetic Resonance in Medicine, 2020

Contribution:

For the first time, the publication demonstrated the feasibility of the porosity, separated fluid/solid shear waves speed, and coupling density in phantoms and in vivo human brain using inversion recovery-magnetic resonance imaging (IR-MRI) and inversion recovery-magnetic resonance elastography (IR-MRE) and introduced the method to the MRE community.
Prof. Sack and Dr. Hirsch conceived the initial idea of my project described to me during my selection project. Dr. Hirsch developed the initial theoretical background described in previously published books. Dr. Hirsch, Prof Sack and I further developed the initial idea and the theory that allowed to estimate, for the first time, the separated shear fields and the coupling density.
Dr. Hirsh developed the IR-MRI/IR-MRE sequence, and I tested and contributed significantly to its implementation.
I created the phantoms production protocols and produced them (fluid-fluid and various types of tofu phantoms). Prof. Braun built the tools necessary for the tofu phantoms production.
I developed a specific histological protocol for obtaining the microscopy slides of the very fragile tofu tissue without breaking its porous structure. I produced the slides, performed the measurement and data analysis. Dr. Radbruch and Dr. de Schellenberger provided me guidance in the field of histology and microscopy.
I performed the measurements and estimations of the extracted fluid via draining by extrapolating the drainage rate.
Dr. Hirsch and I developed the scanning protocols of the phantoms and in vivo studies. I recruited the IR-MRI and IR-MRE study volunteers, organized and performed the phantom and in vivo scans in three different MR scanners.
With the supervision of Prof. Sack and Dr. Hirsch, I designed the postprocessing pipeline of all the experiments and performed the statistical analysis of the results. I completed a more detailed study of the in vivo data to investigate porosity, T1 of the solid compartment, and coupling density distribution in different brain areas. All the analyses were performed on Matlab.
Together with Prof. Sack and Dr. Hirsch, I wrote and edited the manuscript. All findings presented in the publication result from my data analysis and statistical tests. Each figure and table shown was created by me and is based on my research.
All co-authors provided valuable feedback on the experiments and interpreted the results.

_____
Signature, date and stamp of first supervising university professor/lecturer

_____
Signature of doctoral candidate

Journal Data Filtered By: **Selected JCR Year: 2018** Selected Editions: SCIE,SSCI Selected Categories: **"RADIOLOGY, NUCLEAR MEDICINE and MEDICAL IMAGING"** Selected Category Scheme: WoS

Gesamtanzahl: 129 Journale

Rank	Full Journal Title	Total Cites	Journal Impact Factor	Eigenfactor Score
1	JACC-Cardiovascular Imaging	8,801	10.975	0.026160
2	MEDICAL IMAGE ANALYSIS	7,694	8.880	0.013370
3	IEEE TRANSACTIONS ON MEDICAL IMAGING	19,545	7.816	0.024990
4	RADIOLOGY	54,641	7.608	0.061300
5	JOURNAL OF NUCLEAR MEDICINE	27,551	7.354	0.037990
6	EUROPEAN JOURNAL OF NUCLEAR MEDICINE AND MOLECULAR IMAGING	15,406	7.182	0.024760
7	CLINICAL NUCLEAR MEDICINE	4,922	6.498	0.007680
8	INTERNATIONAL JOURNAL OF RADIATION ONCOLOGY BIOLOGY PHYSICS	45,833	6.203	0.046810
9	INVESTIGATIVE RADIOLOGY	6,563	6.091	0.011150
10	Circulation-Cardiovascular Imaging	5,456	5.813	0.018480
11	NEUROIMAGE	99,720	5.812	0.132720
12	ULTRASOUND IN OBSTETRICS & GYNECOLOGY	12,336	5.595	0.020140
13	European Heart Journal-Cardiovascular Imaging	5,498	5.260	0.021650
14	RADIOTHERAPY AND ONCOLOGY	17,873	5.252	0.027470
15	Photoacoustics	512	5.250	0.001330
16	JOURNAL OF CARDIOVASCULAR MAGNETIC RESONANCE	5,113	5.070	0.014020
17	ULTRASCHALL IN DER MEDIZIN	2,238	4.613	0.003700
18	HUMAN BRAIN MAPPING	22,040	4.554	0.043230
19	JOURNAL OF NUCLEAR CARDIOLOGY	3,711	4.112	0.004480
20	EUROPEAN RADIOLOGY	19,597	3.962	0.033870

Rank	Full Journal Title	Total Cites	Journal Impact Factor	Eigenfactor Score
21	RADIOGRAPHICS	11,768	3.923	0.009170
22	Biomedical Optics Express	9,547	3.910	0.021750
23	MAGNETIC RESONANCE IN MEDICINE	32,648	3.858	0.034990
24	SEMINARS IN NUCLEAR MEDICINE	2,245	3.798	0.002710
25	Journal of the American College of Radiology	4,191	3.785	0.009760
26	JOURNAL OF MAGNETIC RESONANCE IMAGING	17,147	3.732	0.027800
27	KOREAN JOURNAL OF RADIOLOGY	2,687	3.730	0.004800
28	INTERNATIONAL JOURNAL OF HYPERTHERMIA	3,552	3.589	0.004020
29	EJNMMI Physics	394	3.475	0.001350
30	NMR IN BIOMEDICINE	7,511	3.414	0.014790
31	MOLECULAR IMAGING AND BIOLOGY	2,543	3.341	0.005360
32	Journal of Cardiovascular Computed Tomography	1,711	3.316	0.004430
33	COMPUTERIZED MEDICAL IMAGING AND GRAPHICS	2,464	3.298	0.002990
34	AMERICAN JOURNAL OF NEURORADIOLOGY	23,231	3.256	0.028010
35	MEDICAL PHYSICS	26,715	3.177	0.030870
36	AMERICAN JOURNAL OF ROENTGENOLOGY	33,633	3.161	0.028540
37	CANCER IMAGING	1,406	3.153	0.002220
38	Quantitative Imaging in Medicine and Surgery	1,072	3.074	0.002420
39	PHYSICS IN MEDICINE AND BIOLOGY	27,458	3.030	0.031970
40	EJNMMI Research	1,408	3.000	0.004320
41	EUROPEAN JOURNAL OF RADIOLOGY	12,871	2.948	0.019480
42	Radiation Oncology	5,669	2.895	0.012980

Selected JCR Year: 2018; Selected Categories: “RADIOLOGY, NUCLEAR MEDICINE and MEDICAL IMAGING”

Received: 6 February 2020 | Revised: 14 August 2020 | Accepted: 14 August 2020

DOI: 10.1002/mrm.28507

FULL PAPER

Magnetic Resonance in Medicine

Separation of fluid and solid shear wave fields and quantification of coupling density by magnetic resonance poroelastography

Ledia Lilaj[1] | **Thomas Fischer**[2] | **Jing Guo**[1] | **Jürgen Braun**[3] | **Ingolf Sack**[1] | **Sebastian Hirsch**[4,5]

[1]Department of Radiology, Charité – Universitätsmedizin Berlin, Berlin, Germany

[2]Department of Radiology, Interdisciplinary Ultrasound Center, Charité – Universitätsmedizin Berlin, Berlin, Germany

[3]Institute of Medical Informatics, Charité – Universitätsmedizin Berlin, Berlin, Germany

[4]Berlin Center for Advanced Neuroimaging, Charité – Universitätsmedizin Berlin, Berlin, Germany

[5]Bernstein Center for Computational Neuroscience, Berlin, Germany

Correspondence
Sebastian Hirsch, Berlin Center for Advanced Neuroimaging, Charité – Universitätsmedizin Berlin, Charitéplatz 1, Berlin 10117, Germany.
Email: sebastian.hirsch@charite.de

Funding information
Deutsche Forschungsgemeinschaft, Grant/Award Number: BIOQIC GRK2260, and Matrix in Vision SFB1340

Purpose: Biological soft tissues often have a porous architecture comprising fluid and solid compartments. Upon displacement through physiological or externally induced motion, the relative motion of these compartments depends on poroelastic parameters, such as coupling density (ρ_{12}) and tissue porosity. This study introduces inversion recovery MR elastography (IR-MRE) (1) to quantify porosity defined as fluid volume over total volume, (2) to separate externally induced shear strain fields of fluid and solid compartments, and (3) to quantify coupling density assuming a biphasic behavior of in vivo brain tissue.

Theory and Methods: Porosity was measured in eight tofu phantoms and gray matter (GM) and white matter (WM) of 21 healthy volunteers. Porosity of tofu was compared to values obtained by fluid draining and microscopy. Solid and fluid shear-strain amplitudes and ρ_{12} were estimated both in phantoms and in in vivo brain.

Results: T_1-based measurement of tofu porosity agreed well with reference values ($R = 0.99$, $P < .01$). Brain tissue porosity was 0.14 ± 0.02 in GM and 0.05 ± 0.01 in WM ($P < .001$). Fluid shear strain was found to be phase-locked with solid shear strain but had lower amplitudes in both tofu phantoms and brain tissue ($P < .05$). In accordance with theory, tofu and brain ρ_{12} were negative.

Conclusion: IR-MRE allowed for the first time separation of shear strain fields of solid and fluid compartments for measuring coupling density according to the biphasic theory of poroelasticity. Thus, IR-MRE opens horizons for poroelastography-derived imaging markers that can be used in basic research and diagnostic applications.

KEYWORDS
brain tissue, coupling density, elastography, inversion recovery, phantom, porosity

1 | INTRODUCTION

MR elastography (MRE) is a noninvasive imaging technique that allows in vivo quantification of the viscoelastic properties of biological soft tissues.[1] In MRE, tissues are usually modeled as monophasic viscoelastic media. However, it has been demonstrated that the mechanical behavior of several tissues, such as brain,[2,3] cartilage,[4,5] or edematous tissue,[6] is better described by a poroelastic model comprising a solid matrix saturated with an incompressible fluid.[7] The solid matrix consists of cells and the extracellular matrix, while the fluid compartment includes interstitial fluid, blood, or cerebrospinal fluid (CSF). The more complex nature of the poroelastic model compared to the monophasic viscoelastic model, including interactions between the compartments, and coupling of motion fields, requires specialized acquisition and postprocessing strategies to exploit the advantages provided by the poroelastic model. To account for the number of unknown model parameters in the poroelastic equations of motion, previous studies have used a priori assumptions about tissue structure.[8] In particular, porosity has never been quantified noninvasively in in vivo brain tissue before. Instead, a global value of, for example, 0.20 for the entire brain, has been assumed.[4,8] In this study, we propose a technique to quantify porosity along with other poroelastic model parameters from a series of measurements. Our motivation is twofold: using spatially resolved maps of the porosity is expected to provide more accurate estimates for the poroelastic parameters than using a global value; and porosity might present itself as a meaningful biomarker to be explored in future studies. While previous applications of poro-MRE have mainly focused on investigating the compression properties of biological tissues,[9,10] in this work, we will concentrate on shear waves since they provide higher SNR than compression waves. The Biot model for poroelastic wave propagation predicts 1 shear wave mode as opposed to 2 compression wave modes.[11]

Our proposed method for poroelastic MRE consists of 4 steps: (1) acquisition of a relaxation curve using inversion recovery (IR-MRI); (2) estimation of porosity and signal parameters of the 2 compartments using a biphasic, biexponential relaxation model; (3) acquisition of MRE data with added IR at two different inversion times (TIs) (IR-MRE); (4) separation of the solid and fluid shear wave fields based on a biphasic MRE signal model.

The general feasibility of this method will be demonstrated using tissue-mimicking phantoms made of coagulated soybean curd (tofu), whose microstructure is characterized by abundant fluid-filled pores.[12] Separating the shear wave fields corresponding to fluid and solid tissue motion will allow us to estimate a new parameter in poroelasticity imaging, namely *coupling density*, ρ_{12}. This parameter is associated with the transfer of kinetic energy between the 2 compartments and is predicted to be negative due to the inability of the fluid to support shear waves.[13]

As an outlook, we will quantify in vivo tissue porosity of the brain considering brain tissue as a porous medium permeated by an extracellular fluid[14] with T_1 relaxation properties similar to CSF.[15] From fluid and solid tissue motions, we will finally quantify ρ_{12} of the the in vivo human brain.

2 | THEORY

Longitudinal relaxation time, T_1, can be mapped using an IR sequence with different TIs and fitting the signal intensity of each voxel with a monoexponential relaxation curve

$$I(TI) = I_\infty \cdot \left(1 - 2 \cdot e^{-\frac{TI}{T_1}}\right) + C. \quad (1)$$

$I(TI)$ is the voxel intensity measured in the image with inversion time TI. I_∞ is the intensity without inversion. C is the noise offset, which is typically two orders of magnitude smaller than I. Since we ensured that $TR > 5 \cdot T_1$ in all measurements, we assumed that each scan was performed with fully relaxed longitudinal magnetization and, therefore, neglected TR-dependent terms in Equation (1).

Most tissue types are not entirely homogeneous across a voxel; they rather have a complex multiphasic structure. In this work, we assume a porous biphasic medium, consisting of a porous solid matrix and a liquid saturating the pore space, with different T_1 constants. The solid compartment is composed of macromolecules and cells, whereas the fluid compartment comprises moving fluids, such as blood, CSF, or interstitial fluid.

2.1 | Porosity estimation by IR-MRI

Porosity f of a porous medium is defined as the volume fraction of the medium that is occupied by the fluid compartment:

$$f = \frac{V^f}{V} \quad (2)$$

where V is a volume element of the medium, and V^f is the enclosed fluid volume. The IR-MRI signal of a biphasic medium is a superposition of the contribution of the 2 compartments, each weighted by its volume fraction: f for the fluid and (1-f) for the solid.

To account for biphasic T_1 signal relaxation, signal intensity is expressed as a function of *TI:*

$$I^m(TI) = I^f \cdot f\left(1-2e^{-\frac{TI}{T_1^f}}\right) + I^s \cdot (1-f)\left(1-2e^{-\frac{TI}{T_1^s}}\right) + C. \quad (3)$$

The superscript m on the left-hand side indicates that this is the measured signal intensity, as opposed to I^s and I^f (the hypothetical signal intensities of the pure solid and fluid material), which can only be quantified indirectly. I^s and I^f also account for the signal intensity dependence on T_2/T_2^* and TE, which are not relevant for this work. In order to estimate porosity, Equation (3) is fitted to a series of IR-MRI scans acquired with different TIs. However, the number of unknown parameters (I^f, I^s, T_1^f, T_1^s, f, C) renders this fitting process unstable. Therefore, we will assess the fluid properties, I^f and T_1^f, in an independent estimation, assuming that their variability across the biphasic object is negligible, thus reducing the unknown parameters to the set (I^s, T_1^s, f, C).

To further simplify the fitting procedure, we focus on the specific case of a scan without inversion pulse (formally, this is identical to $TI \to \infty$, but we will drop the TI dependence in the following formulas)

$$I^{m,\infty} = I^f \cdot f + I^s \cdot (1-f) + C. \quad (4)$$

Since offset C in Equation (4) is typically 2 orders of magnitude lower than I^f and $I^{m,\infty}$, it will be neglected henceforth, improving fitting stability at the expense of precision.

Solving Equation (4) for I^s and substituting into Equation (3) yields the following simplified equation:

$$I^m(TI) = -2 \cdot f \cdot I^f e^{-\frac{TI}{T_1^f}} - 2\left(I^{m,\infty} - f \cdot I^f\right) \cdot e^{-\frac{TI}{T_1^s}} + C. \quad (5)$$

With I^s thusly eliminated as an unknown parameter, the set of fitting parameters is further reduced to f, T_1^s, and offset C.

The IR-MRE signal equation of a biphasic medium is an extension of Equation (3), which includes the motion-induced signal phase:

$$M^m \cdot e^{i\varphi^m} = I^f \cdot f\left(1-2e^{-\frac{TI}{T_1^f}}\right) \cdot e^{i\varphi^f} + I^s(1-f)\left(1-2e^{-\frac{TI}{T_1^s}}\right) \cdot e^{i\varphi^s}. \quad (6)$$

M^m and φ^m represent the magnitude and phase of the measured MRE signal. Equation (6) can be used to decompose the measured compound displacement field, φ^m, into the compartmental fields φ^s and φ^f, if MRE is performed twice with different TIs, denoted TI_1 and TI_2. In the simplest case, we choose $TI_1 \to \infty$ (i.e., no inversion is performed) and $TI_2 = \ln(2) \cdot T_1^f$, that is, the TI that nulls the signal of the fluid. The system of the two versions of Equation (6) for 2 TIs can be solved for φ^s and φ^f

$$e^{i\varphi^s} = \frac{M^{m,2} \cdot e^{i\varphi^{m,2}}}{I^s \cdot (1-f)\left(1-2e^{-\frac{TI^{m,2}}{T_1^s}}\right)} \quad (7)$$

$$e^{i\varphi^f} = \frac{M^{m,1} \cdot e^{i\varphi^{m,1}} - \frac{M^{m,2} \cdot e^{i\varphi^{m,2}}}{\left(1-2e^{-\frac{TI^{m,2}}{T_1^s}}\right)}}{I^f \cdot f} \quad (8)$$

where indices 1 and 2 refer to measurements with TI_1 and TI_2. The displacements φ^s and φ^m can then be extracted by taking the complex phase of the two equations.

2.2 | Biphasic elastic motion

The poroelastic relationship between deformation (strain ε) and the resulting stresses (σ) can be expressed using Biot's law of stress and strain in a biphasic material.[7] We extended this equation to fulfill the condition of single-phase stresses if $f \to 0$ and $\to 1$, as proposed by Sack and Schaeffter[13]:

$$\begin{pmatrix} (1-f)\sigma_{11}^s \\ (1-f)\sigma_{22}^s \\ (1-f)\sigma_{33}^s \\ (1-f)\sigma_{12}^s \\ (1-f)\sigma_{23}^s \\ (1-f)\sigma_{13}^s \\ f\sigma^f \end{pmatrix} = (1-f) \begin{pmatrix} \left(K^s + \frac{4}{3}\mu^s\right) & \left(K^s - \frac{2}{3}\mu^s\right) & \left(K^s - \frac{2}{3}\mu^s\right) & 0 & 0 & 0 & fH \\ \left(K^s - \frac{2}{3}\mu^s\right) & \left(K^s + \frac{4}{3}\mu^s\right) & \left(K^s - \frac{2}{3}\mu^s\right) & 0 & 0 & 0 & fH \\ \left(K^s - \frac{2}{3}\mu^s\right) & \left(K^s - \frac{2}{3}\mu^s\right) & \left(K^s + \frac{4}{3}\mu^s\right) & 0 & 0 & 0 & fH \\ 0 & 0 & 0 & \mu^s & 0 & 0 & 0 \\ 0 & 0 & 0 & 0 & \mu^s & 0 & 0 \\ 0 & 0 & 0 & 0 & 0 & \mu^s & 0 \\ fH & fH & fH & 0 & 0 & 0 & \frac{f}{1-f}K^f \end{pmatrix} \cdot \begin{pmatrix} \varepsilon_{11}^s \\ \varepsilon_{22}^s \\ \varepsilon_{33}^s \\ 2\varepsilon_{12}^s \\ 2\varepsilon_{23}^s \\ 2\varepsilon_{13}^s \\ \varepsilon^f \end{pmatrix}. \quad (9)$$

The displacement of the fluid is expressed by scalar volumetric stress and strain, whereas the full 3D deformation field is required for the solid. K^s and μ^s are the bulk and shear modulus of the solid and K^f is the fluid bulk modulus. The coupling modulus H quantifies the stress induced in one compartment by deformation of the other compartment. Note that this approach, in contrast those by Mcgarry et al and Parker[3,16,17] does not account for additional stresses induced by hydrostatic pressure gradients, since we are only

interested in shear deformation and assume the corresponding model parameters to be pressure-independent. The equations of motion are derived from the balance of momentum,

$$\rho\ddot{\mathbf{u}} = \nabla \cdot \boldsymbol{\sigma} \tag{10}$$

with mass density ρ and displacement field $\mathbf{u}$. Applying the divergence operator to Equation (9), as prescribed by the right-hand side of Equation (10), and separating the resulting equations for solid and fluid motion yields

$$(1-f)\,\nabla \cdot \boldsymbol{\sigma}^s = (1-f)\left[\left(K^s + \frac{1}{3}\mu^s\right)\nabla(\nabla \cdot \mathbf{u}^s) + fH\nabla\varepsilon^f + \mu^s \Delta \mathbf{u}^s\right] \tag{11a}$$

$$f\nabla\sigma^f = f(1-f)H\nabla(\nabla \cdot \mathbf{u}^s) + fK^f\nabla\left(\nabla \cdot \mathbf{u}^f\right). \tag{11b}$$

These equations were derived under the assumption that all elastic properties vary slowly in space, allowing us to neglect their gradients.

Equations (11a and 11b) represent the motion of the full displacement vector field, comprising shear and volumetric deformation. However, from Equation (9), it is obvious that shear strain is decoupled from volumetric stress (and vice versa). Therefore, since elastography usually focuses on shear deformation, and since the shear waves have only one wave mode while the compression waves present two wave modes, we suppress compression waves by applying the curl operator:

$$\rho\nabla \times \ddot{\mathbf{u}} = \nabla \times \nabla \cdot \boldsymbol{\sigma}. \tag{12}$$

For the acceleration terms on the left-hand side of Equation (10), we use the densities introduced in Biot's original theory[11]:

$$\rho_{11}\ddot{\mathbf{u}}^s + \rho_{12}\ddot{\mathbf{u}}^f = (1-f)\,\nabla \cdot \boldsymbol{\sigma}^s \tag{13a}$$

$$\rho_{12}\ddot{\mathbf{u}}^s + \rho_{22}\ddot{\mathbf{u}}^f = f\nabla\sigma^f \tag{13b}$$

with $\rho_{11} = (1-f)\,\rho^s - \rho_{12}$, $\rho_{22} = f\rho^f - \rho_{12}$, and coupling density $\rho_{12} < 0$. ρ^f and ρ^s are the densities of the fluid and the solid, respectively. The coupling density describes the transfer of shear motion between the compartments; since the fluid does not support shear motion itself, it acts as a parasitic mass that is "dragged along" by the solid, exerting a decelerating force which renders ρ_{12} negative.

Applying the curl operator to Equations (13a and 13b) yields the equations for the shear fields only, with $\mathbf{c} = \nabla \times \mathbf{u}$:

$$(1-f)\,\rho^s\ddot{\mathbf{c}}^s + \rho_{12}\left(\ddot{\mathbf{c}}^f - \ddot{\mathbf{c}}^s\right) = (1-f)\,\nabla \times \nabla \cdot \boldsymbol{\sigma}^s \tag{14a}$$

$$f\rho^f\ddot{\mathbf{c}}^f + \rho_{12}\left(\ddot{\mathbf{c}}^s - \ddot{\mathbf{c}}^f\right) = f\nabla \times \nabla\sigma^f = 0 \tag{14b}$$

In the second equation, we used the fact that $\nabla \times \nabla\xi = \mathrm{curl}\,\mathrm{grad}\xi = 0$ for any scalar field ξ. The second equation allows us to establish a relationship between the 2 shear displacement fields:

$$\ddot{\mathbf{c}}^f = -\frac{\rho_{12}}{f\rho^f - \rho_{12}}\ddot{\mathbf{c}}^s. \tag{15}$$

Since $\rho_{12} < 0$ and $f, \rho_f > 0$, the proportionality constant between $\ddot{\mathbf{c}}^f$ and $\ddot{\mathbf{c}}^s$ is real and positive. For oscillating displacements, $\tilde{\mathbf{c}} = \mathbf{c} \cdot e^{i(\omega t + \phi_0)}$, the 2 displacement fields can be expected to have approximately the same phase $\phi_0 + \omega t$.

3 | METHODS

Porosity estimation based on IR-MRI was developed and tested in two types of phantoms: one consisting of two separate liquid compartments of different T_1 relaxivity for emulating biphasic relaxation behavior, and the second phantom made of tofu for mimicking solid tissue with different porosities saturated by a fluid. For the in vivo part of the study, IR-MRI was used to determine porosity in the brains of 21 healthy volunteers (6 female and 15 male; mean age: 35 ± 10 years, age range: 23-58 years), and finally, IR-MRE was performed in seven volunteers (four female and three male; mean age: 33 ± 6 years, age range: 25-41 years). The study was approved by the institutional review board. All participants gave written informed consent.

3.1 | Fluid-fluid phantom

For the first experiment, a pair of saline solutions was prepared. Two 100-ml flat rectangular containers were filled with physiological saline solutions; one of them was doped with 10^{-4} mol/L gadolinium (Dotarem, Guerbet, Roissy, France) and attached to the other container to emulate 2 spatially separated fluid reservoirs of different T_1 relaxation times (see Figure 1).

3.2 | Solid-fluid phantoms

Eight tofu samples were produced in Plexiglas cylinders 5.6 cm in diameter, as described by Streitberger et al,[18] with different porosities by applying different amounts of pressure (Figure 2A). Reference porosities were determined after the IR-MRI experiments by measuring the drainable liquid volume. Due to water retention by surface adhesion, complete drainage of the free fluid would only have been

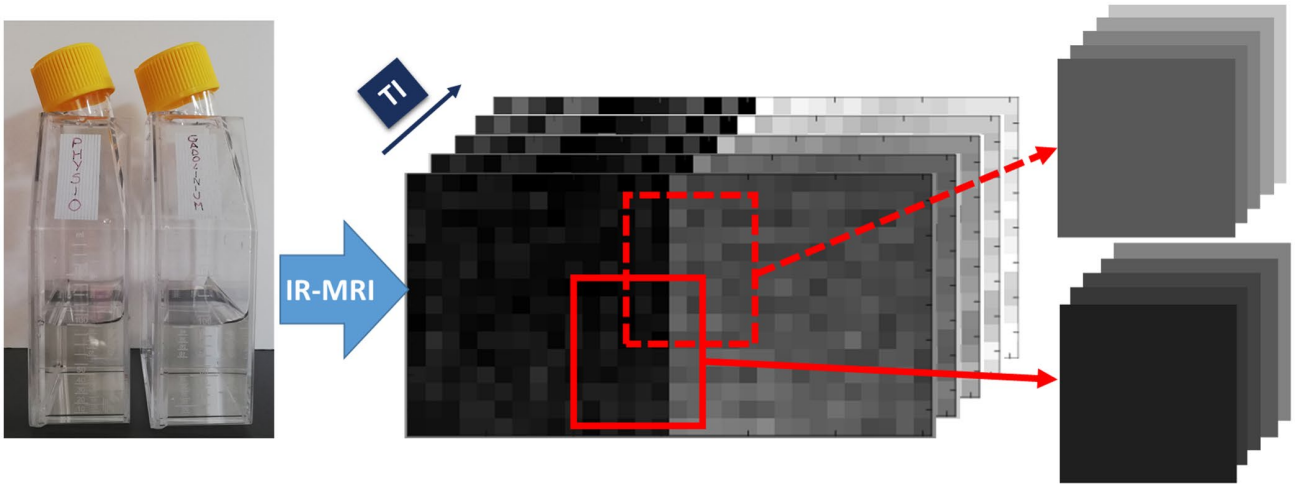

FIGURE 1 On the left, the two flat containers with the physiological solution and the gadolinium-doped solution are shown. After IR-MRI, ROIs were defined, including voxels from both fluids at different ratios at each TI to emulate supervoxels composed of the two media. The ratio at which voxels from both fluids are combined corresponds to the emulated porosity

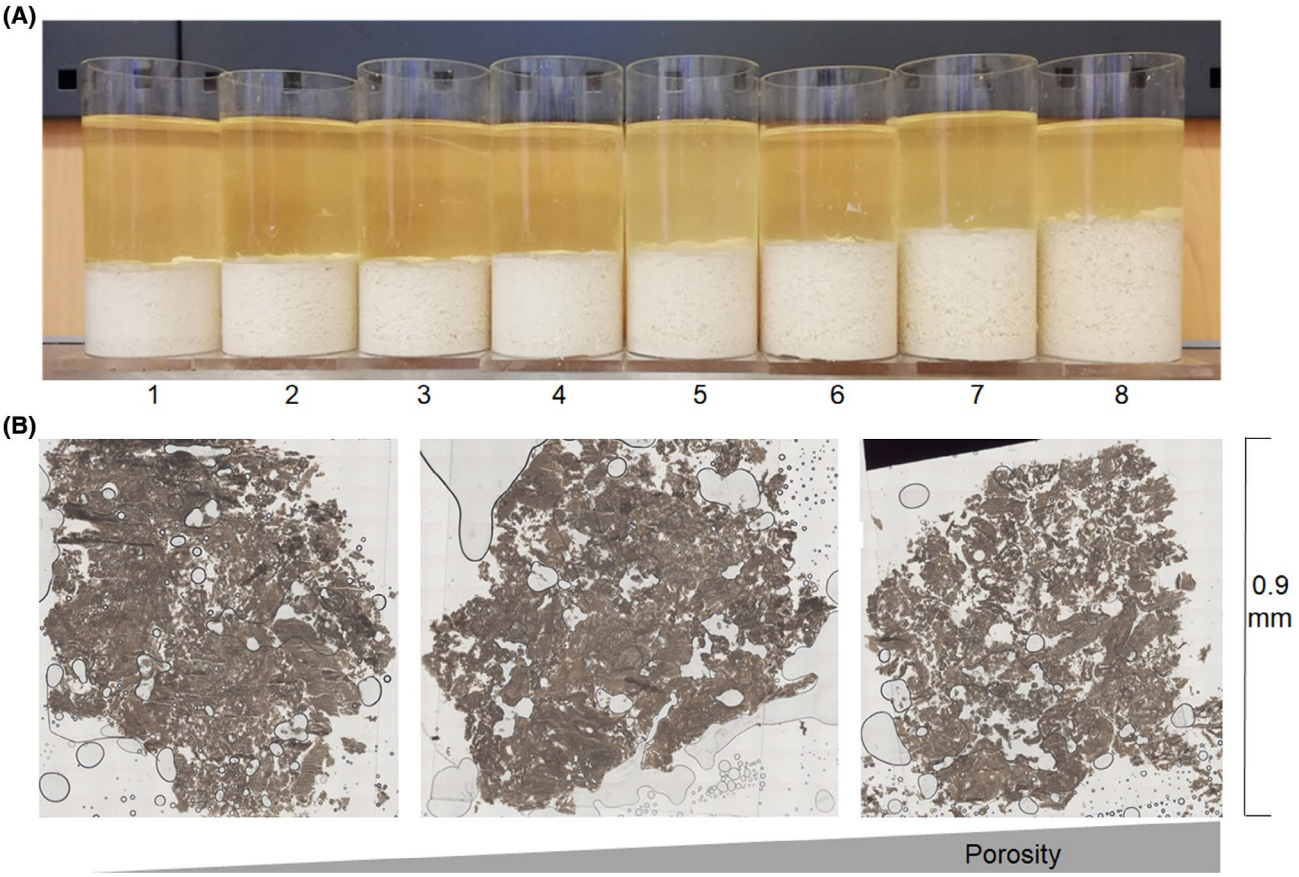

FIGURE 2 A, Eight tofu samples of increasing porosity from left to right. Remaining excess fluid above each tofu sample was used to quantify T_1 relaxation time of the pore fluid compartment. B, Three samples were extracted from the same tofu phantom to produce micrographs. The empty holes inside the sample are pores, in which the fluid compartment of the porous phantom can flow. The bubbles that appear in the images are attributable to the wet mount technique (Leica CV mount, Leica Biosystems, Richmond, USA), necessary to avoid shrinkage of the sample in contact with Kawamoto's adhesive tape. The micrographs show three different porosities, 0.11 ± 0.03, 0.13 ± 0.05, and 0.19 ± 0.04 (from left to right)

possible with excessively long drainage times, which in turn would have biased our results due to water evaporation or condensation. Therefore, we uniformly stopped the drainage after 10 min and extrapolated the experimentally quantified drainage rate to an infinite drainage time using a simple exponential decay model. Furthermore, an additional tofu sample was produced to evaluate the microscopic structure of the material. Cubes of approximately 1 cm^3 were excised from different locations in the tofu phantoms, fixed in paraformaldehyde, dehydrated in 20% sucrose solution for 48 h, and frozen in liquid nitrogen. Slices of 50 μm thickness were prepared according to Kawamoto's film method[19] using a cryostat (Leica CM 1850 UV, Nussloch, Germany), and light transmission microscopy (Figure 2B) was performed (Zeiss Axio Observer for Biology, Jena, Germany). From these micrographs, average porosity was calculated as the ratio of the pore area to the total area of the region of interest (ROI) after image segmentation.

Three additional tofu phantoms were similarly produced for the IR-MRI/IR-MRE experiments. In order to obtain larger phantoms, these were produced in cylindrical vessels with a diameter of 9.5 cm. For this purpose, the soy milk was first concentrated by evaporating a third of its volume before coagulation.

3.3 | IR-MRI/IR-MRE

All IR-MRI data were acquired with a single-shot spin-echo echo-planar imaging (EPI) sequence preceded by a slice-selective inversion pulse, preceded by a reference scan without inversion. The IR-MRI parameters used in the different experiments are compiled in Table 1. In the phantom studies, pauses were inserted between acquisitions to ensure that the effective TR was higher than $5 \cdot T_1^f$.

Additionally, in all in vivo IR-MRI experiments, T_1-weighted volumetric MRI was performed using an MP-RAGE (magnetization-prepared rapid gradient echo) sequence for anatomical reference.

For IR-MRI/IR-MRE experiments, IR-MRI was performed first at different TIs. Afterward, without moving the phantom or the volunteer, IR-MRE was performed twice, once without IR and second with a TI equal to the nulling TI of the fluid compartment. In the brain study, the fluid compartment was CSF, which was suppressed with TI = 2900 ms as priorly estimated from the relaxation measurement. The vibration frequency was 20 Hz and was induced using 2 pressurized air drivers placed side by side under the head and operated in opposed-phase mode.[20] Motion-encoding gradient (MEG) frequency was 39.53 Hz with 20 mT/m amplitude.

TABLE 1 Acquisition parameters used in the IR-MRI and IR-MRI/IR-MRE experiments

	Pure fluid phantom	Tofu phantom	In vivo brain imaging	Tofu phantom (for IR-MRI/MRE)	In vivo brain imaging (for IR-MRI/MRE)
MRI scanner	1.5T Siemens Sonata	1.5T Siemens Sonata	3T Siemens Trio	3T Siemens Prisma^{Fit}	3T Siemens Prisma^{Fit}
Coil	single-channel head coil	single-channel head coil	12-channel head coil	32-channel head coil	32-channel head coil
TE (ms)	36	35	45	65	65
TR (ms)	5150	6000	40550	17380	20000
Matrix size	32 × 88	112 × 32	100 × 100	108 × 110	108 × 110
Voxel volume (mm^3)	1.85 × 1.85 × 1.90	2 × 2 × 2	2 × 2 × 2	2 × 2 × 2	2 × 2 × 2
Slices	1	16	5	5	5
Interslice gap (mm)	–	2	2	2	2
TIs (ms)	120, 170, 220, 270, 320, 370, 420, 470, 520, 620, 720, 820, 920, 1020, 1220, 1420, 1620, 1820, 2020, 2220, 2420, 2620, 2820, 3020, 3400, 3800, 4200, 4600, 5000	120, 170, 220, 270, 320, 370, 420, 470, 520, 570, 620, 720, 820, 920, 1020, 1120, 1220, 1420, 1620, 1820, 2020, 2420, 2820, 3220, 3620	120, 250, 380, 510, 900, 1100, 1300, 1500, 1700, 1900, 2200, 2500, 2800, 3100, 3400, 3800, 4200, 4600, 5000	100, 200, 300, 400, 500, 600, 700, 800, 900, 1000, 1200, 1400, 1600, 1800, 2000, 2500, 3000, 3500, 4000, 5000	100, 200, 400, 600, 800, 1000, 1200,1600, 2000, 2500, 3000, 3500, 4000, 4500, 5000, 6000
Parallel imaging	–	–	Grappa factor 2	–	–

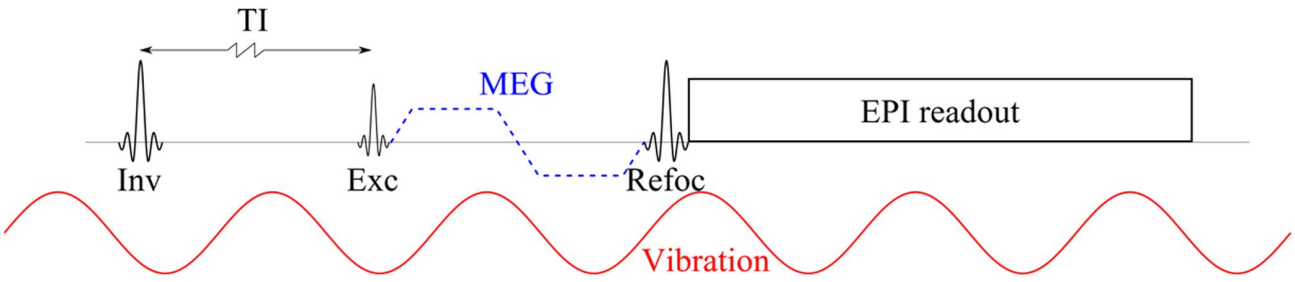

FIGURE 3 Sequence diagram of the acquisition of a single slice with the IR-MRI (black components) and IR-MRE (including MEG and vibration) protocol. The symbols denote: Inv: slice-selective inversion pulse; Exc: slice-selective 90° excitation pulse; Refoc: slice-selective 180° refocusing pulse; MEG: motion-encoding gradient (0th moment nulled, no flow compensation). The acquisition scheme is repeated identically for each slice of the imaging volume. The relative phase between the continuous vibration and the MEG was incremented in eight steps equally spaced over a full oscillation cycle, leading to a total of eight vibration phases × three MEG directions = 24 scans per slice for a single MRE acquisition. For IR-MRI, 16 to 29 scans were performed with different TIs to obtain a dense sampling of the relaxation curve. Two experiments were performed for IR-MRE: a reference scan without inversion pulse (corresponding to $TI = \infty$) and a second scan with TI for CSF-nulling

A diagram of the newly developed IR-MRE sequence is shown in Figure 3. The in vivo scanning session was supplemented by a T_1-weighted MP-RAGE sequence for segmentation. The total scan time per volunteer was approx. 30 min.

3.4 | Data processing

The "pure fluid" phantom data were processed in two steps: first, T_1 relaxation time, signal amplitude I, and noise offset C of each of the two fluids were obtained by fitting the monoexponential Equation (1) to the single-compartment IR-MRI signals within each of the two compartments. The signal of multiple ROIs, each containing voxels from both compartments at different ratios, was averaged into synthetic "supervoxels," emulating the biphasic signal from voxels with different porosities (see Figure 1). For consistency with theory, we refer to the saline solution with longer T_1 as the fluid and the Gd-doped solution with shorter T_1 as the solid. For each ROI, the fraction of voxels from the long-T_1 compartment in the ROI was taken as ground truth porosity. IR-MRI porosity of a biphasic supervoxel was derived by fitting either the full Equation (3) or reduced Equation (5) to the biexponential relaxation signal. As explained in the Theory section, T_1 and I values of the fluid compartment needed to be quantified separately and were used as input variables for our biphasic model to improve fitting stability. Consequently, T_1^f and I^f retrieved from the pure physiological saline solution were used as constants for the biphasic fit of either full Equation (3) or reduced Equation (5) in order to reconstruct T_1 times of the gadolinium-doped solution and porosities of the emulated supervoxels.

Solid-fluid tofu phantom data were analyzed by (1) fitting the IR-MRI signal decay of the excess fluid on top of the phantom with a monophasic model (Equation 1) in order to extract T_1^f and I^f and (2) using these parameters as constants for the biexponential fits (Equation 5) of the biphasic tofu IR-MRI signal.

The same strategy was applied to in vivo IR-MRI data by treating CSF properties as dominating fluid properties of brain tissue. Hence, the IR-MRI signal of CSF in the lateral ventricles was (1) analyzed by monoexponential fitting (Equation 1) for determination of T_1^f and I^f and (2) using these values as constants for fitting the biexponential signal relaxation of the IR-MRI (Equation 5) was applied to the brain data on a voxel-by-voxel basis.

In the IR-MRI/IR-MRE experiments, the IR-MRI scans were processed in the same way as in the previous IR-MRI experiment to obtain f and T_1^s maps aligned with the IR-MRE scans. Equation (8) was solved to obtain the displacement field of the fluid compartment. The fluid compartment being present at a lower quantity than the solid, its relative displacement field is more sensitive to noise than the solid compartment. Therefore, it was then filtered with a Butterworth low-pass filter with a cutoff of 50 m^{-1} and order 1. The curl of the fluid and solid displacement fields was calculated using central differences for interior data points and single-sided differences at the end points. Afterward, ρ_{12} was estimated by solving Equation (15). We assumed $\rho^f = 1000$ kg/m^3, equal to the density of water.

3.5 | Statistical analysis

In the IR-MRI in vivo experiments, for generating tissue probability maps of gray matter (GM), white matter (WM), and CSF, IR-MRI scans were co-registered to MP-RAGE images using Statistical Parametric Mapping (SPM) 12 software (The Wellcome Centre for Human Neuroimaging, London, UK) and segmented using the extended version of the unified segmentation routine.[21] Porosity maps and T_1 maps were segmented based on SPM-generated probability maps. A voxel was assigned to a compartment if its probability value for that compartment exceeded 80%. Group mean values and SDs of CSF T_1 and monophasic T_1, compartmental T_1, and porosity

of GM and WM were calculated. A paired *t*-test analysis was performed for average porosity and normalized solid T_1 values of WM and GM in each volunteer. Statistical tests were performed in Matlab (Mathwork Inc., Natick, USA, version 2018), discarding all values for which the coefficient of determination, R^2, of the fitting was lower than 0.9.

In the IR-MRE phantom and in vivo experiments, the magnitude and oscillation phase of the curl components after Fourier transform were analyzed separately. A right-tailed *t*-test was used to test if the magnitude of the solid curl component was higher than the amplitude of the fluid component, as predicted by theory. To test the assumption that solid and fluid oscillate in phase, as predicted by theory (Equation 15), the motion phase from one compartment was plotted versus that of the other on a per-voxel basis, and linear regression was calculated for each sample and each volunteer. Due to the instabilities caused by the denominator of the rearranged Equation (15), $\rho_{12} = \frac{f\rho^f \ddot{c}^f}{\ddot{c}^f - \ddot{c}^s}$, voxels with $|\ddot{c}^s| < 5 \cdot 10^{-4}$ were removed from the statistical analysis. Statistical significance was assumed for $P < .05$. Median and interquartile intervals were estimated for each tofu sample and in the in vivo brain for WM and GM separately.

4 | RESULTS

4.1 | Fluid-fluid phantom

Figure 4 displays IR-MRI results obtained in the fluid-fluid phantom obtained with the full model (Equation 3) and the reduced model (Equation 5). Error bars indicate that the SE of estimated parameters is smaller for the reduced Equation

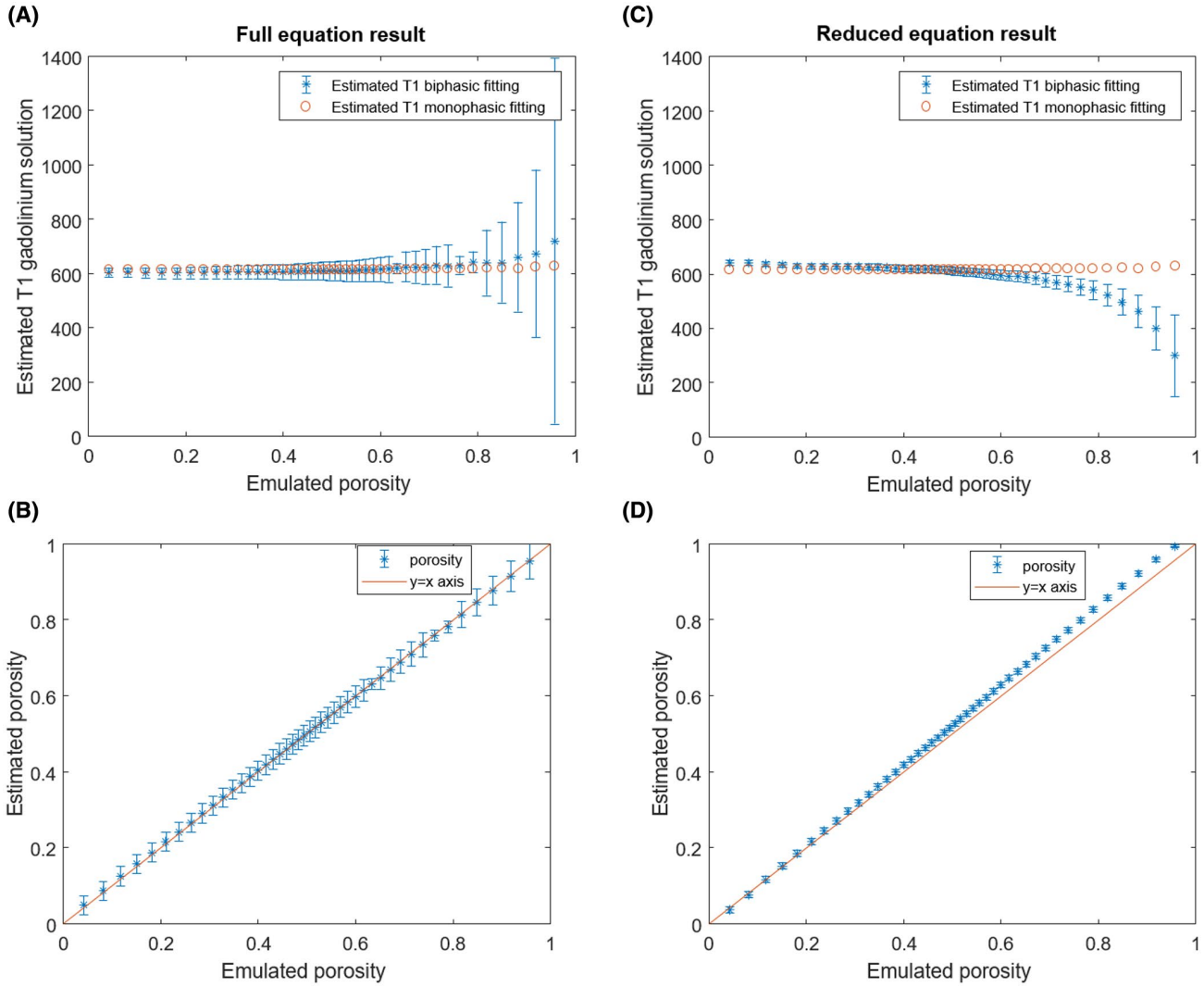

FIGURE 4 A, Comparison of T_1 of the gadolinium solution obtained by fitting the full biphasic model (Equation 3) to the supervoxel data and T_1 of the same solution obtained by fitting the monophasic model (Equation 1) only to the voxels of the doped solution contained in the same supervoxel. B, Comparison of IR-MRI-derived porosity obtained with the full model (Equation 3) and emulated porosity. C and D, Same analysis as A/B, but for data obtained with the reduced model (Equation 5). In each figure, the error bars represent the SE of estimation of the evaluated parameter

(5) (mean SE of f: ±0.007, of T_1^s: ±22 ms) than for the full Equation (3) (mean of f: ±0.03, of T_1^s: ±63 ms). However, Equation (5) tends to underestimate T_1^s and to overestimate porosity at higher ground truth porosities. For example, at ground truth porosities $f > 0.8$, we identified an overestimation of f on the order of 4% and of T_1^s on the order of 3%. Nevertheless, porosities reconstructed using the reduced Equation (5) were in excellent agreement with ground truth (R = 1, $P = 0$, mean residual error of porosity: ±0.02).

4.2 | Solid-fluid phantoms IR-MRI

The porous nature of the solid-fluid phantoms was confirmed by microscopy images, as shown in Figure 2B. Porosities in different regions quantified by image analysis were 0.11 ± 0.03, 0.13 ± 0.05, and 0.19 ± 0.04, indicating an inhomogeneous porous structure across macroscopic distances (Supporting Information Figure S1, which is available online).

Figure 5A shows porosity maps of the central slice of each tofu sample reconstructed from IR-MRI using Equation (5). Mean porosities ranged from 0.12 to 0.27. Porosity determined by draining tofu samples ranged from 0.08 to 0.30, indicating good agreement of IR-MRI with reference porosity values. Figure 5B presents spatially averaged IR-MRI porosity values versus draining porosity. The error bars of the IR-MRI porosity data represent the SD of porosity across slices, while the error bars of the draining porosity data correspond to the measurement error. IR-MRI porosity is correlated with draining porosity (R = 0.99, $P < 10^{-5}$). Because water adhesion causes retention of some of the free water in the tofu, draining porosity is prone to underestimation in tofu, especially at low porosities.

4.3 | In vivo brain study IR-MRI

Figure 6 shows IR-MRI porosity and solid-tissue T_1 of in vivo brain. Average CSF T_1 across all volunteers was 4257 ± 157 ms, while T_1^s and f were 1172 ± 36 ms and 0.14 ± 0.02 in GM and 800 ± 15 ms and 0.05 ± 0.01 in WM, respectively. These parameters were statistically significantly different between GM and WM (all $P < 10^{-16}$). Nevertheless, porosity and T_1^s represent independent information, as demonstrated by the histograms shown in Figure 7. These plots illustrate that T_1^s values are distributed with 2 distinct peaks corresponding to GM and WM, whereas porosity displays a more continuous single-peaked and wider distribution.

4.4 | Solid-fluid phantoms IR-MRI/IR-MRE

As shown in Figure 8A, the average shear wave amplitude in the solid is higher than in the fluid ($P < .05$). Voxel-by-voxel linear fitting of the phases of $\boldsymbol{c}^f$ and $\boldsymbol{c}^s$ resulted in

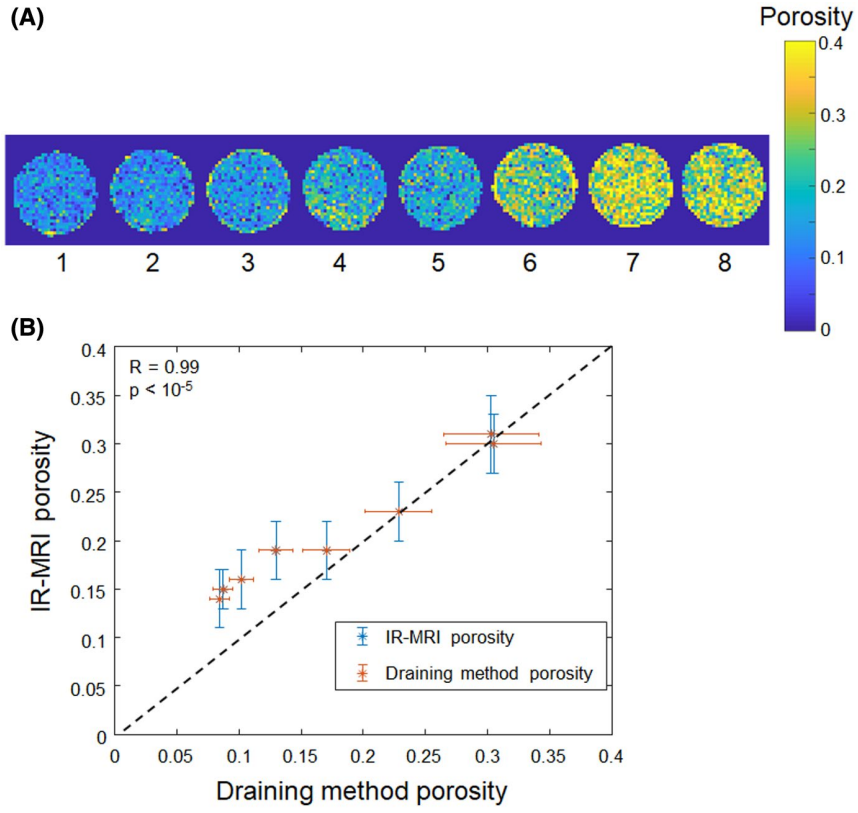

FIGURE 5 A, Porosity maps of the central slice of each of the eight tofu samples shown in Figure 1. B, IR-MRI-derived porosity plotted versus the porosity obtained by draining the fluid compartment from the samples. The black dashed line represents perfect agreement of the two methods. The error bars for IR-MRI porosity represent the SD of interslice average porosity, while the error bars for draining porosity represent the measurement error of the tofu and drained fluid volumes, propagated to the porosity value

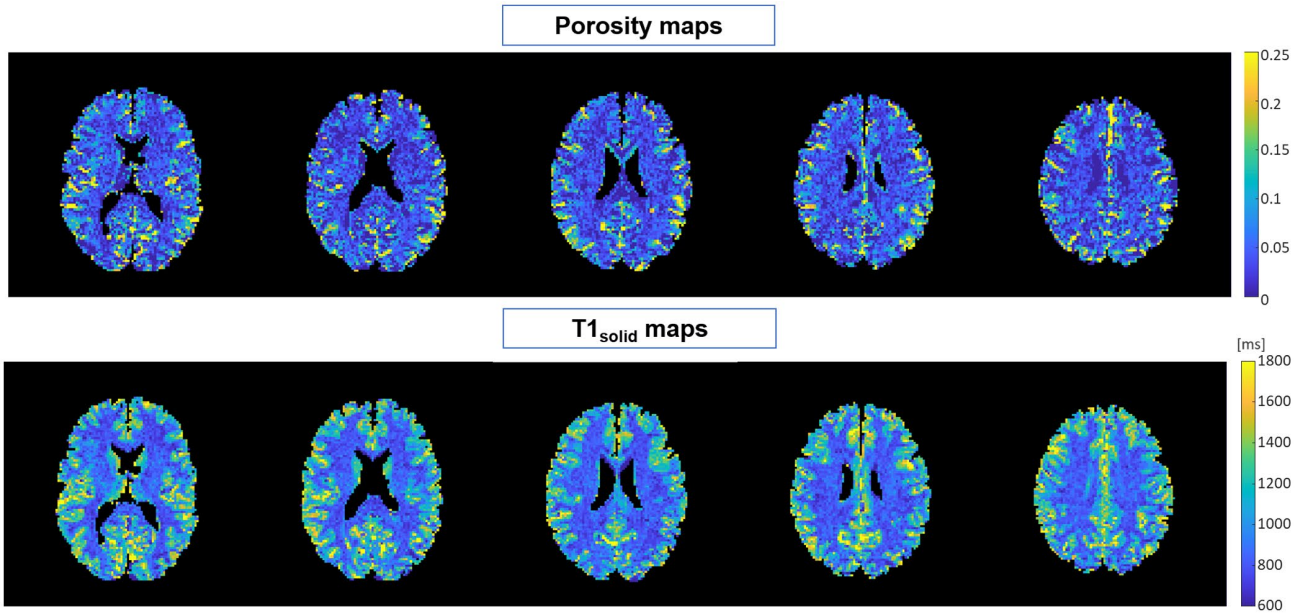

FIGURE 6 Porosity maps (top row) and T_1^s maps (bottom row) of five slices from one volunteer. In both sets of slices, CSF-filled regions, such as the ventricles, are excluded from analysis. As discussed for the liquid-liquid phantom, biphasic fitting reliability is not optimal in areas with porosity >0.5

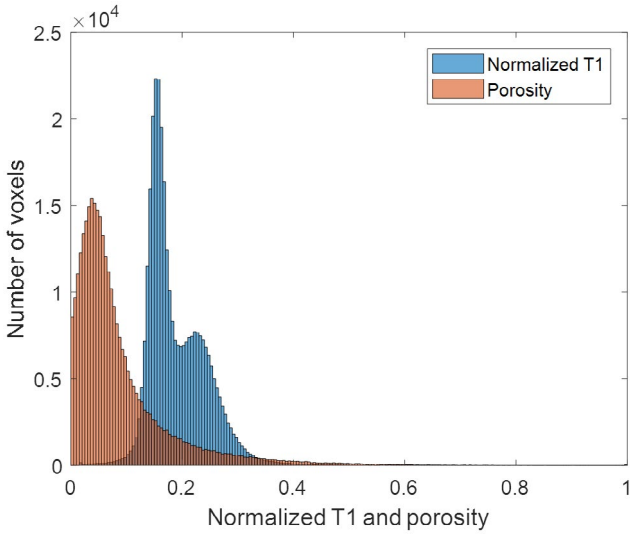

FIGURE 7 Histograms of normalized T_1 and porosity of the brain pooled across all volunteers. T_1 values were rescaled between 0 and 1. The two distributions are clearly different: porosity shows only one peak, while T_1^s reveals two distinct peaks that coincide with mean T_1^s values in GM and WM

an average slope of 0.93 ± 0.07, offset of 0.10 ± 0.01, and R^2 = 0.90 ± 0.07. As an example, the phase data fitting obtained from the same sample as in Figure 8A is shown in Figure 8B. Maps of ρ_{12} were produced for each slice (Figure 8A). The distribution of ρ_{12} is strongly asymmetrical (Supporting Information Figure S2), therefore median and interquartile range were calculated and resulted in −114 (−318, −24) kg/m^3, −117 (−330, −21) kg/m^3, and −190 (−511, −22) kg/m^3 for the three tofu phantoms.

4.5 | In vivo brain study IR-MRI/MRE

Figure 9A shows the curl of the solid and fluid. The average shear wave amplitude in the solid is higher than in the fluid in each volunteer ($P < .05$). Voxel-by-voxel linear fitting of the phases of $\ddot{\boldsymbol{c}}^f$ and $\ddot{\boldsymbol{c}}^s$ resulted in an average slope of 0.98 ± 0.01, offset of −0.01 ± 0.09, and R^2 = 0.95 ± 0.02. As an example, the phase data fitting obtained from the same volunteer as in Figure 9A is shown in Figure 9B. Maps of ρ_{12} were produced for each slice (Figure 9A), and group average medians of −22 ± 29 kg/m^3 and −38 ± 4 kg/m^3 were obtained for GM and WM, respectively.

5 | DISCUSSION

In this study, we introduced an in vivo porosity quantification technique based on T_1 relaxation measurement combined with MRE to separate solid and fluid displacement fields and to estimate dynamic coupling density.

The fluid-fluid phantom experiment served as a first validation of porosity estimation in a highly simplified setting. It incorporated biexponential fitting with four variables and resulted in stable values over a wide range of porosities ($f < 0.9$). Furthermore, it was shown that the simplified model (Equation 5) with only three free parameters produced

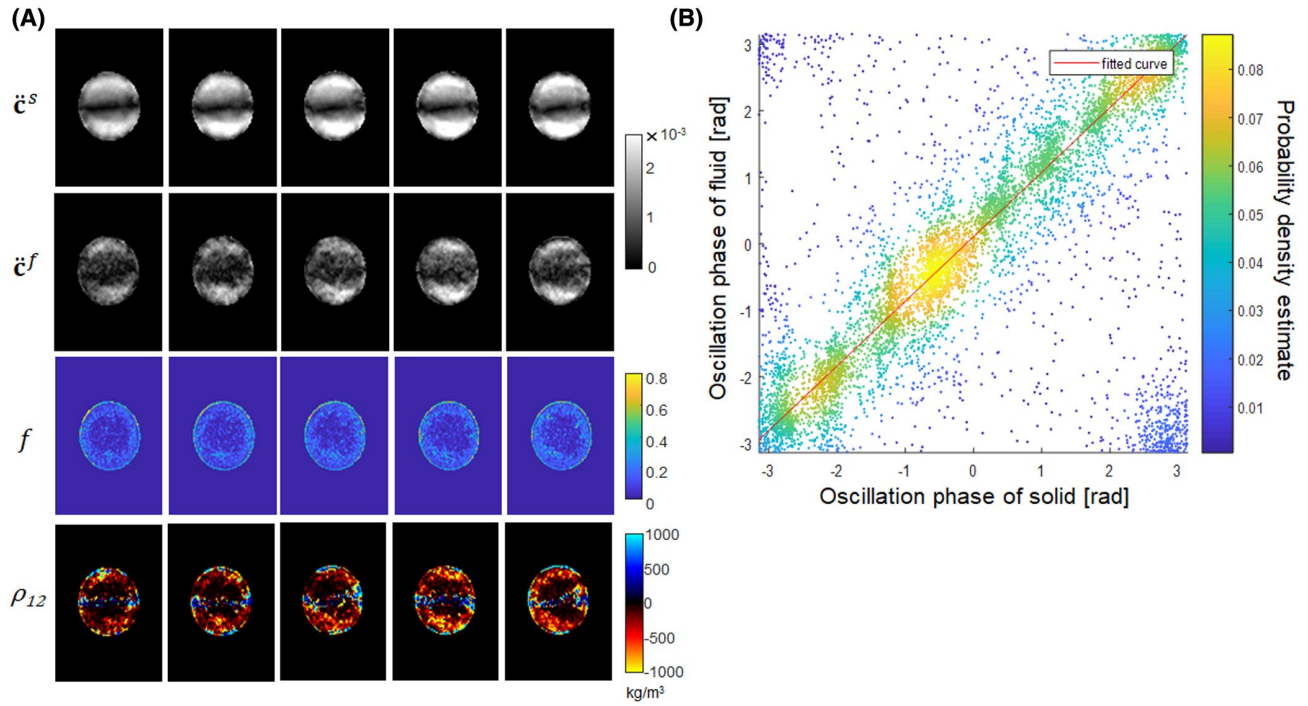

FIGURE 8 A, Magnitude of the through-plane component of the curl of the solid compartment (first row) and fluid compartment (second row) of a tofu sample. The curl of the solid compartment shows higher values than that of the fluid compartment. Porosity maps (third row) and corresponding ρ_{12} maps. B, Voxel-by-voxel plot of the fluid and solid curl phase. The color map represents the probability density estimate of the points in the plot, and the red line represents the linear regression of the plotted data. Due to phase circularity along both axes, the wrapped data points in the top left and bottom right corners cannot be unwrapped unambiguously. However, their effect on linear regression was found to be negligible

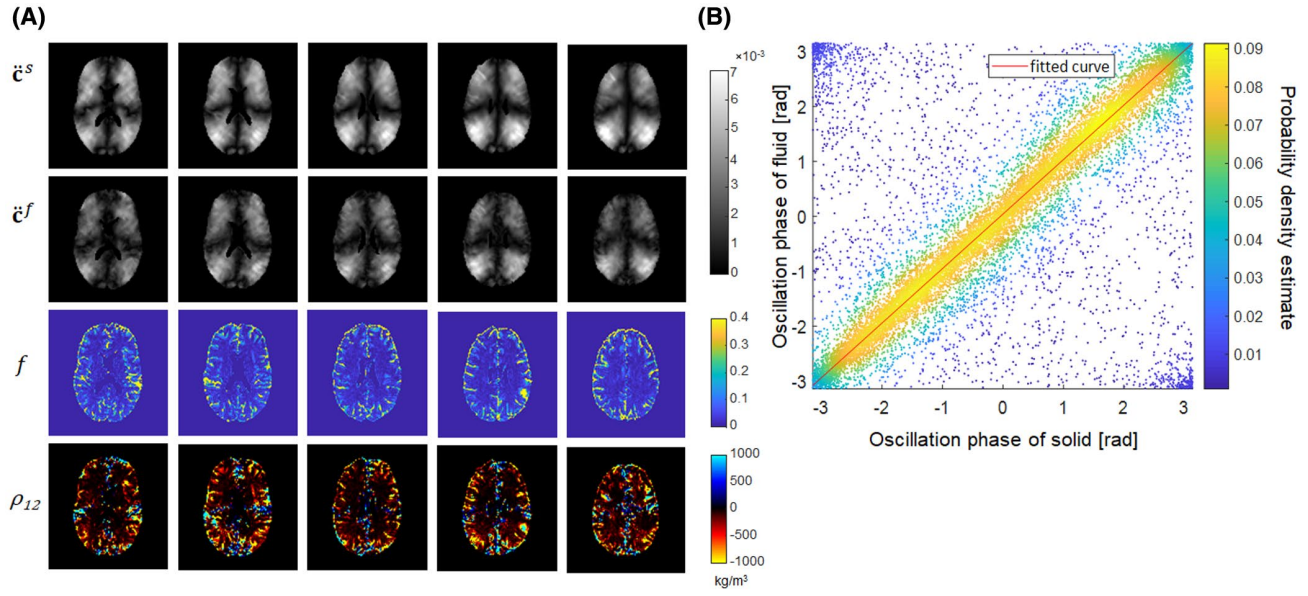

FIGURE 9 A, Magnitude of the through-plane component of the curl of the solid compartment (first row) and fluid compartment (second row). Furthermore, porosity map, and corresponding ρ_{12} maps of a healthy volunteer are shown. B, Voxel-by-voxel plot of the phase of the fluid and solid curl in the same healthy volunteer shown in Figure 8

comparable results within a more constrained range of porosities ($f < 0.5$). However, most biological soft tissues have porosities below the threshold of 0.5: for example, previous studies have shown that average liver tissue porosity is 14%[22], while brain extracellular space (ECS), which contains the fluid volumes quantified by our IR-MRI method, has a

porosity on the order of 20%.[15] Since this is clearly below 50%, we consider the simplified model of Equation (5) valid for IR-MRI reconstruction.

The solid-fluid phantom made of tofu allowed us to validate our method in a biphasic soft-tissue-mimicking material. As with biological tissues, the assumption that tofu, with its composition of an interspersed aqueous solvent and coagulated proteins, can be separated into two distinct compartments is an oversimplification. Furthermore, as revealed by microscopy, the heterogeneity of pores in tofu on the millimeter scale imposes challenges in defining ground truth porosity. Our method for quantifying drainage velocity in conjunction with exponential extrapolation improved the estimation of reference porosity and was more consistent than other methods, including microscopic analysis (Supporting Information S1) or measurement of the fluid volume drained after a fixed drainage time. Nevertheless, there is an offset between draining porosity and IR-MRI, which we attribute to water adhesion at polar groups of the coagulated soy proteins, which in turn leads to retention of aqueous solvent within the solid tissue matrix. Albeit not accessible by drainage, such compartments of retained fluid might still contribute to IR-MRI-derived porosity, while resulting in an overall underestimation of draining porosity.

The biphasic equation (Equation 5) collapses in the quasi-monophasic edge cases $f \to 0$ and $f \to 1$. Therefore, we excluded the ventricles and voxels with $f < 10^{-4}$ from further analysis. Overall, 0.5% of voxels were discarded because of unreliable fitting ($R^2 < 0.9$), and an additional 16.8% of the remaining voxels were discarded based on the $f < 10^{-4}$ criterion.

In the brain, magnetization transfer (MT) effects have to be considered that can interfere with T_1 relaxation measurements.[23,24] To assess the potential effect of MT on porosity estimation, we performed an additional experiment in three healthy volunteers in which we compared the standard IR-MRI protocol, as described above, with a modified version of the protocol with only two slices and excessively long idle time (60 s) between slice acquisitions to allow for complete relaxation between excitations. This experiment revealed that the difference between these 2 scans caused an uncertainty in the porosity estimation of $(17 \pm 14)\cdot 10^{-3}$, $(43 \pm 15)\cdot 10^{-3}$, and $(44 \pm 35)\cdot 10^{-3}$ in homogeneous WM regions for the three subjects. We conclude that, while MT does have an effect on porosity quantification, it does not limit the general applicability of the proposed method (Supporting Information Figure S3). Nevertheless, a sequence optimized to minimize MT would potentially improve the accuracy of the method.

The histograms of T_1 and porosity, as shown in Figure 7, with a single peak in the porosity data and two peaks for T_1, indicate that there is no monotonous mapping between these two quantities, that is, they can be considered to represent unrelated information. Naturally, the type of fluid depends on the specific type of tissue under investigation. In brain tissue, ECS mainly contains a fluid similar in composition to CSF.[25] Several studies have determined the ECS volume fraction[26-28] reporting values between 15% in WM and 30% in GM of in vivo rat brain.[15] In contrast, the vascular volume in the brain does not exceed 3% in GM and 1.5% in WM.[29] As a consequence, blood, with its significantly shorter T_1 than CSF, as well as other short-T_1 liquids, will at least partially be classified as belonging to the solid compartment, thus leading to systematic underestimation of total porosity. In addition to blood, bound water within the ECS which cannot freely move and, thus, exhibits much shorter T_1-times than free CSF, can be considered as part of the solid matrix, both for T_1-relaxation times and mechanically As a result, brain porosity measured by our IR-MRI method is lower than the values reported in the aforementioned studies and should rather be interpreted as CSF porosity.

The shear wave amplitude of the fluid is significantly lower than that of the solid, in both tofu and brain. As predicted by theory, the phases of fluid and solid motion were correlated, indicating in-phase oscillation of the two compartments at different amplitudes. The ρ_{12} maps are encouraging, as they show negative values in agreement with the theory, except for regions of zero deflection amplitudes (e.g., in the vicinity of standing wave nodes), making the difference between curl components in Equation (15) prone to sign errors, as shown in Figures 8A and 9A (Supporting Information Figure S4). The higher SD in GM is a consequence of many voxels near the segmented CSF with porosities higher than 0.5, which, as discussed, lead to an unstable estimation. Knowledge of compartmental displacement fields is a major step toward the full exploitation of the poroelastic medium model in the context of MRE, which has been previously supported by parameter assumptions[3] or an effective medium approach.[9] Separation of the displacement fields could contribute to the further advancement of elastography and poroelastography of hydrocephalus[30-32] and, thus, help in further elucidating the development of the disease and improving its diagnosis. Our results could also contribute to a deeper understanding of brain tumors, especially glioblastoma and meningioma, whose "anomalous" mechanical behavior has been detected by brain elastography.[18]

Our study has a few limitations. First, our model is biphasic and homogeneous in each voxel with respect to the MRI signal, assuming a sharp peak in the relaxation time spectrum of each compartment. This assumption ignores proton exchange across interfaces between different pools of protons,[33] magnetization transfer, the widening of the peaks based on proton interactions, and continuous T_1 spectra. Second, inversion of the biexponential model is ill-conditioned when porosity approaches the limits of 0 or 1, which is not an issue in typical biological soft tissues as long as fluid-filled spaces are excluded from porosity analysis. Finally, possible slight

movement of volunteers can cause a spatial mismatch between the inverted and non-inverted MRE scans, requiring additional alignment steps.[34] In this work, the volunteers' head position was fixed with thick cushions to minimize head motion.

6 | CONCLUSIONS

We have demonstrated for the first time that the combination of IR-MRI and IR-MRE in conjunction with specialized data processing techniques can successfully disentangle externally induced fluid and solid displacement fields in the in vivo human brain. IR-MRI allowed quantification of brain tissue porosity based on simplification of highly complex fluid-solid interactions in biological tissues. Porosity, which reflects the fluid-volume fraction of the human brain, was inferred from a biphasic model, and validation was supported by microscopic and drainage-based analysis in tofu phantoms. Reconstructed coupling density values are negative in both phantoms and in vivo brain, in agreement with theory. Our findings are intended to inspire future studies of soft tissues, which can be successfully modeled as poroelastic media, and to propose a new method for evaluating the interaction of the two constituent compartments.

ACKNOWLEDGMENTS

The authors gratefully acknowledge support from the German Research Foundation (GRK2260 BIOQIC, SFB1340 Matrix in Vision). We thank Helena Radbruch, M.D., and Angela Ariza de Schellenberger, Ph.D., for their valuable help in the fields of histology and microscopy. Open access funding enabled and organized by Projekt DEAL.

ORCID

Ledia Lilaj https://orcid.org/0000-0001-8222-0397
Jürgen Braun https://orcid.org/0000-0001-5183-7546
Ingolf Sack https://orcid.org/0000-0003-2460-1444
Sebastian Hirsch https://orcid.org/0000-0001-8187-8242

REFERENCES

1. Muthupillai R, Lomas DJ, Rossman PJ, Greenleaf JF, Manduca A, Ehman RL. Magnetic resonance elastography by direct visualization of propagating acoustic strain waves. *Science*. 1995;269:1854-1857.
2. Franceschini G, Bigoni D, Regitnig P, Holzapfel GA. Brain tissue deforms similarly to filled elastomers and follows consolidation theory. *J Mech Phys Solids*. 2006;54:2592-2620.
3. Mcgarry MDJ, Johnson CL, Sutton BP, et al. Suitability of poroelastic and viscoelastic mechanical models for high and low frequency MR elastography. *Med Phys*. 2015;42:947-957.
4. Armstrong CG, Mow VC. An analysis of the unconfined compression of articular cartilage. *J Biomech Eng*. 1984;106:165-173.
5. Fortin M, Buschmann MD, Bertrand MJ, Foster FS, Ophir J. Dynamic measurement of internal solid displacement in articular cartilage using ultrasound backscatter. *J Biomech*. 2003;36:443-447.
6. Righetti R, Garra BS, Mobbs LM. The feasibility of using poroelastographic techniques for distinguishing between normal and lymphedematous tissues in vivo. *Phys Med Biol*. 2007;52:6525.
7. Biot MA. General theory of three-dimensional consolidation. *J Appl Phys*. 1941;12:155-164.
8. Mcgarry M, Van Houten E, Solamen L, Gordon-Wylie S, Weaver J, Paulsen KD. Uniqueness of poroelastic and viscoelastic nonlinear inversion MR elastography at low frequencies. *Phys Med Biol*. 2019;64:075006.
9. Hirsch S, Klatt D, Freimann F, Scheel M, Braun J, Sack I. In vivo measurement of volumetric strain in the human brain induced by arterial pulsation and harmonic waves. *Magn Reson Med*. 2013;70:671-683.
10. Tan L, McGarry MDJ, Van Houten EEW, et al. A numerical framework for interstitial fluid pressure imaging in poroelastic MRE. *PLoS One*. 2017;12:e0178521.
11. Biot MA. Theory of propagation of elastic waves in a fluid-saturated porous solid. II. Higher frequency range. *J Acoust Soc Am*. 1956;28:179-191.
12. Aguilera JM, Stanley DW. *Microstructural Principles of Food Processing and Engineering*. Gaithersburg, Maryland: Aspen Publishers, Inc; 1999.
13. Sack I, Schaeffter T. *Quantification of Biophysical Parameters in Medical Imaging*. Cham, Switzerland: Springer; 2018.
14. Nagashima T, Tamaki N, Matsumoto S, Horwitz B, Seguchi Y. Biomechanics of hydrocephalus: A new theoretical model. *Neurosurgery*. 1987;21:898-904.
15. Syková E, Nicholson C. Diffusion in brain extracellular space. *Physiol Rev*. 2008;88:1277-1340.
16. Parker KJ. A microchannel flow model for soft tissue elasticity. *Phys Med Biol*. 2014;59:4443-4457.
17. Parker KJ. Experimental evaluations of the microchannel flow model. *Phys Med Biol*. 2015;60:4227-4242.
18. Streitberger K, Lilaj L, Schrank F, et al. How tissue fluidity influences brain tumor progression. *Proc Natl Acad Sci USA*. 2020;117:128-134.
19. Kawamoto T. Use of a new adhesive film for the preparation of multi-purpose fresh-frozen sections from hard tissues, whole-animals, insects and plants. *Arch Histol Cytol*. 2003;66:123-143.
20. Dittmann F, Tzschätzsch H, Hirsch S, et al. Tomoelastography of the abdomen: Tissue mechanical properties of the liver, spleen, kidney, and pancreas from single MR elastography scans at different hydration states. *Magn Reson Med*. 2017;78:976-983.
21. Ashburner J, Friston KJ. Friston KJ. Unified segmentation. *Neuroimage*. 2005;26:839-851.
22. Debbaut C, Vierendeels J, Casteleyn C, et al. Perfusion characteristics of the human hepatic microcirculation based on three-dimensional reconstructions and computational fluid dynamic analysis. *J Biomech Eng*. 2012;134:011003.
23. Wolff S, Balaban RS. Magnetization transfer contrast (MTC) and tissue water proton relaxation in vivo. *Magn Reson Med*. 1989;10:135-144.
24. Dixon WT, Engels H, Castillo M, Sardashti M. Incidental magnetization transfer contrast in standard multislice imaging. *Magn Reson Imaging*. 1990;8:417-422.

25. Kamali-Zare P, Nicholson C. Brain extracellular space: geometry, matrix and physiological importance. *Basic Clin Neurosci*. 2013;4:282-286.
26. Van Harreveld A, Crowell J, Malhotra SK. A study of extracellular space in central nervous tissue by freeze-substitution. *J Cell Biol*. 1965;25:117-137.
27. Van Harreveld A. The extracellular space in the vertebrate central nervous system. In: Bourne GH, ed. *The Structure and Function of Nervous Tissue 4*. New York: Academic Press, Inc; 1972: 447-511.
28. Ohno N, Terada N, Saitoh S, Ohno S. Extracellular space in mouse cerebellar cortex revealed by in vivo cryotechnique. *Comp Gen Pharmacol*. 2007;505:292-301.
29. Schlageter KE, Molnar P, Lapin GD, Groothuis DR. Microvessel organization and structure in experimental brain tumors: Microvessel populations with distinctive structural and functional properties. *Microvasc Res*. 1999;58:312-328.
30. Streitberger K, Wiener E, Hoffmann J, et al. In vivo viscoelastic properties of the brain in normal pressure hydrocephalus. *NMR Biomed*. 2011;24:385-392.
31. Perriñez PR, Pattison AJ, Kennedy FE, Weaver JB, Paulsen KD. Contrast detection in fluid-saturated media with magnetic resonance poroelastography. *Med Phys*. 2010;37:3518-3526.
32. Pattison AJ, Perrinez PR, Mcgarry M, Weaver JB, Paulsen KD. Feasibility study to measure changes in intracranial pressure using magnetic resonance poroelastography. In Proceedings of the 10th Annual Meeting of ISMRM, Stockholm, Sweden, 2010, p. 3406.
33. Deoni SCL, Rutt BK, Jones DK. Investigating the effect of exchange and multicomponent T1 relaxation on the short repetition time spoiled steady-state signal and the DESPOT1 T1 quantification method. *Magn Reson Med*. 2007;25:570-578.
34. Fehlner A, Hirsch S, Weygandt M, et al. Increasing the spatial resolution and sensitivity of magnetic resonance elastography by correcting for subject motion and susceptibility-induced image distortions. *J Magn Reson Imaging*. 2017;46:134-141.

SUPPORTING INFORMATION

Additional Supporting Information may be found online in the Supporting Information section.

FIGURE S1 Average IR-MRI porosity of 4 samples compared to the corresponding porosity measured by the microscopy
FIGURE S2 Histogram of the distribution of ρ_{12} values in the tofu phantom represented in Figure 8
FIGURE S3 Comparison of porosity in homogenous areas of WM obtained by analyzing standard IR-MRI scans and long idle time IR-MRI scans
FIGURE S4 Comparison between the anatomical scans and ρ_{12} maps shown in Figure 9

How to cite this article: Lilaj L, Fischer T, Guo J, Braun J, Sack I, Hirsch S. Separation of fluid and solid shear wave fields and quantification of coupling density by magnetic resonance poroelastography. *Magn Reson Med*. 2021;85:1655–1668. https://doi.org/10.1002/mrm.28507

My curriculum vitae does not appear in the electronic version of my paper for reasons of data protection.

List of publications:

- **Magnetic Resonance in Medicine (2021)**
  Separation of fluid and solid shear wave fields and quantification of coupling density by magnetic resonance poroelastography
  Lilaj L, Fischer T, Guo J, Braun J, Sack I, Hirsch.
  Editor's pic of March 2021
  Journal impact factor 2019: 3.635

- **Proceedings of the National Academy of Sciences (2021)**
  How tissue fluidity influences brain tumor progression
  Streitberger K J*, Lilaj L*, Schrank F, Braun J, Hoffmann K T, Reiss-Zimmermann M, Käs J A, Sack I.
  *Lilaj and Streitberger equally contributing first authors.
  Journal impact factor 2019: 9.412

- **Magnetic Resonance in Medicine (Accepted)**
  Inversion recovery MR elastography of the human brain for improved stiffness quantification near fluid-solid boundaries
  Lilaj L, Herthum H, Meyer T, Shahryari M, Bertalan G, Caiazzo A, Braun J, Fischer T, Hirsch S, Sack I.
  Journal impact factor 2019: 3.635

- **Magnetic Resonance in Medicine (2021)**
  Reduction of breathing artifacts in multifrequency magnetic resonance elastography of the abdomen
  Shahryari M, Meyer T, Warmuth C, Herthum H, Bertalan G, Tzschätzsch H, Stencel L, Lukas S, Lilaj L, Braun J, Sack I.
  Journal impact factor 2019: 3.635

- **Frontiers in Physiology (2021)**
  Changes in liver mechanical properties and water diffusivity during normal pregnancy are driven by cellular hypertrophy
  Garczyńska K, Tzschätzsch H, Kühl A, Morr A S, Lilaj L, Häckel A, Schellenberger E, Berndt N, Holzhütter H G, Braun J, Sack I, Guo J.
  Journal impact factor 2019: 4.134

Acknowledgments

I'd like to express my deepest thanks to Professor Ingolf Sack for his invaluable suggestions, supervision, patience, and encouragement. Thanks for converting errors into lessons, pressure into productivity, and skills into strengths. It's been a pleasure learning from you.
I am very grateful to Dr. Sebastian Hirsch for his supervision and for kindly sharing his knowledge and time with me.
I'd also like to express my gratitude to Professor Jürgen Braun for his support and trust, even before getting to know me in person.
A special thanks to Dr. Jing Guo for her invaluable help as a colleague and a friend.
I would like to extend my deepest gratitude to my colleagues Angela Ariza de Schellenberger, Anna-Sophie Morr, Baptiste Polchlopek, Bernhard Kreft, Carsten Warmuth, Eric Barnhill, Felix Schrank, Florian Dittmann, Gergely Bertalan, Heiko Tzschätzsch, Helge Herthum, Jakob Jordan, Joachim Snellings, Judith Bergs, Karolina Garczynska, Matthias Anders, Mehrgan Shahryari, Rolf Otto Reiter, Steffen Görner, Tom Meyer, Yang Yang, Stephan Marticorena Garcia, Yasmine Safraou and Yavuz Oguz Uca. The time spent with all of you has been a gift that I will keep in my most precious memories.
I would also like to thank the first cohort of BIOQIC students, especially Azadeh Mohtashamdolatshahi, Matteo Ippoliti, and Andreas Kofler. We made it, guys!
My endless gratitude goes to my friends, especially Valentino Lepro and Nino Chirico, who motivated me to move to Berlin for my Ph.D. project and were at my side at every step of it, as always.
Last but certainly not least, I have no words to express how grateful I am for parents Kastriot Lilaj and Tefta Hysa and my brother Paolo. Without your support and love, none of this would have been possible.

Thank you.